Luminescent Metal Hydrides Containing Europium(II)
and
Hydrogenation Studies of Ytterbium and $Li_xSr_{1-x}AlSi$

DISSERTATION

zur Erlangung des Grades
des Doktors der Naturwissenschaften
der Naturwissenschaftlich-Technischen Fakultät III
Chemie, Pharmazie, Bio- und Werkstoffwissenschaften
der Universität des Saarlandes

von
Dipl. Chem. Nathalie Kunkel

Saarbrücken
Februar 2014

Tag des Kolloquiums: 26. Mai 2014

Dekan: Prof. Dr. Volkhard Helms

Berichterstatter: Prof. Dr. Holger Kohlmann

Prof. Dr. Michael Springborg

Prof. Dr. Thomas Schleid

Vorsitz: Prof. Dr. Gregor Jung

Akademischer Mitarbeiter: Dr. Bernd Morgenstern

The scientist is motivated primarily by curiosity and a desire for truth.

Irving Langmuir, Nobel Prize in Chemistry 1932

Meinem Vater Helmut

Abstract

The first systematic study of Eu(II)-luminescence in hydride and hydride-fluoride host lattices is described within the present work. Due to its high emission intensities and the dependence of its emission wavelength on its coordination sphere, Eu(II) is of major importance for the design of luminescent materials.

Eu(II) luminescence was studied in hydrides of the alkaline earth metals MH_2 (M = Ca, Sr, Ba), the perovskites $LiMH_3$ (M = Sr, Ba), $AMgH_3$ (A = Na, K), ternary magnesium hydrides and the hydride-fluorides EuH_xF_{2-x}, $LiMH_xF_{3-x}$ (M = Sr, Ba) and $KMgH_xF_{3-x}$. Samples showed broad band emission as it is typical for the electric dipole transition $4f^7$ - $4f^65d$. The widest redshift ever observed in the emission of Eu(II) was found for the alkaline earth metal hydrides MH_2 (M = Ca, Sr, Ba) and $NaMgH_3$.

Extremely well-resolved spectra of Eu(II) in $LiSrD_3$ and $LiSrH_3$ allowed the assignment of different vibrational modes and thus the clarification that the bonding in the $4f^{n-1}5d(e_g)$ excited state is weaker than in the ground state and also the first quantitative estimation of the crystal field strength of hydride and deuteride ever.

It was also shown that the variation of the hydride and fluoride content in mixed compounds allows the targeted design of phosphors with varying emission colors.

Additionally, *in-situ* deuteration studies of Yb and theoretical studies of the hydrogenation of $Li_xSr_{1-x}AlSi$ were carried through.

Kurzzusammenfassung

In der vorliegenden Arbeit wurde die erste systematische Untersuchung von Eu(II)-Lumineszenz in Hydrid- und Hydridfluoridwirtsgittern durchgeführt. Aufgrund seiner hohen Emissionsintensitäten und der Abhängigkeit der Emissionsenergie von der Koordinationssphäre ist Eu(II) von großer Bedeutung bei der Herstellung von Leuchtstoffen.

Eu(II)-Lumineszenz wurde in den Hydriden der Erdalkalimetalle MH_2 (M = Ca, Sr, Ba), den Perowskiten $LiMH_3$ (M = Sr, Ba), $AMgH_3$ (A = Na, K) und ternären Magnesiumhydriden sowie den Hydridfluoriden EuH_xF_{2-x}, $LiMH_xF_{3-x}$ (M = Sr, Ba) und $KMgH_xF_{3-x}$ untersucht. Die Verbindungen wiesen die für den elektrischen Dipolübergang $4f^7$ - $4f^65d$ typischen breiten Emissionsbanden auf. Die weiteste bekannte Rotverschiebung der Emission von Eu(II) wurde für die Erdalkalimetallhydride MH_2 (M = Ca, Sr, Ba) sowie $NaMgH_3$ beobachtet.

Hochaufgelöste Eu(II)-Spektren in $LiSrD_3$ and $LiSrH_3$ erlaubten die Zuordnung verschiedener Schwingungsmoden und somit die Klarstellung, dass die Bindungsstärke im angeregten $4f^{n-1}5d(e_g)$ schwächer als im Grundzustand ist und weiterhin die erste quantitative Abschätzung der Kristallfeldstärke von Hydrid und Deuterid. Zusätzlich konnte gezeigt werden, dass die Variation von Hydrid- und Fluoridgehalt in gemischten Verbindungen die gezielte Synthese von Leuchtstoffen mit gewünschten Emissionsfarben ermöglicht.

Zusätzlich wurden *in-situ* Deuterierungsuntersuchungen an Yb und theoretische Studien der Hydrierungen von $Li_xSr_{1-x}AlSi$ durchgeführt.

Acknowledgements

The present study was carried out within the groups of Prof. Dr. Holger Kohlmann and Prof. Dr. Michael Springborg from October 2010 to February 2014.

In the first place I would like to thank my supervisor Prof. Dr. Holger Kohlmann for his unlimited support and patience, his advice, all the long discussions and, most of all, for giving me the freedom to choose topics and directions of my research and always supporting me in pursuing my own ideas and the spectroscopical studies. I am greatly indebted to Prof. Dr. Andries Meijerink for his enormous support in spectroscopic questions, sharing his huge experience with me and allowing me to use his equipment. Without his help, the investigating spectroscopic properties would definitely not have been possible to such a large extent.

Furthermore, I thank Prof. Dr. Michael Springborg for his support, his help with quantum-mechanical questions, introducing me into the theoretical chemistry community and for adopting me in his group.

I thank Dr. Robert Haberkorn for helping me with any questions concerning X-ray and neutron diffraction as well as crystallography, many weekends refining and taking many of the luminescence pictures. And also Prof. Dr. H. P. Beck for scientific discussions.

I would like to thank my two groups in Saarbrücken, especially Stephan Kohaut for his enormous help in computational questions and Dr. Oliver Clemens, Jonas Sander, Patrick Wenderoth, Christian Reichert, Jessica Bauer and Nicolas Louis, as well as the group in Leipzig. I'd also like to thank the group in Utrecht for their warm welcome and support. I'm furthermore indebted to my students, especially Ramona Hahn, who was a huge support in analytics. I'm also thankful to PD Dr. Ralf Kautenburger and Dr. Christina Hein for help with the ICP-MS analyses.

I also thank PD Dr. Richard Weihrich and Wenjie Yan for temperature-dependent XRD measurements and Thomas Hansen for support at the D20/ILL.

I am thankful to my high school teacher Oliver Busch, who had already believed in me and supported my will to become a scientist in the early days.

I'm also indebted to Prof. Dr. Katharina Kohse-Höinghaus for tutoring me and Prof. Dr. Guido Kickelbick for giving me a place in his lab.

I am thankful to Prof. Dr. Claudia Wickleder and Dr. Matthias Adlung for allowing me the use of their spectrometer and Prof. Dr. Henning Höppe for discussion.
Furthermore I would like to thank the Landesgraduiertenförderung for financial support and especially Dr. Theo Jäger and Prof. Dr. Manfred Schmitt for support and advice.
I'm also extremely indebted to Sylvia Beetz and Hermann Recktenwald for technical support and making my work with high hydrogen pressures possible and to Günter Berlin for all the ampoules.
Last, but not least, I thank my family for their love and support.

Contents

1 Introduction and aims

So-called phosphors or luminescent materials find application in a vast number of devices of importance, such as fluorescent tubes, LEDs, lasers, fiber amplifiers, plasma displays, solar cells, scintillator crystals and afterglow materials[1–3].

Following an excitation -usually via UV emission of a gas discharge, X-rays, cathode rays, UV LEDs or blue-emitting LED chips- the phosphor emits light in the visible color range. Depending on the decay times, the emission is classified as fluorescence ($\tau < 10$ ms) or phosphorescence ($\tau > 0.1$ s) and the phosphor is therefore either suited for applications requiring short lifetimes or a long afterglow[4]. In order to achieve high emission intensities, high transition probabilities are needed.

Luminescence of inorganic solids may be classified into luminescence of activator ions and semiconductors; the following work focuses on luminescent materials whose emission is based on the former mechanism. *Classical* inorganic phosphors are luminescent materials consisting of a host lattice and an activator ion such as, for instance, a rare earth ion[2]. In order to avoid concentration quenching a rather small doping rate is usually chosen. Such activator ions can be classified into two different categories: activator ions that interact weakly with the host lattice and such that interact strongly. Weakly interacting activator ions are lanthanide ions Ln^{3+} showing intraconfigurational transitions within the 4f shell which lead to typical line emissions. In contrast, for activator ions such as Eu^{2+} and Ce^{3+} whose emission originates from d-f transitions, as well as activator ions with s^2 configurations such as Pb^{2+} and Bi^{3+}, a strong interaction with the lattice is observed.

Even though a large number of luminescent materials is known, there is still a need for improvement and development of new materials with better properties. Improved materials should, for instance, possess better energy efficiency or different color coordinates and temperatures[3]. Especially the former becomes more and more important, because the global stock of fossil fuels is running low and alternative energies, as well as energy efficiency, rapidly gain in importance. Since the widely-used blue-emitting BAM ($BaMgAl_{10}O_{17}:Eu^{2+}$) lacks a sufficient radiation and temperature stability, there is still need for a better blue-emitting material. The alternative material $LaPO_4:Tm^{3+}$ exhibits a better temperature stability, but also unwanted emissions in the UV reducing the brilliance of the phosphor. The commonly-used red-emitting phosphors

(Y, Gd)BO_3:Eu^{3+} or Y_2O_3:Eu^{2+} show satisfying quantum efficiencies as well as temperature and radiation stability, however, also an unwanted additional orange emission. Green-emitting phosphors either exhibit unwanted blue emission (as e.g. materials based on Tb^{3+}) or a lack of stability and an afterglow (Zn_2SiO_4:Mn^{2+}). Due to a need for improved sensitivity of scintillation materials as well as improved reactions times in new medical applications, the development of new X-ray detection materials is of great interest[3]. The host lattice of such materials, e.g. $BaFBr_{1-x}I_x$:Eu^{2+}, forms electron-hole pairs upon ionization caused by ionizing radiation and, following an energy transfer, activator ions emit light. Conventional materials show rather long reaction times thus limiting the time resolution of the detector.

1.1 Divalent europium as a phosphor

Due to its exceptional luminescence properties, divalent europium doped into inorganic compounds is of great interest for applications as a phosphor. $4f^65d^1 \rightarrow 4f^7$ transitions are parity-allowed, resulting in much shorter emission lifetimes as well as in oscillator strengths by 3-4 orders higher than for the forbidden f-f transitions of trivalent rare earth ions and therefore high emission intensities. Furthermore, the d-electrons are relatively unshielded against interactions with the lattice and the emission energies of these transitions show a strong dependence on the coordination sphere[5]. Consequently, divalent europium as a dopant in different host lattices is used in the production of LEDs of variable colors for screen or laser applications. Yet, mainly oxides and fluorides, which usually exhibit emission energies in the blue or green color region, have been used as host lattices. Studies of other host lattices, such as nitrides or sulfides, are rather rare. Until recently, hydrides have been completely unknown as a host lattice for divalent rare earth ions. However, a hydridic matrix could serve as an extremely interesting system for the study of luminescence properties of divalent lanthanides, since the hydride ligand should posses a strong influence on the energetic position of the d-levels due to its softness and polarizability. Thus a redshift in the emission energies compared to known emission energies of divalent europium doped in compounds, such as oxides, can be expected. Furthermore, as the ionic radii of hydride and fluoride are very similar and many metal hydrides exhibit isotypic fluorides, a partial substitution of hydride by fluoride and vice versa[6] in order to obtain a different ligand field strength should be possible, consequently allowing the design of phosphors of any desired color.

1.2 Aims

This work intends to help understanding the dependence of the luminescence properties of an activator ion, in particular Eu(II), on the host lattice. A profound knowledge of the influence of a host lattice allows the design of luminescent materials with desired properties. As model systems, metal hydride host lattices providing the most simple anions possible, H^-, are chosen and effects of its covalence and polarizability on the emission energies, or more precisely, on the crystal field splitting and the location of the center of gravity of the 5d levels of Eu(II) are investigated. Furthermore, the influence of partial substitution of the rather soft hydride ligand with the rather hard fluoride ligand is studied. Mixed hydride fluorides might also exhibit a much better stability towards air and humidity than pure hydrides.

In order to study Eu(II) in a hydridic matrix, suited systems need to be selected. An important issue for the selection of a system is the size of the band gap, because compounds exhibiting narrow band gaps are likely to show luminescence quenching. For instance, alkaline-earth metal compounds with a sufficiently large band gap could serve as a host lattice. As many of them exhibit an isotypic europium compound, the existence of solid solution series seems likely, a fact that might facilitate doping with Eu(II).

2 Theoretical background

2.1 Metal hydrides

Due to its size and electron configuration $1s^1$, hydrogen holds an exceptional position in the periodic table[7]. Containing only one electron and one proton, it is the lightest of all elements. Since oxidation leads to a proton, whereas the inert-gas electron configuration is reached through the acceptance of an electron, hydrogen may show a chemical behavior similar to alkaline earth metals as well as halogens[8]. However, compared to the halogens, it possesses a lower electron affinity and electron negativity resulting in a less pronounced nonmetal character. Together with most of the other elements -apart from the noble gases and a few others- it forms at least one hydrogen compound[7,9] and, depending on the electronegativity of the binding partner, it carries a positive or negative partial charge.

Metal hydrides show a large number of compounds with varying stoichiometry as well as different structural and electronic properties and may be classified into covalent, ionic and metallic hydrides. Tetrahedral SnH_4 molecules are, for instance, covalent hydrides just as the hydrides of the non- and semimetals. Depending on the electronegativity of the binding partner the bond in a covalent hydride may be of almost nonpolar character or strongly polar.

Ionic hydrides crystallize in ionic lattices formed by metal cations and hydride anions. The hydrides of the alkaline and alkaline earth metals apart from beryllium, as well as hydrides formed by divalent europium and ytterbium, can be described as typical ionic compounds. The alkaline metal hydrides, for instance, crystallize in the sodium chloride structure; at standard conditions strontium and divalent europium hydride crystallize in the lead dichloride structure[10,11]. However, the bonds of these ionic compounds exhibit covalent parts, which increase, for instance, from barium hydride towards magnesium hydride or from the alkaline metal hydrides towards the alkaline earth metal hydrides. Furthermore, not only binary hydrides, but also some ternary hydrides, such as $SrMgH_4$, $LiSrH_3$ or $Ca_4Mg_3H_{14}$, are counted among the class of saline metal hydrides[12].

Metallic hydrides are almost exclusively transition metal hydrides with atomic hydrogen embedded in interstitials in the metal lattice and are therefore also called interstitial hydrides[13]. They usually show a metal-like appearance, a disordered distribution of hydrogen atoms, a high hydrogen mobility[14] and often exhibit interesting electronic features. For instance, palladium becomes superconducting through hydrogen uptake, showing a strong dependence of the critical temperature on the ratio of hydrogen and palladium from a ratio of 0.77 onwards[15]. Due to their reversible hydrogen release at high temperatures metallic hydrides are of interest for technical application. $LaNi_5H_{6-x}$[16], for instance, is used as a battery material in nickel metal hydride storage batteries.

Except those three categories of binary hydrides discussed above, furthermore there are complex ternary hydrides $A_xM_yH_z$ with an electropositive metal A and a transition metal M[7], such as K_2ReH_9[17,18]. Complex hydrides are stoichiometric and usually non-metallic compounds with discrete metal-hydrogen bonds[14].

2.2 Binary hydrides of europium and ytterbium

Unlike the other rare earth metals exhibiting a more stable trivalent character and therefore forming trihydrides already at atmospheric pressure and moderate temperatures, hydrogenation of europium and ytterbium at these conditions yields only dihydrides[19]. The formation of dihydrides could easily be explained by the electronic configuration favoring a divalent valence state in many compounds[20].

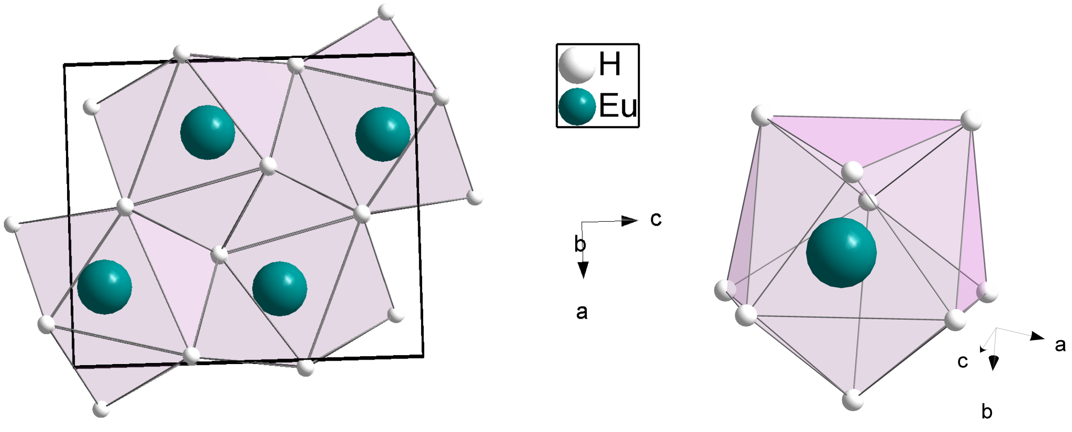

(a) View along the *b*-axis.

(b) Coordination polyhedron.

Figure 1: Structure of EuH_2 in view along the *b*-axis (a) and the coordination polyhedron of europium (b).

These dihydrides crystallize in the orthorhombic $PbCl_2$ structure type, which can also be found in the hydrides of alkaline earth metals[21]. Trigonal MH_6-prisms sharing common triangular faces along the crystallographic axes *b* form columns and are further linked by common edges. The interconnected prisms form zigzag chains along *a*. Europium or ytterbium is situated in the center of a tricapped trigonal prism of hydrogen atoms. Both metal deuterides have been examined using neutron diffraction[11,22,23].

The ytterbium dihydride can be synthesized by hydrogenating ytterbium metal at about 550 K and atmospheric pressure. However, already in 1966, the synthesis of an ytterbium hydride with an atomic ratio H:Yb greater than 2 was reported[24]. Hydrogenation was carried out at several atmospheres pressure. The hydride was of black color and fairly stable in air, its hydrogen content was believed to be 2.55. Structure determination from X-ray powder diffraction suggested the existence of a face-centered cubic structure with a lattice constant of about 519 pm. Decomposing $YbH_{2.55}$ led to the formation of hydrides with a hydrogen content of 2.42 and 2.04, respectively, which were believed to crystallize with fcc symmetry. Additionally, a metastable fcc YbH_2 was reported which converts to the orthorhombic form on annealing. Furthermore, the synthesis of ytterbium hydrides with a hydrogen content of 2.59 and 2.74 at 350°C and atmospheric pressure was reported[25]. Their structures were also assumed to be face-centered cubic.

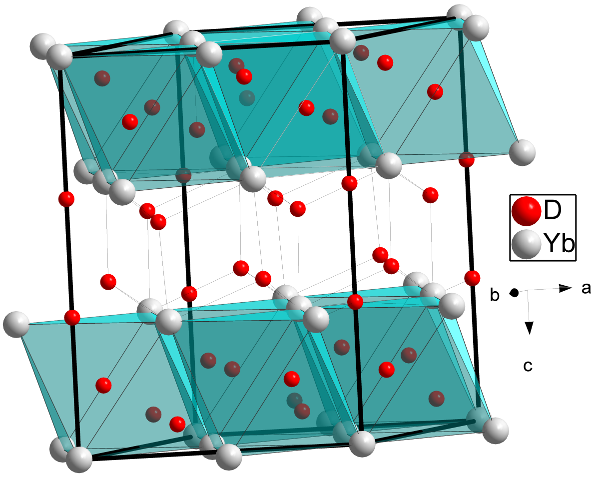

Figure 2: Structure of $YbD_{2.67}$ as described by Auffermann[26].

Anyhow, reinvestigation of the assumed cubic structure and synthesis of $YbD_{2.67}$ at high pressure led to the conclusion that these hydrides do not crystallize in the cubic structure type, but rather with trigonal symmetry[26]. The structure was described as close-packing of ytterbium with an ordered occupation of the tetrahedral holes and 2/3 of the octahedral holes by hydrogen. Within the work mentioned above, samples were synthesized under high pressures up to 3200 bar, however, X-ray and neutron diffraction measurements only took place at standard pressure and *in-situ* measurements were not carried out. Therefore nothing is known about the existence of phases stable only at high hydrogen pressures.

2.3 Metal hydrides used as host lattices for Eu(II)

In the following, structures and properties of the metal hydrides used as host lattices for Eu(II) will be shortly depicted. Due to the similar ionic radii of Sr^{2+} and Eu^{2+}[27], many europium compounds have isotypic strontium compounds and europium is likely to occupy strontium sites, making a europium doping of strontium host lattices facile. As deuterides are often preferred for structural refinement due to the larger neutron bound coherent scattering cross section of deuterium compared to hydrogen[28,29], the terms hydride and deuteride will be used simultaneously unless not indicated otherwise.

2.3.1 MH_2; M = Ca, Sr, Ba

The alkaline earth metal hydrides can be prepared by exposing the metals to a hydrogen atmosphere at elevated temperatures[21]. Hydrogen or deuterium positions in CaH_2[30] and CaD_2[31,32], SrH_2[10] and SrD_2[10], BaH_2[10] and BaD_2[10,33] were determined using neutron diffraction. Similar to EuH_2, they crystallize in the orthorhombic $PbCl_2$ structure type. Therefore it seems likely that doping with europium or even the preparation of mixed crystals is possible and the alkaline earth metal hydrides are suitable host materials for Eu(II) luminescence. Such mixed crystals have already been synthesized for the system $Eu_xSr_{1-x}H_2$[34,35]. Assuming that europium occupies the site of the alkaline earth metal atom, its coordination polyhedron consists of a tricapped trigonal prism of hydrogen atoms.

2.3.2 ABH_3; A = Li, K, Na, B = Sr, Ba, Mg

$LiSrH_3$ and $LiBaH_3$ are colorless solids crystallizing in the cubic inverse perovskite structure type and were prepared by reaction of the binary hydrides[36–38] or, in case of $LiBaH_3$, also from LiH, Li_3N and Ba[39]. Lithium is surrounded by six hydrogen ligands in an octahedral arrangement, whereas the alkaline earth metal is coordinated cuboctahedrally. The structure type has been unambiguously confirmed by neutron diffraction studies on $LiBaH_3$ and $LiBaD_3$[37] and for the similar europium compound $EuLiD_3$[11]; $LiSrH_3$ was presumed to be isostructural.

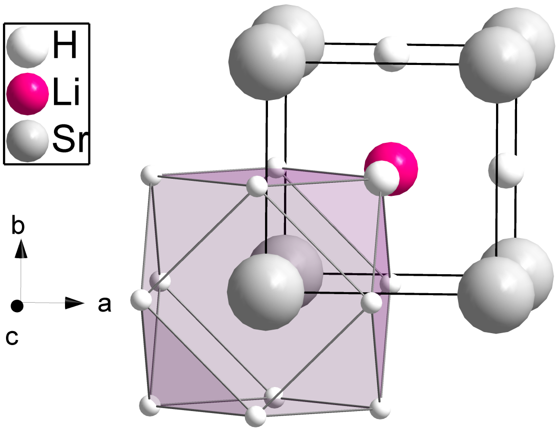

Figure 3: Structure of $LiSrH_3$.

$KMgH_3$ was first prepared by the hydrogenolysis of KMg(*sec*-C_4H_9)$_2$ in benzene solution or by a pyrolytic olefin elimination reaction in vacuum[40]. Alternative syntheses are the reaction of the binary hydrides under hydrogen pressure[41] or the hydrogenation of a mixture of the metals[42]. Comparing the diffraction data of $KMgH_3$ and $KMgF_3$[43] and analyzing single crystal X-ray data[42], the normal cubic perovskite structure with magnesium in the octahedral environment was assumed.

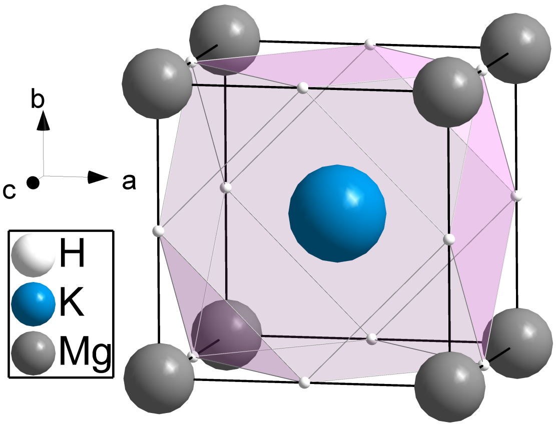

Figure 4: Structure of $KMgH_3$.

The ternary hydride $NaMgH_3$ crystallizes in the orthorhombically distorted perovskite structure of $GdFeO_2$ (*Pnma*) and is isotypic with the fluoride $NaMgF_3$[44]. It can be prepared via the reactions of the binary hydrides at 380°C and 70 bar H_2 pressure.

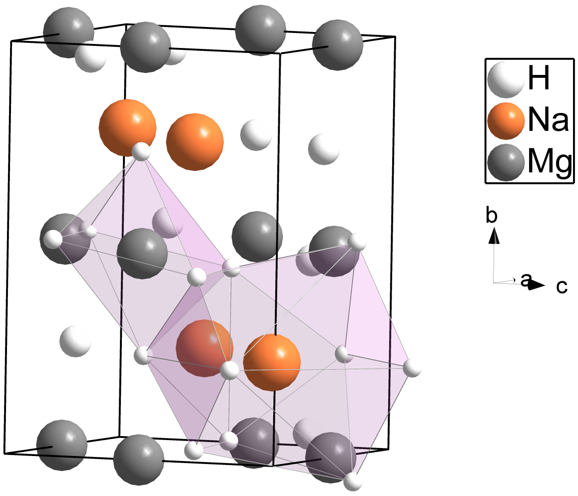

Figure 5: Structure of $NaMgH_3$ according to[44].

The isotypic fluorides doped with divalent europium $LiBaF_3:Eu^{2+}$[45] and $KMgF_3:Eu^{2+}$[46] have been studied before. $KMgF_3$ is the first known host lattice allowing the observation of ^6I emission of Eu(II). Due to the small crystal field splitting and the energetically high position of the barycenter of the $4f^65d$ states in $KMgF_3$, the lowest $4f^65d$ level is situated above the $^6I_{7/2}$ level and the ^6I emission is visible below 25 K (approx. 360 nm). The emission from the $^6I_{7/2}$ level is quenched via the lowest $4f^65d$ level above 25 K. For $LiBaF_3$ the lowest excited states within the $4f^7$ configuration ($6P_J$) are lower in energy than the lowest $4f^65d$ state, thus allowing the observation of magnetic dipole transitions and vibrationally induced electric dipole transitions within the $4f^7$ states. The position of the zero-phonon lines is given as 359.1 nm. However, no evidence for the existence of $LiSrF_3$ has been found so far[38].

2.3.3 $SrMgH_4$

$SrMgH_4$ and $SrMgD_4$ can be prepared from the Sr-Mg alloy under hydrogen (deuterium) pressure and crystallize in the $BaZnF_4$ structure (space group $Cmc2_1$)[47]. The isotypic europium compound also exists[48]. The noncentrometrical structure can be seen as a distorted variant of the centrosymmetrical homologue $BaMgH_4$. Strontium is coordinated by nine close hydrogen (deuterium) atoms in a distorted trigonal prism connecting via triangular faces parallel to the (100) plane. Magnesium is coordinated by six close hydrogen (deuterium) neighbors that form a distorted octahedron and are connected with three SrH_9 units via common edges or faces. The MgH_6 units form columns perpendicular to [100] and [001]. Thus two different sites of the host lattice might be occupied by europium. However, due to the similar radii, europium is more likely to occupy the strontium position.

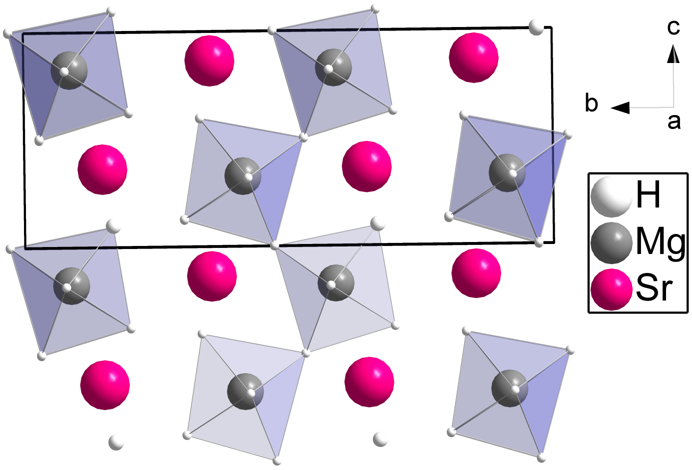

Figure 6: Structure of $SrMgD_4$.

2.3.4 $BaMgH_4$

$BaMgH_4$ is the centroysymmetrical variant (*Cmcm*) of $SrMgH_4$ and can be prepared by heating BaH_2 and Mg powder under high hydrogen pressure[49].

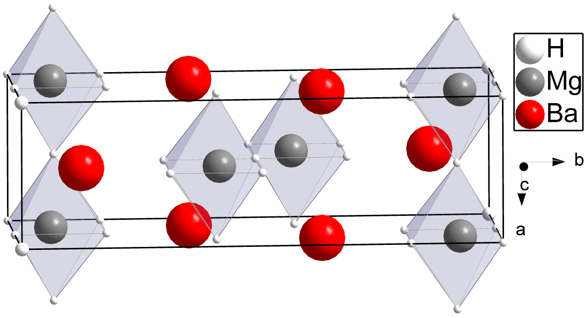

Figure 7: Structure of $BaMgH_4$.

Its structure is built up by MgH_6 octahedra forming zigzag chains parallel to the c-axis that are linked via vertices. Linking of the chains leads to the formation of slabs running parallel to the *ac* plane. The almost cuboctahedral coordination sphere of barium, which is situated in between the slabs, is formed by 13 hydrogen atoms. One of the prism faces of the cuboctahedron is capped by two hydrogen ligands.

2.3.5 $Ba_6Mg_7H_{26}$

$Ba_6Mg_7H_{26}$ can be prepared by sintering a 6:7 mixture of BaH_2 and magnesium powder at 730 K and 100 bar hydrogen pressure[50] and crystallizes in the space group *Immm*.

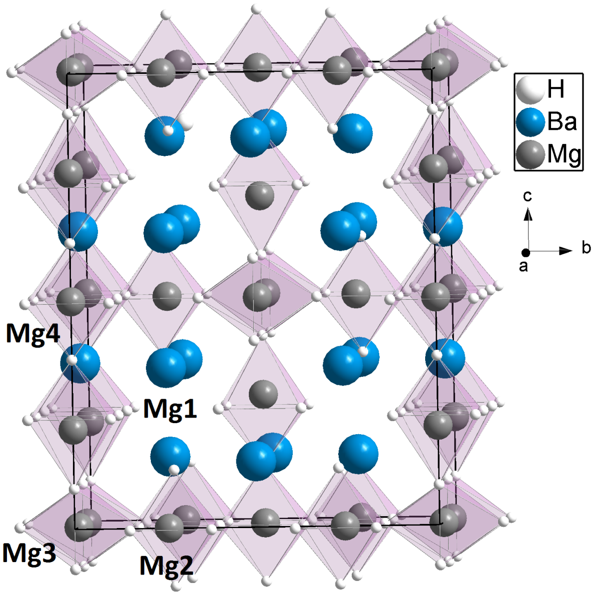

Figure 8: Structure of $Ba_6Mg_7H_{26}$, *Immm*, according to[50].

However, characterization was carried out on a multiphase sample containing considerable amounts of Ba_2MgH_6, $BaMgH_4$ and MgO. Magnesium is coordinated more-or-less octahedrally by six hydrogen atoms with one octahedron being strongly elongated. There are four magnesium sites which are indicated by Mg1-Mg4. The Mg3-octahedra form rutile-like chains running along *a* connected by Mg2- and Mg4-octahedra and build up slabs that run parallel to the *ab* plane. Those slabs are connected with the Mg1-octahedra. Barium is coordinated cuboctahedrally.

2.3.6 Ba_2MgH_6

Sintering the binary hydrides BaH_2 and MgH_2 at high hydrogen pressure leads to the formation of Ba_2MgH_6[51].

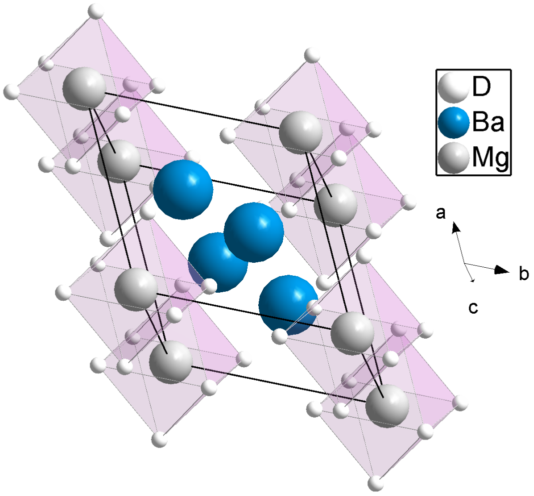

Figure 9: Structure of Ba_2MgD_6, $P\bar{3}m1$, according to[51].

The ternary hydride crystallizes in the trigonal K_2GeF_6 structure type (space group $P\bar{3}m1$). Magnesium is in the center of a nearly regular octahedron of hydrogen atoms.

2.3.7 $Ca_4Mg_3H_{14}$

$Ca_4Mg_3H_{14}$ was prepared via hydrogenation of the CaMg alloy at elevated temperatures and hydrogen pressures[52].

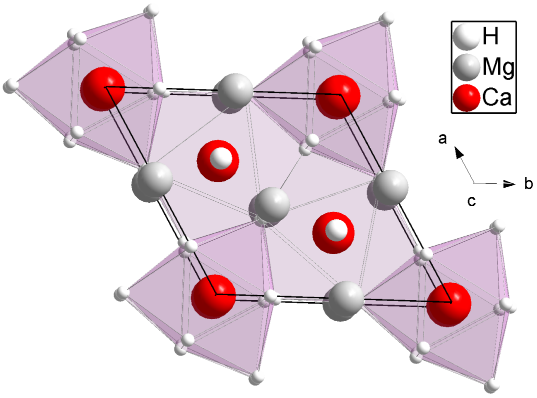

Figure 10: Structure of $Ca_4Mg_3H_{14}$, $P\bar{6}2m$, according to[51].

Calcium forms the center of a tricapped trigonal prism of hydrogen ligands with one trigonal prism sharing edges along the prism axis and forming nets running parallel to the hexagonal base and the other sharing triangular faces and forming columns along [001]. Magnesium is in the center of pentagonal bipyramids sharing four base edges with each other and one with a calcium-centered tricapped trigonal prism.

2.4 Hydride-fluoride analogy and hydride-fluorides

Due to their very similar ionic radii, ionic compounds of hydride and fluoride, such as for instance the alkaline earth compounds, show structural analogies[6]. Shannon reports the effective ionic radius of fluoride for the coordination number 6 as 133 pm (crystal radius 119 pm)[27], whereas the effective radius of hydride varies from 127 to 153 pm[27,53], showing a high polarizability and therefore being highly sensitive to the particular cation. In ionic crystals with minimal polarization, a crystal radius of 153 pm can be assumed[54]. For instance, the alkaline earth metal hydrides crystallize in the $PbCl_2$ structure type in the space group *Pnma* at room temperature, but transform into the more symmetrical cubic structure at higher temperatures. The fluorides, however, crystallize in the cubic structure type at ordinary pressures, but, due to the reduced interatomic distances, transform into the $PbCl_2$ structure at higher pressures[6]. Partial solid solution series of calcium, strontium and barium hydride-fluorides were already synthesized via solid state reactions of the corresponding hydrides and fluorides at elevated temperatures[55,56]. Furthermore, solid solution series of ternary hydride-fluorides, such as $LiSrH_xF_{3-x}$ ($x > 1.0$), $LiBaH_xF_{3-x}$, $KMgH_xF_{3-x}$[38] and $KCaH_{3-x}F_x$[57] were reported. For instance, the solid solution series $KCaH_{3-x}F_x$ were prepared via a solid state reaction of KF, CaF_2 and CaH_2 under high hydrogen pressure and at elevated temperatures in a stainless steel autoclave.

2.4.1 EuF_2 and EuH_xF_{2-x}

In the system EuF_2 and EuH_xF_{2-x} with $x \leq 0.8$ a solid solution series with the fluoride structure type exists[58]. Europium forms a fcc lattice where all tetrahedral voids are occupied by fluoride or hydride anions and europium is coordinated by a cube of anions. For $x > 0.8$ a two phase region containing EuH_2 and $EuF_{1.2}H_{0.8}$ was observed. Within the solid solution series the lattice parameter a remains almost constant. The authors studied the magnetic susceptibilities as well as Mössbauer spectra. Replacing fluorine by hydrogen led to an increase of the covalent character manifesting itself in the increase of electron density in the 6s orbital of europium due to charge transfer from the hydride. EuF_2 shows an absorption at approx. 400 nm, but no luminescence emission[5,59].

2.5 Hydride-chlorides

2.5.1 EuHCl

EuHCl is obtained via the reaction of $EuCl_2$ and EuH_2 at 1000 K and about 3 bar hydrogen pressure[60]. Similar to the strontium compound, the europium compound crystallizes in the tetragonal PbFCl structure type. The layers vertical to the c-axes are built up by the invidual elements. Europium is coordinated by a capped quadratic antiprism (see Fig.11) formed by chloride and hydride ligands. In contrast to EuH_2, EuHCl does not exhibit ferromagnetic but weak antiferromagnetic interactions which might be due to the larger interatomic europium-europium distances.

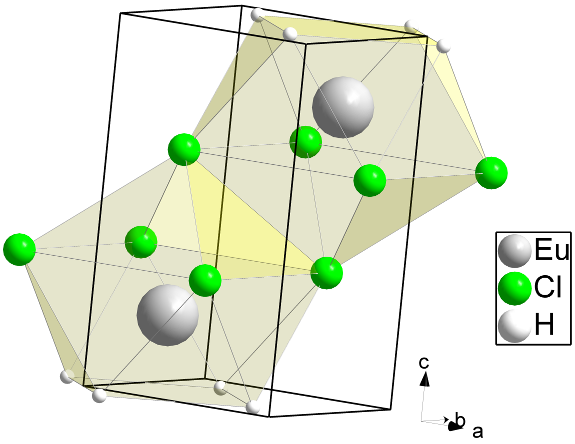

Figure 11: Structure of EuHCl according to[60].

2.6 Half-Heusler phases

Half-Heusler phases are ternary materials XYZ with 1:1:1 stoichiometry forming a tetrahedral zinc blende sub lattice with occupied octahedral positions[61]. They crystallize in the noncentrometrical cubic structure, space group $F\bar{4}3m$. X stands for the most electropositive element (a main group element, transition metal or rare earth element, e.g. Li), Y is a maingroup element and Z the most electronegative element (main group element from the second half of the periodic table, for instance Si). X occupies the octahedral sites, whereas Y and Z form the zinc blende lattice. The bonding within the zinc blende sub lattice has a covalent character and can be described by a molecular orbital approach. X and Y, however, build a NaCl-type sub lattice with interactions of ionic character. An example for a Half-Heusler phase is LiAlSi, which can be synthesized by a melting reaction of the elements[62], crystallizes in the MgMgAs structure type, space group $F\bar{4}3m$ and can be described as $Li^+[AlSi]^-$.

According to[63], LiAlSi can be hydrogenated at 535°C under 80 bar hydrogen pressure to form a phase $LiAlSiH_{0.9}$ with hydrogen occupying half of the tetrahedral voids. However, the hydrogen content was determined only by calculating the pressure difference in the autoclave. The cell parameters did not show a significant change (LiAlSi 593.1(2) pm, $LiAlSiH_{0.9}$ 592.7 pm). During an *in-situ* neutron powder diffraction experiment of our group at the D20/ILL, the proposed $LiAlSiH_{0.9}$ was not found. However, a yet unknown, possibly trigonal, phase was formed[64].

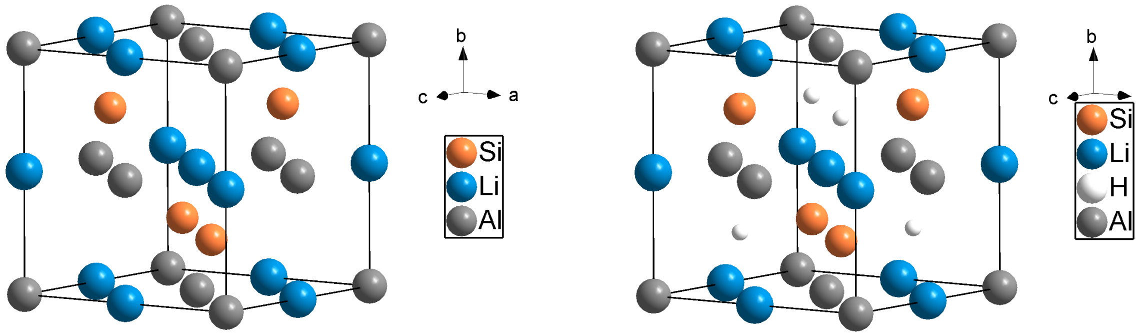

(a) LiAlSi. (b) $LiAlSiH_{0.9}$.

Figure 12: From left to right: LiAlSi according to[62] (a) and $LiAlSiH_{0.9}$ according to[63] (b).

2.7 Zintl phases and hydrides of Zintl phase

Intermetallic compounds with a strong heteropolar binding character are called Zintl-phases. The type of their chemical bonding can be described as a bridge between metals and ionic salts. A commonly accepted prerequisite for a compound being considered as Zintl phase is that it consists of an alkali or alkaline earth metal and a member of the groups 13-17[65]. The electronegative component may reach an electronic octet via an electron transfer from the electropositive component and bonding to each other. The structure of the anionic sub lattice often resembles that of the corresponding p-block element. For low differences in electronegativity between the electropositive and electronegative component, deviations from the Zintl-Klemm concept occur[66].

Hydrogenation of Zintl phases may either lead to the formation of so-called Zintl phase hydrides or polyanionic hydrides. In Zintl phase hydrides hydrogen is hydridic and only coordinated by s-block metal ions. It therefore reduces the number of electrons that can be assigned to the electronegative component and ultimately leads to changes in the polyanionic substructures. In polyanionic hydrides hydride bonds covalently to a p-block metal atom and those hydrides can be described as intermediates between Zintl phases and ionic metal hydrides. An example for such a polyanionic hydride is SrAlSiH[67], which can be obtained by hydrogenation of SrAlSi. SrAlSiH, as well as other monohydrides MTtTrH (M = Ca, Sr, Ba; Tr = Al, Ga, In; Tt = Si, Ge, Sn)[66], contain layered polyanions such as, for instance, $[AlSiH]^{2-}$.

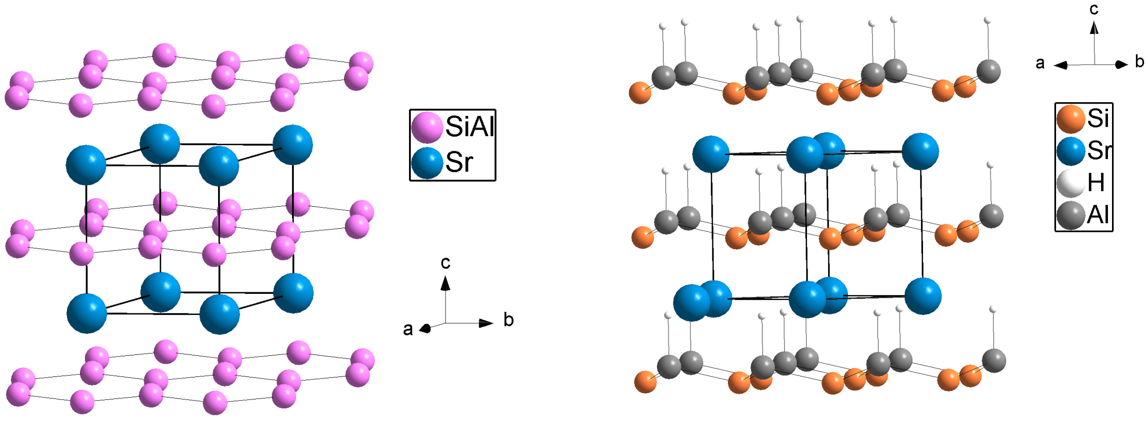

(a) SrAlSi.

(b) SrAlSiH.

Figure 13: From left to right: SrAlSi according to[68] (a) and $SrAlSiH_{0.9}$ according to[66] (b).

2.8 Structural classifications and the radius of hydride

2.8.1 Grouping of $PbCl_2$ type compounds

Compounds crystallizing in the $PbCl_2$ structure type can be classified according to their $\frac{a+c}{b}$ and $\frac{a}{c}$ ratios[69,70]. Salt-like compounds, such as $PbCl_2$[71] and the dihydrides of Ca, Sr, Ba and Eu[19,21] belong to a group with $\frac{a}{c}$ between 0.8 and 0.9 and $\frac{a+c}{b}$ from 3.3 to 4.0. Within the group, differences in the coordination polyhedra are only small, whereas they differ strongly from other compounds of groups with other values for the ratios mentioned above.

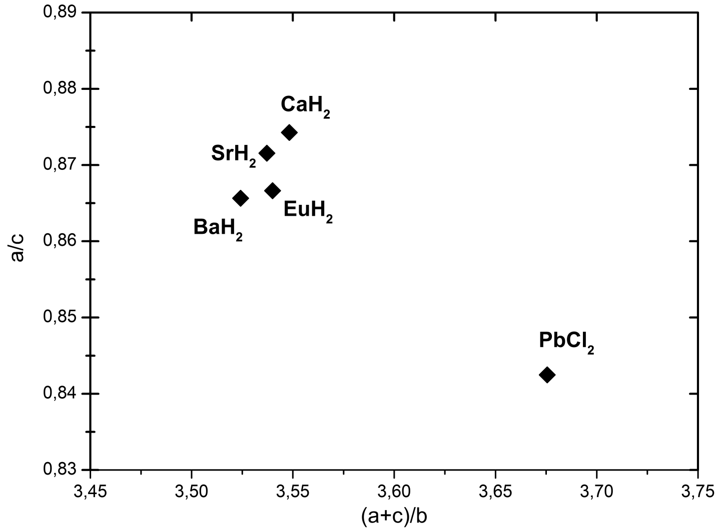

Figure 14: Grouping of EuH_2 and the alkaline earth metal hydrides of Ca, Sr, Ba crystallizing in the $PbCl_2$ structure type according to their axial ratios.

2.8.2 Covalence and the radius of hydride

Due to its covalence and polarizability, the radius of hydride depends on the cation and the structure type. Pauling proposed a rather large radius of 208 pm, whereas Gibb found 140 pm[72]. For more ionic hydrides such as the hydrides of Rb, Cs, K and Na, hydride is larger than fluoride and values up to 153 pm were reported[54], for lithium and magnesium hydride the hydride and fluoride anion have approximately the same size and in case of more covalent hydrides, hydride becomes significantly smaller than fluoride[27].

2.8.3 The cubic perovskite structure type and Goldschmidt's tolerance factor

A structure type often found in inorganic solid materials is the perovskite structure with ABX_3 stoichiometry[7]. The smaller cation is octahedrally coordinated by six anions, whereas the larger cation is located inside a cuboctahedral arrangement of 12 anions. However, compounds crystallizing in the ideal cubic perovskite structure type such as $SrTiO_3$ are rather rare; even the mineral named perovskite, $CaTiO_3$ is actually a slightly tilted variant[73]. In order to estimate if a structure crystallizes in the ideal cubic perovskite structure type or shows a symmetry reduction[74], a tolerance factor has been introduced by Goldschmidt[75]. The ionic radii must show a certain ratio of their sizes, given by the relationship:

$$r_A + r_X = t\sqrt{2}\,(r_B + r_X) \tag{1}$$

or

$$t = \frac{r_A + r_X}{\sqrt{2}\,(r_B + r_X)} \tag{2}$$

For $0.89 < t < 1$ the ideal cubic perovskite structure is observed. However, the tolerance factor is rather a guiding value than an absolute criterion, since the result depends on the ionic radii that are used and neglects polarization effects. The determination of ionic radii has also been controversially discussed. Different sets of radii have been determined by Pauling, Shannon and Prewitt or Fumi and Tosi[27,76–78] and others. For instance, Fumi and Tosi report the observation of ratios of the cation and anions that are larger than in the traditional set of ionic radii and are believed to better describe the real physical size of a ion in a solid than the effective ionic radius[27]. Due to the controversy concerning the determination of the ionic radii, the interval for the tolerance factor t of 0.9-1.1 is also sometimes given[7] for the ideal cubic perovskite structure type. For $0.8 < t < 0.89$, distorted variants and for $t > 1$ hexagonal perovskites are observed. Values below 0.8 usually lead to the formation of the ilmenite structure type. A doubling of all axes causes a splitting of the $1a$ site into $4a$ and $4b$ and may yield the elpasolite structure type (K_2NaAlF_6).

Tolerance factors for hydrides crystallizing in the perovskite structure type have been evaluated by Wu et al[79]. Effective ionic radii were used and hydride radii were derived from the metal-hydrogen bond either of the B-site or the A-site cation. In a second approach, a constant hydride radius of 140 pm was assumed. The estimations using the first approach yield extremely varying hydride radii and both methods could not explain the experimentally observed existence of the inverse cubic perovskite $LiSrH_3$. However, it should be questioned if the use of effective ionic radii is appropriate for the treatment of hydridic compounds, since the hydride ligand is expected to show a strong covalence.

2.9 In situ DSC

Differential Scanning Calorimetry (DSC) is an isothermal calorimetric method[80]. Heating up sample and reference together and always keeping them at the same temperature, the differences in heat flow are recorded as a function of temperature of the sample.

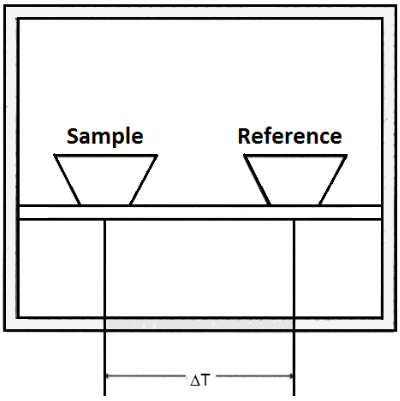

Figure 15: Outline of a differential scanning calorimetry cell. The crucibles for sample and reference are connected with thermocouples.

Sample and reference are placed inside a crucible, for instance an aluminum crucible, each one located on a heatable platform. In case a reaction, phase transition or crystallization takes place, the sample needs to be provided with a different amount of heat compared to the reference. This difference in heat flow can be determined using thermocouples.

For instance, an exothermal reaction or a crystallization yields an exothermal signal, whereas an endothermic signal can be recorded at the melting point of a substance.

The utilized in situ DSC cell features a gas pressure cell holding the measurement setup within, which allows measurements at higher pressure with a reaction gas, such as, e.g., hydrogen. Thus it is possible to study hydrogenation reactions and to determine ideal hydrogenation conditions.

In contrast to hydrogenation reactions inside an autoclave, it is easy to vary temperature and pressure using the DSC cell, which allows for determining the termination of a reaction by studying the heat flows.

2.10 Luminescence

When an electron from an excited state drops to a lower energy state by a radiative transition, the difference in energy is released as a photon, thus resulting in the spontaneous emission of light. In solids this process is called luminescence and, in the special case of a previous absorption of a photon, it is called photoluminescence[81].

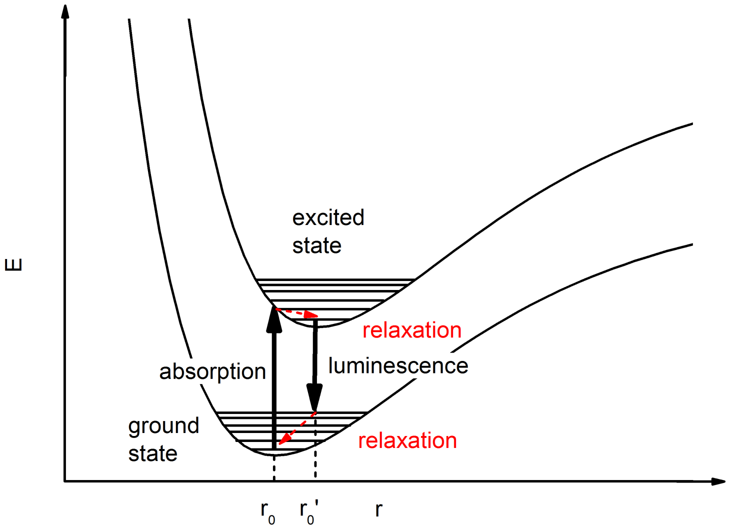

Figure 16: Simplified scheme to illustrate luminescence transitions, displaying ground and excited state as a function of the configurational coordinate r. Modified, after[81].

Applying the Born-Oppenheimer approximation, which states that due to the fact that the nuclei are much heavier than the electrons, the electronic and nuclear motions are separable, one may plot the electronic energy as a function of a configurational coordinate r. As a further consequence of the fact that the nuclei are much heavier than the electrons, the Franck-Condon principle can be applied and therefore the optical transitions can be represented by vertical arrows (see Fig. 16). For the considered coupled vibrational-electronic states the total wave function can be written as a product of an electronic wave function that depends parametrically on the nuclear coordinates and functionally on the electronic coordinates and a vibrational wave function that depends only on the nuclear coordinates. For a given electronic state the vibrational function can simply be described as the wave function of a harmonic oscillator centered at the equilibrium configuration of that electronic state. Assuming that the equilibrium position of the ground and excited state are not the same, we write r_0 for the equilibrium position of the ground state and $r_0^{'}$ for that of the excited state. After the electron is excited, the nuclei adjust their positions to the new equilibrium distances in a non-radiative process (relaxation; indicated by the dotted lines). Subsequently, the system may return to its ground state by emitting a photon, followed by a rapid relaxation reestablishing the equilibrium distances of the ground state. In solids, vibrational relaxations usually occur on a time scale of ps, whereas the re-emission of a photon takes at least about 1 ns. The relaxation processes lead to a loss of the emission energy compared to the absorption energy, which is called the Stokes shift[82].

However, radiative emission is not the only way of reaching the ground state. The excitation energy can also be converted into phonons or via transfer to impurities or defects[81]. In case these processes occur faster than the radiative transition, the luminescent efficiency (or quantum efficiency) η_R will be low.

The rate for spontaneous emission between two levels with a population N of the upper level at the time t is determined by the Einstein coefficient A:

$$(\frac{dN}{dt_R}) = -AN \tag{3}$$

and A^{-1} is the radiative lifetime τ_R of the transition. The total rate equation for the excited state can be written as the sum of the radiative and non-radiative rates with the radiative τ_R and non-radiative lifetime τ_{NR}:

$$(\frac{dN}{dt}) = -N(\frac{1}{\tau_R} - \frac{1}{\tau_{NR}}) \tag{4}$$

The luminescent efficiency η_R can be obtained by dividing the radiative emission rate by the total de-excitation rate:

$$\eta_R = \frac{1}{1+\frac{\tau_R}{\tau_{NR}}} \tag{5}$$

Therefore an efficient luminescence takes place if the radiative lifetime is much shorter than the non-radiative lifetime.

2.11 Vibronic transitions in rare earth spectroscopy

For simultaneous changes of the electronic and vibrational states of a system, so-called vibronic transitions, caused by electron-phonon interactions, are observed[83]. For weak electron-phonon interactions spectra with rather sharp lines are observed, whereas a strong electron-phonon interaction leads to structureless, broad bands.

For a vibronic transition between the states $\Psi(f,n')$ and $\Psi(i,n)$ with n' and n being the final and initial vibrational state and f and i the final and initial electronic states and μ being the electronic dipole or magnetic dipole operator, the matrix element is the following:

$$\langle \Psi(f,n') \mid \mu \mid \Psi(i,n) \rangle \tag{6}$$

At low temperatures only the vibrational level $n = 0$ of the initial electronic state will be occupied. The so-called zero phonon transition is the purely electronic transition with $n = 0$ to $n' = 0$. The vibronic transitions 0 - n' can then be observed at higher energy in the excitation spectra (vibronic transition from $n = 0$ of the electronic ground state to n' in the electronic excited state) and at lower energy in the emission spectra (vibronic transition from $n = 0$ of the electronic excited state to n' in the electronic ground state). Since at higher temperatures vibrational levels other than $n = 0$ are occupied, the vibronic intensities are temperature-depend and so-called anti-Stokes transitions ($n > 0$ to $n' = 0$) can also be observed at higher temperatures. However, within the following work analyses of vibrational fine structures are only carried out for spectra measured at 4K and it will be assumed that only $n = 0$ is occupied. Using the adiabatic approximation and assuming the electronic part to be indepent of the vibrational coordinates, equ. 6 can be separated into an electronic and a vibrational term and becomes:

$$\langle \Psi(f) \mid \mu \mid \Psi(i) \rangle \langle \chi(n') \mid \chi(n) \rangle \tag{7}$$

and for the intensity I applies:

$$I \propto |\langle \Psi(f) \mid \mu \mid \Psi(i) \rangle \langle \chi(n') | \chi(n) \rangle|^2 \tag{8}$$

The electronic matrix element vanishes for electric-dipole radiation in case of intraconfigurational transitions (as ff transitions), but not for df transitions. Considering only inversion symmetry, parity forbidden electronic dipole transitions can be observed if a coupling with *ungerade* vibrational modes takes place, whereas magnetic-dipole transitions can show a coupling with *gerade* vibrations. Thus transitions within the 4f^{n}configuration of rare earth elements are only observed in case those transitions are magnetic-dipole allowed or vibrationally induced. For Eu(II) 4f^{6}d5 - 4f^7 interconfigurational emission, the zero phonon line is an electric-dipole transition so that the strongest vibronic lines will be those coupling with Raman active vibrational modes.

Assuming that the vibrational frequencies in the ground and excited states are equal, but allowing the average values of the configurational coordinates to be different (*linear coupling case*)[84], taking $n = 0$ (for very low temperatures) and summing over n' the shape of the optical transition becomes[83,85]:

$$I_n \approx \frac{e^{-S} S^{n'}}{n'!} \tag{9}$$

with the so-called Huang-Rhys or coupling parameter S and the vibrational quantum number n of the terminal state. S is small ($\ll 1$) for weak coupling and large (20-40) for strong coupling resulting in broad band spectra. For S between 1 and 5 the coupling is of intermediate strength and the zero phonon line is followed by a series of vibronic lines.

2.12 The static crystal field approach and coupling schemes

For the description of spectroscopical interesting centers in inorganic solids, it is convenient to separate the term for the static crystal field and the dynamic crystal field which is due to the vibrational motion of the solid. Here the *static crystal field approach* is presented briefly, for a detailed description see, for instance,[84,86,87]. Since only the outer electrons are involved in optical transitions, the inner electrons can be described as a constant electrostatic field interacting with the outer electrons (*central field approximation*) and the Hamiltonian becomes:

$$\hat{H} = \hat{H}_{FI} + \hat{H}_c \tag{10}$$

$$= \hat{H}_0 + \hat{H}' + \hat{H}_{so} + \hat{H}_c \tag{11}$$

with the free-ion Hamiltonian $\hat{H}_{FI}$, the sum over all N electrons of one-electron operators $\hat{H}_0$, the inner-electron Coulomb interaction $\hat{H}'$, the spin-orbit coupling $\hat{H}_{so}$ and the energy of interactions of the outer electrons with the electrostatic field $\hat{H}_c$. The free-ion Hamiltonian $\hat{H}_{FI}$ is approximated by constructing a spherically symmetric one-electron operator which approximates the potential energy of an electron in the field of the nucleus and the remaining electrons[86]. Summing over the electrons i and the neighboring ions l, the crystal field term can be written as:

$$\hat{H}_c = \sum_i \sum_l \hat{H}_c(r_i, R_l) \tag{12}$$

Depending on the relative sizes of the different terms, 3 methods of determining the *eigenstates* and *eigenvalues* need to be differentiated.

If the crystal field can be considered to be *weak*, e.g. $\hat{H}_c \ll \hat{H}'$, $\hat{H}_{so}$, then the influence of the crystal field is neglected initially, the free-ion Hamiltonian is calculated and afterwards the influence of the crystal field is introduced using pertubation theory. Since the 4f electrons are partially shielded from the lattice by the outer 5s and 5p electrons, neglecting the influence of the crystal field in the first place in case of transitions within the 4f shell is an appropriate approach. The levels of the 4f electrons are then characterized by L, S, J values where some term-mixing is allowed. For large differences between energy separations of different LS terms and the spin-orbit coupling energy, the mixing becomes so small that it can be neglected and Russel-Saunders approximation is valid (LS coupling, S spin angular momentum, L orbit angular momentum). L, S, J and M_J are now good quantum numbers and the splitting of each LS term by spin-orbit coupling leads to a number of states $|LSJM_J\rangle$ with different J and M_J values. Energy levels for trivalent rare-earth ions are tabulated in so-called Dieke digrams[88] where the extent of the crystal field splitting is shown schematically by the width of the levels depicted in the diagram.

For *intermediate* crystal field strengths, where $\hat{H}' > \hat{H}_c > \hat{H}_{so}$, $\hat{H}_{so}$ is neglected in the first place. The matrix elements of $\hat{H}_c$ are calculated using the free-ion L functions as basis functions and from those matrix elements new crystal field orbital states are obtained and multiplied by spin S functions. Afterwards the effect of the spin-orbit coupling is taken into consideration.

For a *strong* crystal field, $\hat{H}_c > \hat{H}' > \hat{H}_{so}$, both $\hat{H}'$ and $\hat{H}_{so}$ are initially neglected so that the Hamiltonian becomes a sum of one-electron orbital terms. Subsequently, the interactions between the electrons and an orbital quantum number Λ are introduced. Λ is the crystal field analogue of the L value for the free ion. The spin states are introduced, which leads to the S parameter. Spin-orbit coupling is then treated as a pertubation.

Since 5d electrons of rare earth ions such as Eu(II) or 3d electrons of transition ions interact strongly with the chemical environment, the influence of the crystal field is much larger or in the same order of magnitude as the influence of the spin-orbit coupling and also often larger than the L-S splitting and therefore it is appropriate to apply the intermediate or strong crystal field approach.

Within the central field approximation a coupling scheme of momentum summation needs to be chosen in order to construct wave functions for the electrons. Two such coupling schemes, one for lighter atoms and one for heavier atoms exist[89,90]. Since the spin-orbit coupling in lighter atoms is small compared to electrostatic interactions between the electrons, L and S are good quantum numbers and the LS or Russel-Saunders coupling scheme is appropriate. In contrast, for heavier atoms the spin orbit interactions are much larger than the Coulomb interactions so that L and S are no longer good quantum numbers and the jj coupling scheme should be considered instead. Since Coulomb and spin-orbit interactions are of the same order of magnitude for rare earth elements, neither coupling scheme is a good approximation. Thus an intermediate coupling scheme developed from the LS coupling scheme is usually applied. The symbol $^{2S+1}\mathrm{L}_J$ is used for naming an electronic state. Since this description does not allow the distinction between states with the same quantum numbers L and S, an additional quantum number τ needs to be introduced. In practice, depending on the irreducible representations of a specific group, two or more additional quantum numbers are needed. Such classification were, for instances, listed by Wybourne[91]. Recently, it was also shown that $4\mathrm{f}^{n-1}5\mathrm{d}$ configurations of the rare earth ions may be modeled using minor modifications to the standard calculations for $4\mathrm{f}^{n}$[92,93].

2.13 Selection rules

Selection rules are discussed briefly, however, the quantum-mechanical approach is beyond the scope of this work and the interested reader is referred to, for instance,[84,86]. In order to determine selection rules, the probability of a radiative transition between states a and b needs to be considered. This probability is proportional to $\langle b|\mu|a\rangle^2$ with μ being the appropriate (electric or magnetic dipole) operator. For an electronic center with inversion symmetry the electric dipole matrix element becomes zero unless the wave functions of a and b are of opposite parity. This requirement is called the *Laporte selection rule*. Since the magnetic dipole operator is of even parity, the magnetic dipole matrix element becomes zero unless a and b are of similar parity. Both the electric and the magnetic dipole operators belong to the J = 1 irreducible representations which results in the selection rule ΔJ = J - J' = 0, ± 1. Furthermore, for a π-polarized transition, ΔM = M - M' = 0 and for a σ-polarized transition ΔM = ± 1 must be fulfilled. Related to the Laporte selection rule, Δl = ± 1 applies for electric dipole transitions, since the components of the electric dipole moment, which are formed from l = 1 spherical harmonics, are of odd parity. The selections rules for an electric dipole transition are ΔS = 0, ΔL = 0, ± 1 with L = 0 $\rightarrow$ L = 0 forbidden. However, transitions between spin-forbidden states may occur in the presence of spin-orbit coupling. Local distortions in the lattice may furthermore destroy the local inversion symmetry so that Laporte-forbidden transitions may become allowed.

Transitions between 4f states are electric-dipole forbidden, since they occur between states of the same parity and are therefore caused by a magnetic dipole process. For crystallographic sites lacking inversion symmetry a mixing with opposite-parity states may occur and lead to an increase in the emission intensity of the transition. Selection rules for electric dipole transitions within the 4f shell can be deduced from the Judd-Ofelt theory: ΔJ $\leq$ 6, ΔS = 0, ΔL $\leq$ 6.

Transitions between the $4f^n$ and the $4f^{n-1}5d$ levels are dipole-allowed and interact strongly with the lattice leading to intense and broad bands.

2.14 Defects and excitons

Looking at phosphors, two different types of defects have to be considered. On the one hand, in case of controlled point defects the solid is doped with a foreign activator cation and on the other hand, inadvertent point and line defects are formed because of impurity and entropy effects[94]. In order to satisfy the law of charge neutrality, the lattice needs to compensate for the charge inequality, if an atom is missing or an extra atom is present. For instance, in case of a cation with an extra charge there needs to be a compensation by a suitable anion or another cation with a lesser charge. Due to the 2nd law of thermodynamics, a perfect solid does not exist above absolute zero temperature and therefore lattices always contain a certain number of point defects. In principle, three major types of defects can occur in a three-dimensional lattice: a point defect (one-dimensional), a line or edge defect (two-dimensional) or a plane or volume defect (three-dimensional). It is assumed that doping of activator ions into host lattices leads mainly to point defects and thus line and volume defects will not be discussed here any further. In a homogeneous solid, several types of point defects may be present: vacancies, self-interstitials, substitutional impurities as well as interstitial impurities. In the last two cases, impurity atoms are involved. An atom that is located in the space between the atoms of the main lattice is called an interstitial and in case an atom of the main lattice is located there, the resulting defect is called a self-interstitial.

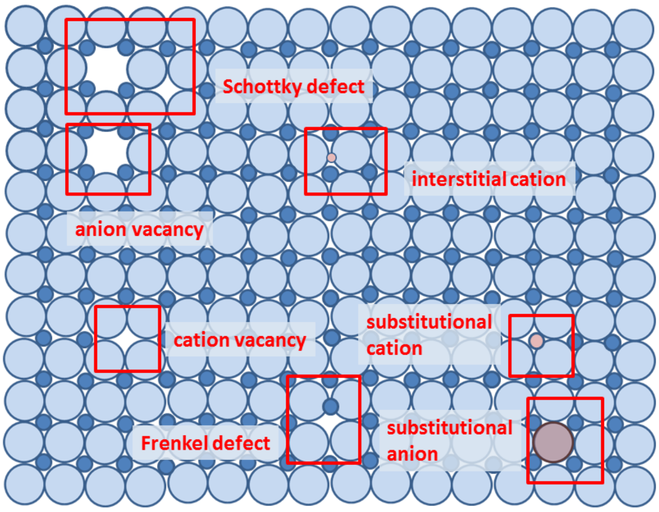

Figure 17: Possible point defects in ionic solids.

In heterogeneous solids the situation is similar, except the fact that there is a charge involved and therefore compliance of the charge neutrality is required and positive charges in the cation sublattice need to be balanced by negative charges in the anion sublattice and vice versa. Due to the required charge neutrality and the presence of two sublattices, possible types of defects are limited to the following: Schottky defects (meaning the absence of both cation and anion), Frenkel defects (meaning a cation vacancy accompanied by the same cation as an interstitial; in case such defect is present in the anion sublattice, it is called Anti-Frenkel-defect), cation and anion vacancies, interstitial impurity atoms (both cation and anion possible) and substitutional impurities (both cation and anion possible). Furthermore, a negatively-charged cation vacancy could capture a positive charge and form a positive hole (h^+) or a positively-charged anion vacancy a negative charge (e^-). An electron trapped at an anion vacany is also called color-center (F-center). The name was chosen because of the electron being optically active, meaning that it is able to absorb light at a well-defined band, thus leading to a specific color of the crystal. It was shown that for the different alkali halides, an inverse relation between the size of the cation (or its polarizability) and the maximum energy of the absorption band exists[81,84]. Additionally, under certain conditions, two F-centers can be combined to form a so-called M-center. Conjoining two color-centers might lead to completely different absorption properties. The absorption of a photon, resulting in the excitation of an electron from the valence to the conduction band in a semiconductor or insulator, at the same time creates a hole in the valence band. The oppositely charged particles can attract each other and the attractive Coulomb interaction increases the probability of the formation of an electron-hole pair, once again resulting in an increase of the optical transition rate. Now it is also possible that a bound electron-hole pair, namely an exciton, is formed[81]. Excitons may be classified into two basis types, the so-called free or Wannier-Mott excitons (see Fig. 18a) and the tightly bound or Frenkel excitons (see Fig. 18b).

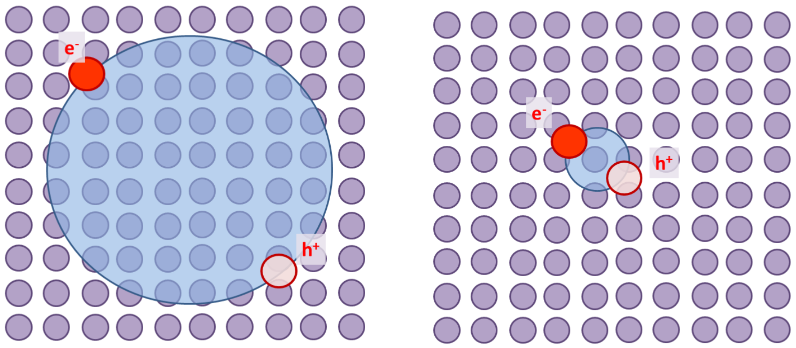

(a) Wannier exciton.

(b) Frenkel exciton.

Figure 18: Free (a) and tightly bound exciton (b).

The former are likely to occur in semiconductors (band gaps of maximal 5eV), their binding energies are in the range of about 10 meV and their radii are much larger than the lattice constants. Therefore they can be described as delocalized states moving freely through the crystal and can be modeled as a hydrogenic system. The latter are mainly observed in insulators and possess binding energies of about 1 eV and radii of the same order of magnitude as the lattice constants. They are therefore localized states and can only move through the crystal by hopping from one site to another. For instance, divalent europium or ytterbium doped into a host lattice could be ionized through the excitation of an electron through the absorption of a photon, leading to a broadening of the emission peak and a large Stokes shift (anomalous luminescence) or luminescence quenching. Here, excitation of the electron to the 5d levels leads to auto-ionization and delocalization of the electron over the surrounding cations and the formation of an trapped exciton-like state near the Eu^{3+} or Yb^{3+} impurity. Then a radiative return to the ground state is in some cases possible via anomalous emission. Various compounds exhibiting anomalous Eu(II) or Yb(II) luminescence have been studied[95]. Anomalous emission is often observed for Yb^{2+} on a Ca^{2+} or Sr^{2+} site, whereas on a Ba^{2+} site often no emission is observed at all. Furthermore, the probability of anomalous emission is also higher for Yb^{2+} than Eu^{2+} and increases with increasing covalence between lanthanide and anions or increasing size of the cation site. It also increases with increasing size of the anions or decreasing size of the lanthanide ion. For instance, normal df emission is always observed for divalent lanthanides on monovalent cation sites and never occurs for divalent lanthanides on trivalent cation sites.

2.15 Luminescence of divalent europium

Unlike the luminescence energies of trivalent rare-earth-ions, those of the divalent lanthanides including Eu(II) depend strongly on the chemical environment. Due to this dependence and the high intensity of the $4f^6 5d^1 \rightarrow 4f^7$ transitions, which are parity allowed and mostly involved in the emission process, the Eu^{2+}-ion shows remarkable luminescence properties[96]. The emission intensity is enhanced up to a factor of 10^6, so that in principle, the Eu(II)-ion is extremely suitable for applications as a phosphor. For instance, $BaMgAl_{10}O_{17}$:Eu^{2+} is used as blue LED in screens. In contrast to the nearly constant emission energies of trivalent europium or other trivalent rare-earth-ions the emission energies depend on the coordination sphere and therefore on the host lattice[97]. In this context different parameters, as the type and number of ligands and their polarizability, the distance of the ligands to the cation, the covalence of the bond, the symmetry, as well as the energetic position of the conduction band, play an important part. The strong dependence of the $4f^6 5d^1 \rightarrow 4f^7$ transition on the coordination sphere originates from the weak shielding of the 5d electrons, which are exposed strongly to the influence of ligands and their crystal field (see, for instance, Fig. 20 and 19). Crystal Field diagrams and d-orbital energy levels are, for instance, given in[87,98,99]. In contrast, the influence of the crystal field on the 4f states is weak, because they are shielded efficiently by the 5s and 5p electrons.

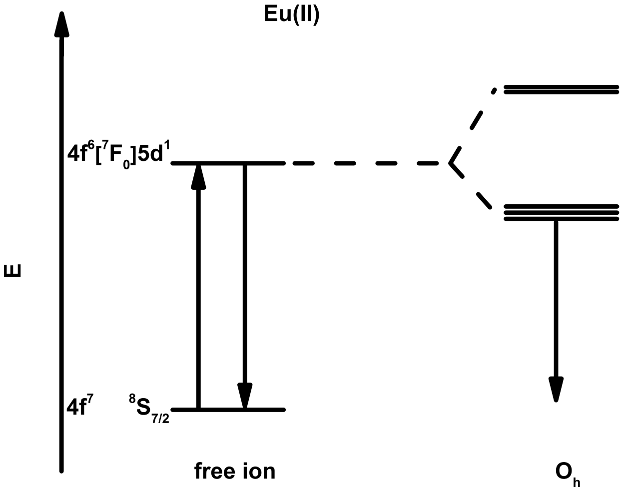

Figure 19: Schematic diagram of Eu(II) in an octahedral environment.

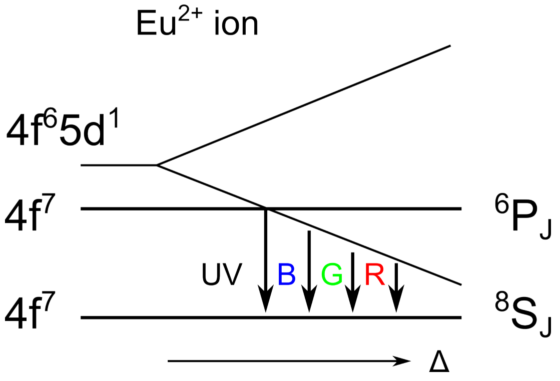

Figure 20: Eu(II) levels depending on the crystal field strength and the resulting emission colors shown schematically.

In case of the 5d states, the factors determining the emission energies can be separated into the contributions from the nephelauxetic effect of the ligands leading to an energetic reduction of the position of the barycenter and the crystal field splitting. In the end, both effects cause a redshift of the emission energy of an ion situated within a coordination polyhedron compared to that of a free ion.

However, the dependence of the luminescence on the constitution of the host lattice has been studied only insufficiently. Up to the present mainly oxides and fluorides have been used as host lattices. For instance, the emission wavelength of SrF_2:Eu^{2+} is 416 nm. Furthermore, a great many of mixed halogenides as, e.g., SrFCl:Eu^{2+} (λ_{em}^{df} = 388 nm) as well as sulfates (SrSO$_4$:Eu^{2+}, λ_{em}^{df} = 376 nm) or oxyhalogenides, such as M$_4$OX$_6$ (M = Sr, Ba; X = Cl, Br; blue emission)[100] are well-known. Anyhow, all these known compounds emit blue or green light; merely nitrides -which are also suitable for applications as phosphors- as well as a few known sulfides and selenides exhibit emission energies in the orange and red spectral region (Ca$_2$Si$_5$N$_8$, λ_{em}^{df} = 616 nm). Furthermore, the relation between the host and thermal quenching of the Eu(II) luminescence, as well as anomalous emission, is still only insufficiently understood.

2.15.1 Different types of Eu^{2+} emission

In order to describe the emission of Eu^{2+}, classifying it into three different types of emission is commonly accepted: normal broad band df emssion, ff narrow line emission and anomalous emission of Eu^{2+}[5].

In all cases excitation to the lowest fd level occurs and the final state of the transition is always the ground state 4f^7 [^{8}S$_{\frac{7}{2}}$]. In case of normal df emission, the dipole- and spin-allowed transition from the relaxed 4f^6[^{7}F$_0$]5d^1 state to the ground state takes place and the absorption and emission spectra show broad bands originating from transitions between the ^{8}S$_{\frac{7}{2}}$ ground state and the crystal field components of the 4f^{6}5d^1 configuration[101].

If the position of the ^{6}P$_J$ states of the 4f^7 configuration is situated below the lowest 4f^{6}5d component and a luminescence quenching due to phonon relaxation to the 4f^7[^{6}P$_{\frac{7}{2}}$] state takes place, no df emission, but only a narrow line emission from [^{6}P$_{\frac{7}{2}}$] to [^{8}S$_{\frac{7}{2}}$], usually around 356 - 364 nm, can be observed. Thus narrow line emission takes place if the barycenter of the crystal field components of the 4f^{6}5d^1 configuration are situated at high energy and the crystal field splitting is small. It is therefore usually observed in host lattices containing fluoride anions, since the nephelauxetic effect of fluoride is weak. Sometimes narrow line emission is also observed together with normal df emission.

A third type of emission can be characterized by an extremely large Stokes shift (5000 - 10.000 cm^{-1}) and emission bands showing a width of more than 4000 cm^{-1}. Additionally, a temperature-dependent variation of the emission takes place. This behavior has been explained by an autoionization of the 5d electron to a conduction band state, leading to the creation of an exciton[102]. The observed anomalous emission can be attributed to an irradiant transition of the electron to

the ground state. However, auto-ionization does not imperatively lead to an anomalous emission, but can also be the reason for the absence of an Eu^{2+}-emission[103].
For instance, this is the case if Eu^{2+} replaces a trivalent cation and charge compensation is not provided by the first anion coordination sphere. This situation leads to a localization of the lowest-energy $4f^6 5d^1$ state inside the conduction bands, resulting in auto-ionization and luminescence quenching after fd excitation. Therefore Eu(II) only shows luminescence on a trivalent cation site if a charge compensation in the first anion coordination shell stabilizes the divalent oxidation state.

2.15.2 Thermal quenching of Eu^{2+} 5d-4f luminescence

Thermally activated quenching mechanisms of Eu(II) luminescence have already been discussed for several decades, since the understanding of thermal quenching plays an important role in the design of phosphors. Several quenching mechanisms, such as a large displacement between the ground and excited state in the configuration coordinate diagram[104,105], thermal excitation of 5d electrons to the conduction band[106] or excitation of holes from Eu(II) to valence band states[107] have been proposed. In case of a large displacement between the two parabolae for the ground and excited state in the configuration coordinate diagram (see Fig.21) a thermally activated radiationless cross-over from the excited state to the ground state can take place.

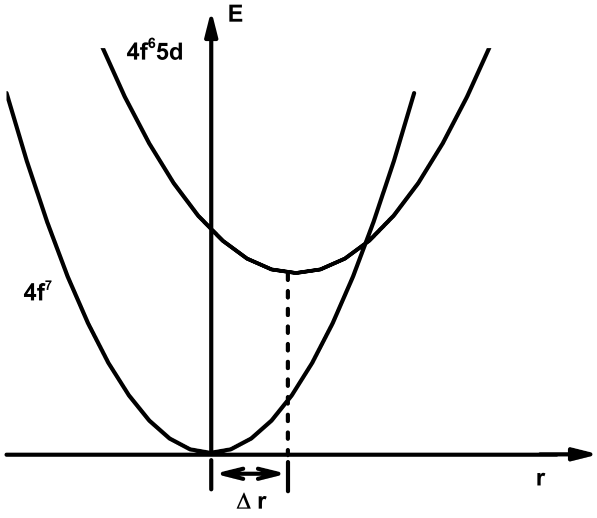

Figure 21: Schematic configurational coordinate diagram for the $4f^7$ and $4f^6 5d$ configuration of Eu(II) according to[105,108].

Here the quenching temperature is strongly correlated with the coupling parameter S[108] and the Stokes shift is supposed to be rather large. The large displacement was often used to explain thermal quenching of Eu(II) on Ba, Sr or Ca sites. For series of alkaline earth compounds the quenching temperature tends to increase with increasing radius of the alkaline earth ion. However it was recently shown that this assumption is wrong and the quenching is caused by the ionization of the 5d electron to conduction band states[103]. If the configuration coordinate model was applicable, a relation between the Stokes shift and the quenching temperature as well as the size of the occupied site should exist. This has been disproven, since the Stokes shift is known for many different compounds[5]. Thermal release of a hole from Eu(II) to the valence band has also been refuted, since it requires a too large energy[109]. In order to prove that the genuine quenching mechanism for Eu(II) doped compounds is the ionization of the 5d electron to conduction band states, Dorenbos[103] studied the relationship between the energy barrier for thermal quenching and the energy difference between the relaxed lowest 5d state and the conduction band. He proposed a model to explain the increase of the quenching temperature with increasing radius of the alkaline earth ion and the occurrence of the reverse behavior in some compounds. Furthermore, he introduces a crude relationship between the quenching temperature $T_{1/2}$ and the energy barrier Δ E:

$$\Delta E = \frac{T_{1/2}}{680} eV \tag{13}$$

In order to clarify the quenching mechanism, the position of the energy levels of Eu(II) and the bands of the host need to be known. An estimation of the position of the Eu(II) 4f and 5d levels can be carried out using the methods presented in[95,110], where the absolute position of the energy levels is obtained from the energy of the Eu(II) df emission and the Eu(III) charge transfer band whose energy corresponds to the energy difference between the top of the valence band and the Eu(II) ground state. Adding the energy of charge transfer to the 5d-4f emission gives the energy of the relaxed lowest 5d states. Furthermore, the position of the bottom of the conduction band needs to be known. Since for some compounds an increase of the quenching temperature with increasing radius of the alkaline earth ion is observed and for some compounds the reverse behavior, two type of compounds are distinguished. In compounds of type (I) the bottom of the conduction band consists of the same cations as the one replaced by Eu^{3+} and for such compounds a strong increase of the band gap with smaller size of the alkaline earth ion is observed (compounds such as $LaAlO_3$ or $GdAlO_3$ are also type (I) compounds). The smaller size of the alkaline earth ion leads to a more negative Madelung potential. As a result of the Madelung potential, the size of the bandgap as well as the energy of charge transfer to Eu^{3+} increase. Since a local lattice relaxation around Eu(III) partly counteracts the effect of changing site size, the bandgap increases faster than the energy of charge transfer, leading to a situation where the energy difference between the lowest 5d state and the bottom of the conduction band increases with smaller site size and the quenching temperature therefore increases in the same order. Type (II) compounds are such compounds where the bottom of the conduction band is formed by cations other than the one replaced by Eu^{3+} (i.e. others than Ba, Sr, Ca), so that a strong dependence of the band gap on the type of alkaline earth ion does not exist and the position of the conduction band stays rather constant. For such compounds the largest Δ E values are observed for the barium compounds, resulting in a decrease of the quenching temperature with smaller size of the alkaline earth cation.

2.16 Luminescence of the activator ions Ce(III), Yb(II), Sm(II) and Mn(II)

As mentioned before (see 2.12), Coulomb and spin-orbit interactions are of the same order of magnitude for the rare earth ions and an intermediate coupling scheme developed from the LS coupling scheme is usually applied. Therefore, terms are often named using $^{2S+1}L_J$ in literature, even though this procedure is, strictly speaking, incorrect, since spin-orbit interactions are not always negligible. However, $^{2S+1}L_J$ terms will also be used in the following.

As the Ce(III) emission originates from a 5d-4f transition, oscillator strengths are usually high. Due to spin-orbit interactions the ground state of the $4f^1$ configuration is a doublet, $^2F_{5/2}$ and $^2F_{7/2}$, resulting in two emission bands separated by about 2000 cm^{-1} [84,111]. Depending on the coordination sphere, the $5d^1$ state is split into several crystal field components[112].

For Yb(II) optical transitions can be observed between the $4f^{13}d^1$ excited state and the $4f^{14}$ ($^1S_0$) ground state[113]. Depending on the coordination polyhedron, df transitions may be formally allowed or forbidden, e.g. transitions between the T_{2u} and E_u in a cubic coordination and the ground state are forbidden. However, the exchange interaction between the 5d electron and the remaining $4f^{13}$ is relatively weak and the lowest levels of the $4f^{13}d^1$ contain both low and high spin LS terms. Therefore it is impossible to clearly distinguish spin-allowed and spin-forbidden transitions and spectra often show bands that can be assigned to a spin-forbidden transition. Calculating the energy level scheme of the $4f^{13}d^1$ is complicated, since the crystal field and the spin-orbit coupling on the free ion states both play a role[114]. Such calculations have been carried out based on LS coupling[115] as well as a jj-coupling scheme[116]. In contrast to Eu(II), Yb(II) often exhibits anomalous emission, which is only deficiently understood until now[82,95]. For Sm(II) band luminescence is observed when the $4f^5 5d^1$ state is located below the lowest excited ^5D_J level of the $4f^6$ levels. In case of relaxation from the df state to the $4f^6[^5D_J]$ df emission is quenched and only ff line emission can be observed[117]. As the lowest excited state ^5D_J of the $4f^6$ is -even for strong crystal fields- often located at lower energies than the $4f^5 5d^1$ state, the observation of broad band emission is rather rare[118]. Due to spin-orbit interactions the $4f^6$ ground state splits into ^7F_J with J = 0-6[119].

Mn(II) has $3d^5$ configuration and the free ion ground state is a sextet ^6S[82,84]. Since the location of the $^4T_1$ and $^4T_2$ levels strongly depend on the crystal field strength, an increase in the crystal field strength leads to a shift in the energy of the $^4T_1$-$^6A_1$ and $^4T_2$-$^6A_1$ transitions. Thus tetrahedrally coordinated Mn(II) usually emits green light, octahedrally coordinated Mn(II), however, emits in the red color region[82,120].

2.17 Stray light in monochromators

Beside the desired wavelength, stray light of an intensity comparable to the luminescence of a sample may pass through the excitation monochromator and subsequently be scattered. They shattered light may then interfere with measurements. Especially in case of weakly emitting biological samples or powder samples it is therefore often necessary to use a double-grating monochromator for the excitation which limits the stray light intensity to 10^{-8}-10^{-12} of the intensity of the sample[121]. However, the use of a double-grating monochromator also leads to a loss in intensity. Additionally, in some cases it may be necessary to also use a double-grating monochromator on the emission side. This is especially the case for weakly emitting samples.

3 Experimental details

3.1 Synthesis

Due to the moisture and air sensitivity all utilized metals, intermetallics and hydrides were handled in an argon-filled glove box. The metal hydrides were prepared by hydrogenation of the corresponding intermetallic compounds or alloys, which had been synthesized through melting reactions or via solid state synthesis, under hydrogen pressure.

For melting reactions, the metals were superficially cleansed from oxide by means of a milling cutter. The alloys were prepared by reaction of the metals in sealed niobium tubes. The melting reactions were conducted by enclosing the niobium tubes in sealed silica ampoules at temperatures of 750-940°C depending on the system. The samples were kept slightly above their melting temperatures for approx. 4h and subsequently quenched to room temperature. However, the intermetallic compounds were not investigated by X-ray diffraction, because they could not be ground due to their hardness and toughness. Therefore, in the following, the compositions of the samples from melting reactions will be assumed to be equal to the nominal compositions and alloys were processed into hydrides without further investigation.

Hydrogenation reactions were carried out either in an autoclave at temperatures from 600 to 800 K and hydrogen pressures of 40-150 bar or in a DSC chamber at maximal 720 K and 50 bar hydrogen pressure.

Fluorides, mixed hydride-fluorides and mixed hydride-chlorides were obtained via solid state reaction carried out in an inert or hydrogen gas atmosphere. Mixed compounds were either prepared at 800 K and 20-60 bar hydrogen pressure in an autoclave or at up to 1000 K and 15 bar in a silica high pressure cell.

3.2 Technical equipment and methods

3.2.1 Glove Box

All works under argon were carried out in a glove box of mbraun featuring a copper catalyst, as well as molecular sieve for the removal of oxygen and water. These were recycled using Hydrostar (hydrogen argon mixture) at regular intervals.

3.2.2 Gas tungsten arc welding

Welding up the used niobium tubes was carried out via gas tungsten arc welding in a self-construction. The argon pressure while welding was 350 - 400 mbar and the current 20 A; a Lymox® electrode (tungsten-rare-earth-alloy) was used.

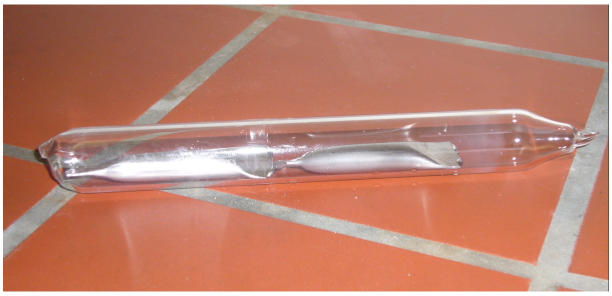

Figure 22: Sealed niobium tubes enclosed in a sealed silica ampoule.

3.2.3 Autoclave

Hydrogenation reactions were carried out in a self-construction autoclave made of *Nicrofer® 5219 Nb-alloy 718*, which is corrosion-resistant even at high hydrogen pressures and temperature resistant up to 600°C. For heating, a calibration up to 650°C relating the oven temperature with the temperature measured inside the autoclave was carried out using a self-made top for insertion of a thermocouple.

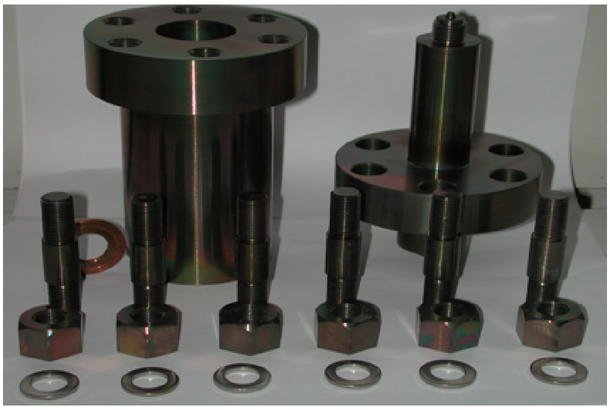

Figure 23: Autoclave, fragmented.

3.2.4 Sapphire single crystal high-pressure cell

For *in situ* neutron diffraction experiments, a sapphire single crystal gas pressure cell with a contactless laser-heating system especially developed for *in situ* neutron powder diffraction[122–125] was used. Due to its chemical intertness against hydrogen and the studied samples, mechanical strength as well as its low incoherent scattering and absorption cross section for thermal neutrons, the gas pressure cell is well-suited for *in situ* hydrogenation studies at high pressures and elevated temperatures. The cells were made of sapphire single crystals grown along the crystallographic axes c or tilted up to 15° with respect to the c axes. The flanges on both ends were closed by stainless steel end caps sealed with indium or lead wires and connect the cell to a gas delivery system. Samples are enclosed in a 6 mm diameter borehole and heated contactlessly with two laser beams.

Figure 24: Sapphire gas pressure cell.

Temperature calibration was carried out comparing refined lattices constants of palladium powder in the range between 25°C and 400°C as indicated by the pyrometer with the temperature dependence of palladium's lattice parameters[126] and yielded the following temperature calibration: $T_{cal} = 8.0(7)°C + 0.941(8) T_{pyro} - 0.00029(2)°C^{-1} T_{pyro}^{2}$[124]. Furthermore, a second calibration curve of the pyrometer was obtained from temperature dependent neutron diffraction measurements of silicon (325 mesh, 99.999%, Johnson & Matthey) and refinement of its unit cell parameters. The calibration $T_{cal} = 11(10)°C + 0.7(2)T_{pyro} + 0.0004(1)°C^{-1}T_{pyro}^2 - 8(1) \cdot 10^{6}°C^{-2}T_{pyro}^3$ was obtained through comparison of the refined data with data from X-ray powder diffraction[127,128]. A proper orientation of the cell allows the removal of the single crystal Bragg reflections from the scattering plane of the diffractometer. A favorable orientation is chosen via a preliminary omega scan of the cell (for an example, see Fig. 25). However, diffuse scattering due to phonon excitations also occurred so that in some cases small regions in the 2θ range need to be excluded.

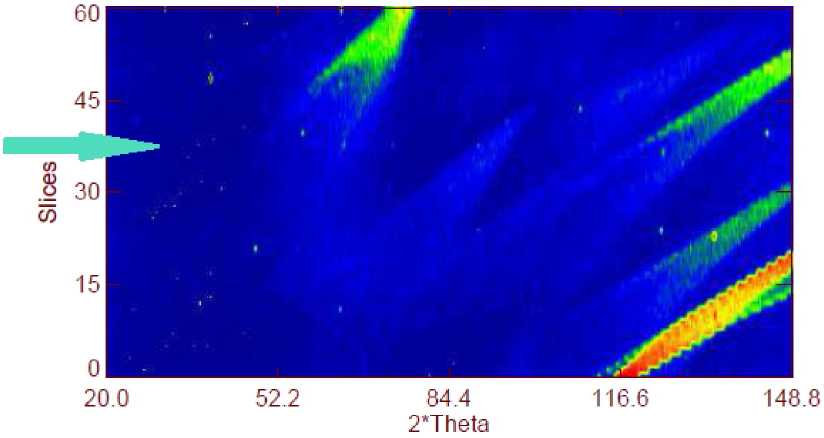

Figure 25: Omega scan (in false colors) of the empty single crystal sapphire high pressure cell GlaBa07 at the D20/ILL, 15° inclination angle with respect to the c-axis. Measuring position marked by arrow.

3.2.5 Silica high-pressure cell

For reactions at temperatures far above 400°C and high hydrogen pressures, silica high-pressure cells based on the design of the sapphire cell were used *ex-situ*. The lengths of 250 - 350 mm in contrast to the 10 mm length of the sapphire cell allows a heating to higher temperatures, since a melting of the indium or lead seals is avoided. The cells permit heating with the contactless laser system as well as tube furnaces as long as the end caps and the seals are sufficiently protected from heat. Tests confirmed leak tightness with indium seals up to approx. 800°C and 15 bar hydrogen using the laser-heating system and 650°C and 12 bar hydrogen using a tube furnace. In case the cell was not inert against the reactants, a stainless steel crucible was used.

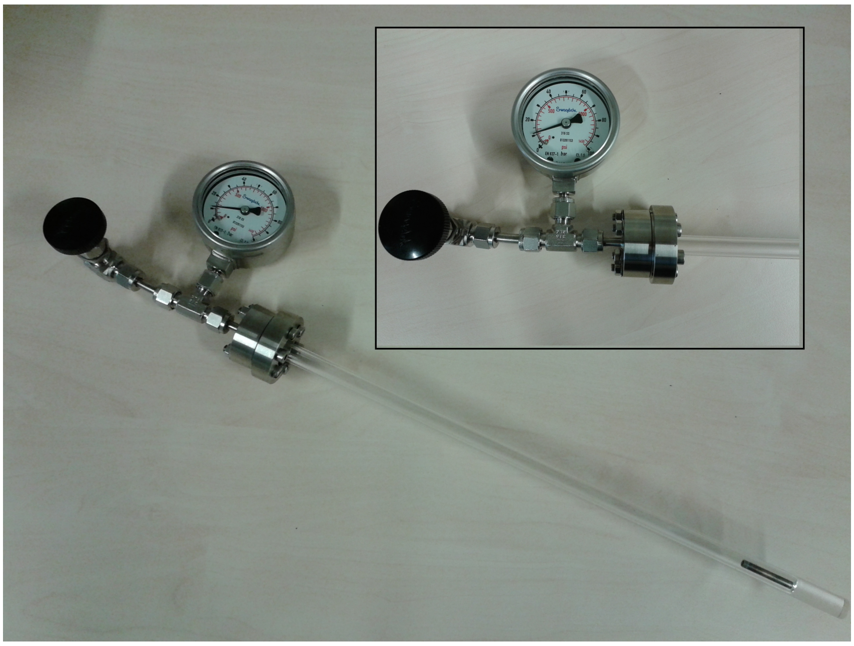

Figure 26: Silica gas pressure cell with stainless steel crucible.

3.2.6 DSC

Preparation via DSC was carried out using an instrument of TA Instruments, model Q1000 featuring a high pressure chamber for hydrogen pressures up to 70 bar. Due to the air sensitivity of the examined samples, measurements were carried out within sealed aluminum pans. To assure the completion of the reactions, measurements were repeated at least once or twice.

Hydrogenation conditions were 450°C and about 50 bar hydrogen pressure (see Fig. 27). Anyhow, the chosen cooling rate could not be assured due to the fact that the instrument does not possess an active cooling system.

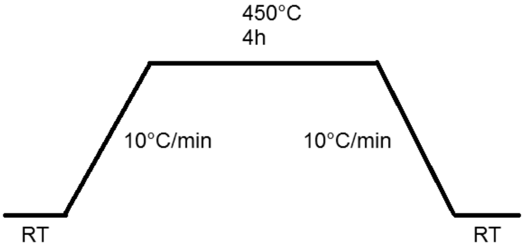

Figure 27: Temperature program of a hydrogenation reaction within the DSC at about 50 bar.

3.2.7 X-ray diffraction

X-ray powder diffraction data at RT were collected on a Panalytical Philips *X'Pert Pro* diffractometer with focusing Bragg-Brentano geometry and a fine focus X-ray tube (CuK$\alpha_{1,2}$ radiation), a Bruker *D8 Advance* with *Lynxeye* with focusing Bragg-Brentano geometry and a fine focus X-ray tube (CuK$\alpha_{1,2}$ radiation) and a Guinier camera (Huber G670, CuKα_1 radiation). Low temperature XRD measurements were carried out on a Guinier camera (Huber G670, CuKα_1 radiation) with cryostat within the group of PD Dr. Richard Weihrich at the University of Regensburg. To determine the zero shift of the G670 in the RT measurements, silicon was used as internal standard. Samples were enclosed between kapton foils (or aluminum in case of low temperature measurements) with apiezon grease. The data collection time was 30-60 min depending on the sample, diffraction range was 10 - 110° 2θ, below 22° 2θ an increased background occurred due to the sample preparation.

Crystal structures were refined using the program packet FullProf[129] according to the Rietveld method[130] or using TOPAS 2.1 (Bruker AXS, Karlsruhe, Germany)[131]/TOPAS 4.1[132] and the fundamental parameter approach[133]. In FullProf the profile fitting was carried out using a pseudo-Voigt function. The background was described either using a polynomial or linear interpolation. The ratio of CuKα_1 and CuKα_2 was determined using a silicon standard (NIST 640d). In TOPAS, the instrumental function was determined empirically by means of a reference scan of LaB$_6$. Typically, complete structures including hydrogen positions from literature were taken as starting structures and scale factors, lattice parameters, atomic positions of the metal atoms and microstructural parameters were refined. An overall B-value or coupled B-values were used in order to minimize errors in quantitative phase analysis. If not indicated otherwise, ratios given in the refinement plots obtained using TOPAS are given in weight percentage. ε_0 as obtained by TOPAS is specified in case a measure of the mean strain is used in discussion.

3.2.8 Neutron powder diffraction

Neutron powder diffraction measurements were carried out at the Institute Laue-Langevin in Grenoble, France at the high-flux powder diffractometer D20 in high resolution mode in the range $3° \leq 2\theta \leq 150°$ (resolution $2\theta = 0.1°$). Usually, the wavelength of about 1.867 $\AA$ was kept fix during measurements and determined exactly for each experiment from a measurement of a silicon standard (NIST640b). For standard measurements of hydrides samples were enclosed in vanadium cylinders sealed by an indium wire and handled in an argon-filled glovebox. For *in situ* studies at high deuterium pressure and high temperatures, sapphire single crystal high-pressure cells together with a contactless laser heating system were used. The crystals had varying cutting directions with respect to the crystallographic c-axis. Omega scans were taken of the empty cells and a favorable position was chosen for the measurements. Data processing was carried out using the program LAMP[134,135]. Structural refinement was carried out with TOPAS 4.2 using both neutron data and XRD data, if available. The same positional, size and strain parameters were used. The instrumental function for the neutron data was determined empirically by means of a reference scan of a Si standard (NIST640b).

3.2.9 Luminescence measurements

Photoluminescence emission and excitation spectra were carried out on different luminescence spectrometers.

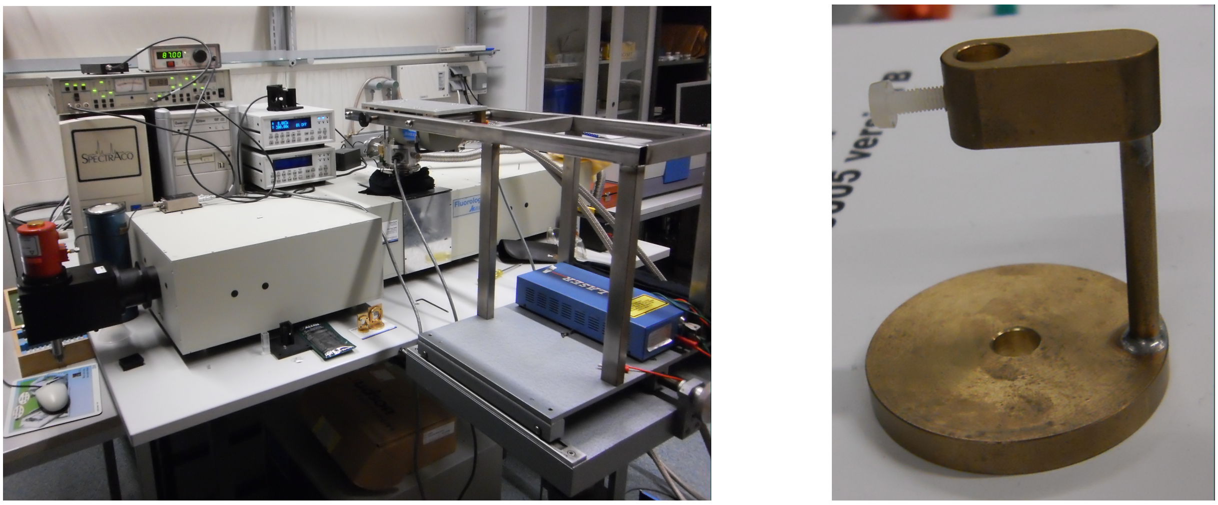

(a) Fluorolog 3-22.

(b) Sample holder.

Figure 28: Luminescence spectrometer FL3-22 with closed-cycle helium cryostat (a) and self-constructed sample holder (b).

Spectra of the alkaline earth metal hydrides containing 0.5 mol% europium were recorded in Siegen on a luminescence spectrometer (FL3-22, Jobin Yvon) equipped with two double monochromators according to Czerny-Turner (1200 grooves per mm) for the excitation beam and UV/Vis emission and a monochromator (600 lines per mm) for NIR emission, a 450 W Xenon lamp for sample excitation and a 75 Xenon lamp for life-time measurements. Depending on the chosen width of slit, a resolution of 0.05 nm, respectively 0.2 nm, for luminescence and excitation spectra can be achieved. For detection, two different detectors were used. UV/Vis luminescence was detected via a photomultiplier R928P (Hamamatsu); NIR luminescence was detected via a nitrogen-cooled InGaAs diode (J23D, Judson). Spectra were corrected for photomultiplier sensitivity as well as for lamp intensity. Noise suppression in the NIR range was carried out using lock-in-technology (SR 510, Stanford Research). Correction of the lamp intensity is warranted only up to 1650 nm (due to the calibration of the lamp) and of the excitation spectra only up to 600 nm (due to the determination of the correction factor using Rhodamine B). For low temperature measurements at 10 K a liquid helium closed cycle cryostat was used. The signal at 790 nm in the UV/Vis spectra at 10 K is an artifact originating from the cryostat. All remaining excitation spectra, as well as higher resolution emission and excitation spectra, most room temperature emission spectra and life time measurements were carried out in Utrecht. Photoluminescence emission and excitation spectra were measured on a Edinburgh Instruments FLS920 spectrofluorometer equipped with a double monochromator according to Czerny-Turner (300 mm focal length) for the excitation beam, a monochromator for UV/Vis emission and a 450 W Xenon lamp for sample excitation. For detection, a photomultiplier tube R928P (Hamamatsu) was used. Wavelength accuracy was determined via calibration with a standard. The wavelength accuracy of the excitation wavelength lies within a range of errors of 0.5 nm, whereas the emission wavelengths are slightly shifted to higher energies (between 1.5 nm and 3 nm). Whenever a well-resolved vibronic fine structure was available, the emission wavelength was therefore shifted so that the positions of the zero-phonon lines in the excitation and emission lines were identical. For low temperature measurements an Oxford liquid helium flow cryostat was used. Luminescence decay curves were measured under pulsed excitation with a Edinburgh 376.8 nm pulsed diode laser (65 ps pulses). Luminescence decay curves were analyzed using a single exponential function, even though for some samples the curves in the higher temperature region for partly quenched luminescence deviate slightly from single exponential behavior; for an example of such fit see Fig. 30.

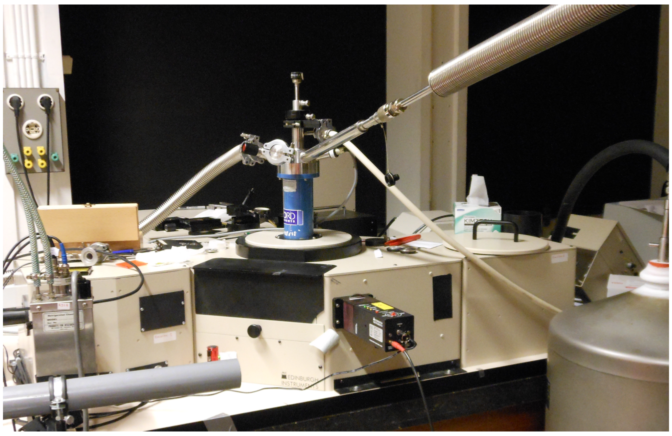

Figure 29: Luminescence spectrometer FL9-20 with helium flow cryostat.

Furthermore, photoluminescence spectra were recorded on a FluoroMax 4 spectrometer (Horiba Jobin Yvon) equipped with two monochromators (1200 grooves per mm) for the excitation beam and UV/Vis emission and a 150 W xenon arc-lamp for sample excitation. For detection, a R928P photomultiplier with response from 180-850 nm was used. Spectra were corrected for photomultiplier sensitivity as well as for lamp intensity. Data collected on the Fluoromax 4 were mainly used for making a pre-selection of samples to be measured in higher resolution mode. In case no comparable spectra measured at another spectrometer are shown, spectra measured at the FluoroMax4 will be given in the appendix (see Sect. 8.3).

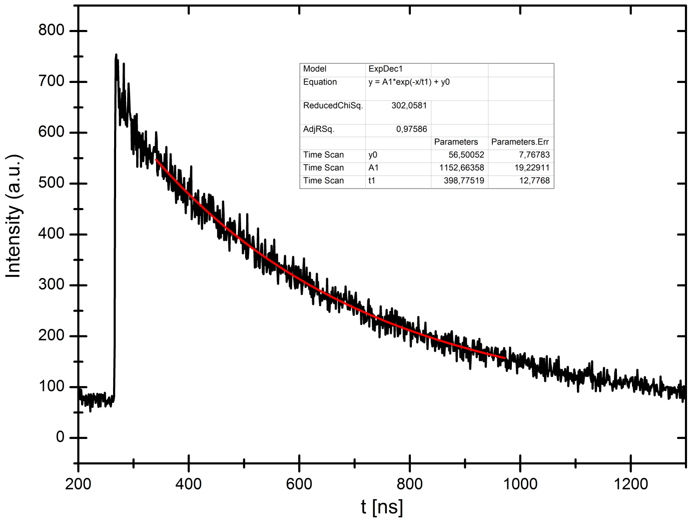

Model	ExpDec1		
Equation	y = A1*exp(-x/t1) + y0		
ReducedChiSq.	302,0581		
AdjRSq.	0,97586		
		Parameters	Parameters.Err
Time Scan	y0	56,50052	7,76783
Time Scan	A1	1152,66358	19,22911
Time Scan	t1	398,77519	12,7768

Figure 30: Decay curve at 42 K of $LiSrH_3:Eu^{2+}$, emission at 580 nm.

3.3 Materials

The starting materials used in the syntheses were europium ingot (Alfa Aesar, 99.9%), strontium rod or pieces (oddments of unknown origin, probably 99.9% or Alfa Aesar, 99.8%), calcium pieces (Alfa Aesar, 99.5%), barium pieces or rods (Sigma Aldrich, 99.9% or Chempur, 99.3% (rest strontium)), magnesium rod or powder (Chempur, 99.999% or ABCR, 99.8% under argon), ytterbium ingot (Alfa Aesar, 99.9%), lithium wire (Alfa Aesar, 99.8%), potassium (ABCR 99.95%), manganese powder (Merck), KH (Aldrich, 50 wt % in paraffin, washed several times with hexane), MgH_2 (Alfa Aesar, 98%), LiH (Acros Organics, 98%), NaH (Sigma Aldrich, 95%), LiF (Merck, 99%), SrF_2 (abcr, 99.99%), BaF_2 (Aldrich, 99.99%), MgF_2 (abcr, 99.99%), EuF_2 (Alfa Aesar, anhydrous, 99.9%), $EuCl_2$ (Sigma Aldrich, 99.99%) and hydrogen/deuterium (Praxair, 99.9%). Niobium tubes from Plansee, E. Wagener or Holdenrieder (99.70%, 99.95%, 99.95%) were used. Argon (Praxair, 99.996%) was utilized as inert gas and Hydrostar (Praxair) for the regeneration of the glove box.

4 Experimental results and discussion

In the following the synthesis and characterization for every host lattice system and -in case of investigation using *in situ* DSC- the optimized hydrogenation conditions will be cited. Subsequently, in case of the samples with low europium content and the occurrence of luminescence, the luminescence properties such as luminescence excitation and emission spectra as well as lifetime measurements will be depicted and discussed. Generally, europium doping rates are quoted according to the initial weight of the educts, for ternary hydrides the mol percentage is defined in relation to the ion whose site europium is presumed to occupy. However, it has been shown in another work carried out within our group regarding the analysis of europium containing samples via ICP-MS[136] that those assumptions are valid within a small range of errors for the complete system $Eu_xSr_{1-x}H_2$ and random samples of the system $LiEu_xSr_{1-x}H_3$. It is therefore assumed that the nominal europium content is equivalent to the actual content with possible small deviations.
Furthermore, *in situ* neutron diffraction experiments investigating the hydrogenation behavior of YbH_x or YbD_x under high hydrogen pressures are reported.

4.1 Eu-doped alkaline earth metal hydrides

4.1.1 $Eu_xSr_{1-x}H_2$

The complete solid solution series $Eu_xSr_{1-x}H_2$ and it structural parameters was the subject of another work[34,35]. However, as the luminescence properties of samples with small x have been investigated during the present work, structural parameters of samples relevant for luminescence studies shall be listed here briefly. Refined lattice constants are listed in Table 1. The hydrides were obtained as colored powders via hydrogenation of the corresponding alloys or intermetallic compounds in an autoclave at 230°C and 270 bar for about 3 days. A transition of color from white SrH_2 via orange and red towards dark purple EuH_2 could be observed. X-ray powder diffraction data were collected on a Panalytical Philips *X'Pert Pro* diffractometer, Guinier camera (Huber G670, $CuK\alpha_1$ radiation) as well as a Bruker *D8 Advance*; Rietveld refinement was carried out using FullProf and TOPAS. The red luminescence is weak and could hardly be observed with the naked eye for some samples. Europium is assumed to occupy the strontium site within the tricapped trigonal prism formed by hydrogen ligands. Ignoring the effects of doping on the cell volume, the europium-hydrogen distances vary from about 235 pm to 271 pm.

Table 1: Refined lattice constants of the system $Eu_xSr_{1-x}H_2$, space group *Pnma*, X-ray data collected at the G670 (left) and the *X'Pert Pro* diffractometer (right). Estimated standard deviations provided by the program FullProf are given in brackets.

x	a [pm]	b [pm]	c [pm]	a [pm]	b [pm]	c [pm]
0.0	637.76(2)	386.78(1)	732.73(2)	638.84(4)	387.47(2)	733.83(5)
0.002	-	-	-	637.31(1)	386.95(1)	732.20(1)
0.005	637.09(4)	386.53(1)	733.37(5)	637.62(3)	386.08(2)	732.57(3)
0.01	637.80(1)	387.261(9)	731.76(2)	638.66(4)	387.68(2)	732.82(4)
0.02	637.73(2)	387.27(1)	731.65(2)	638.09(3)	387.25(1)	732.30(3)

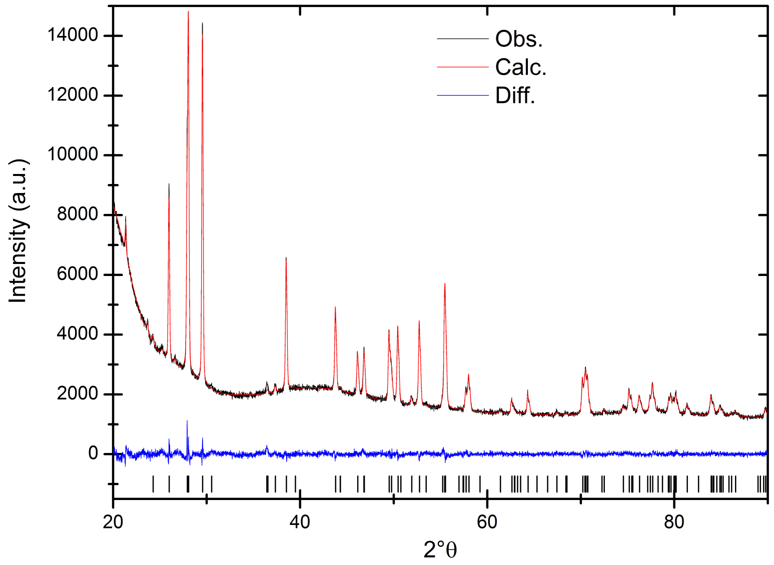

Figure 31: Rietveld refinement of the crystal structure of SrH_2, data recorded at the Bruker *D8 Advance*.

4.1.2 CaH_2:Eu^{2+}

The hydrides CaH_2 and CaH_2:Eu^{2+} (0.5 mol%) were obtained purely as powders through hydrogenation of the corresponding alloys at about 300°C and 60 bar for about 3 days. In contrast to white CaH_2, samples doped with europium exhibit a reddish color. The Rietveld refinement of CaH_2:Eu^{2+} (0.5 mol%) and the refined lattice constants are listed in Fig.32 and Table 2.

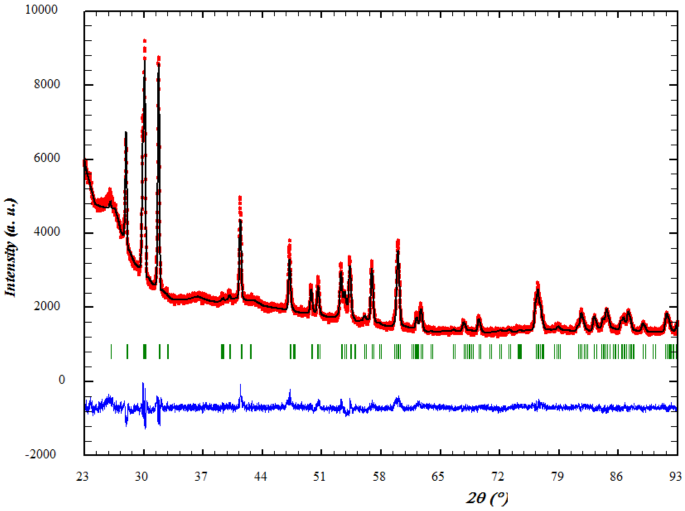

Figure 32: Rietveld refinement of the crystal structure of CaH_2:Eu^{2+} (0.5 mol%), data recorded at the Huber G670.

Table 2: Refined lattice constants of the system $Eu_xCa_{1\text{-}x}H_2$, space group *Pnma*, X-ray data were collected on the *X'Pert Pro* diffractometer. Estimated standard deviations provided by the program FullProf are given in brackets.

x	a [pm]	b [pm]	c [pm]
0.0	594.47(5)	359.20(2)	680.47(5)
0.005	596.35(2)	360.43(1)	681.90(2)

Similar to SrH_2, europium is assumed to occupy the calcium site within the tricapped trigonal prism formed by hydrogen ligands. Ignoring the effects of doping on the cell volume, the europium-hydrogen distances vary from about 205 pm to 270 pm.

4.1.3 BaH_2:Eu^{2+}

The hydrides BaH_2 and BaH_2:Eu^{2+} (0.5 mol%) were obtained purely as powders through hydrogenation of the corresponding alloys at about 300°C and ca. 85 bar for about 3 days. In contrast to white BaH_2, samples doped with europium exhibit a yellow color. Refined lattice constants are listed in Table 3.

Table 3: Refined lattice constants of the system $Eu_xBa_{1-x}H_2$, space group *Pnma*, X-ray data were collected on the *X'Pert Pro* diffractometer. Estimated standard deviations provided by the program FullProf are given in brackets.

x	a [pm]	b [pm]	c [pm]
0.0	681.59(8)	416.78(3)	787.34(7)
0.005	680.74(4)	417.04(2)	787.01(5)

For europium on the barium site (tricapped trigonal prismatic coordination polyhedron) the europium-hydrogen distances vary from about 249 pm to 302 pm.

4.1.4 Luminescence spectra of the Eu(II)-doped earth alkaline hydrides

Luminescence measurements of CaH_2:Eu^{2+}, SrH_2:Eu^{2+} and BaH_2:Eu^{2+} (0.5 mol%) yielded an emission with a peak maximum of 765 nm, 728 nm and 755 nm, respectively (see Fig. 33)[35]. The broad band in the emission spectrum can be assigned to the $4f^65d^1 \rightarrow 4f^7$ transition of Eu(II). A strong redshift of the emission energy compared to well-known emission energies of divalent europium can be observed, representing the widest redshift in calcium, strontium or barium containing host lattices, respectively, so far known. It is due to the fact that the hydride ligand is considerably softer and therefore more polarizable compared to fluoride or oxide, leading to a larger nephelauxetic effect. Therefore the 5d states experience an energetic reduction, causing a reduction of the emission energy.

Comparing the emission bands of the three Eu(II)-doped alkaline-earth hydrides, those for M

= Ca and Sr show very similar shape, with a 36 nm shift to longer wavelengths for the calcium compound. This shift might be explained by the smaller unit cell volume of the calcium compound, in which the hydride anion can exert an even stronger ligand field effect on Eu(II). However, for the barium compound, the emission band shows a slightly different shape and its position is in between those of M = Ca and Sr. The difference might be explained by the fact that the Ba position in BaH_2 is too large for the Eu^{2+} ion[10], thus realizing a different environment from Ba for instance by a local relaxation of the structure or by the occupation of different lattice sites. The larger band width in case of the barium compound is also consistent with the frequent observation of the so-called anomalous emission[95] occurring in europium- or ytterbium-doped barium compounds and resulting in large Stokes shifts and band widths. Since the coordination polyhedra of the metal ions in MH_2 (M = Sr, Ba) or EuD_2[11] are tricapped trigonal prisms, they are approximately comparable with the coordination polyhedron observed for the $[ReH_9]^{2-}$ anion in K_2ReH_9[18], even though the metal-hydride interatomic distances vary slightly. Absolute values for the energetic positions of the d orbitals of $[ReH_9]^{2-}$ were never determined, however, numerical values for the relative energies were calculated in terms of D_q for $\rho = 2.0$[99]. According to those calculations, the d_{z^2} is located at -2.55 in units of D_q, the $d_{x^2-y^2}$ and d_{xy} at -0.38 and the d_{xz} and d_{yz} at 1.51. Compared to 6.0 for the e_g and -4.0 for the t_{2g} in an octahedral environment, this splitting is rather small. Since the excitation spectra consist only of broad bands, it is not possible to assign different d-levels. However, taking the calculated relative splitting of the $[ReH_9]^{2-}$ d levels as a crude estimation, the crystal field splitting seems to play only a minor role in the redshift of the emission. In contrast, a large shift of the barycenter of the Eu(II) 5d levels to lower energies due to the strong covalence of the hydride anion and thus a strong nephelauxetic effect might be a reasonable explanation.

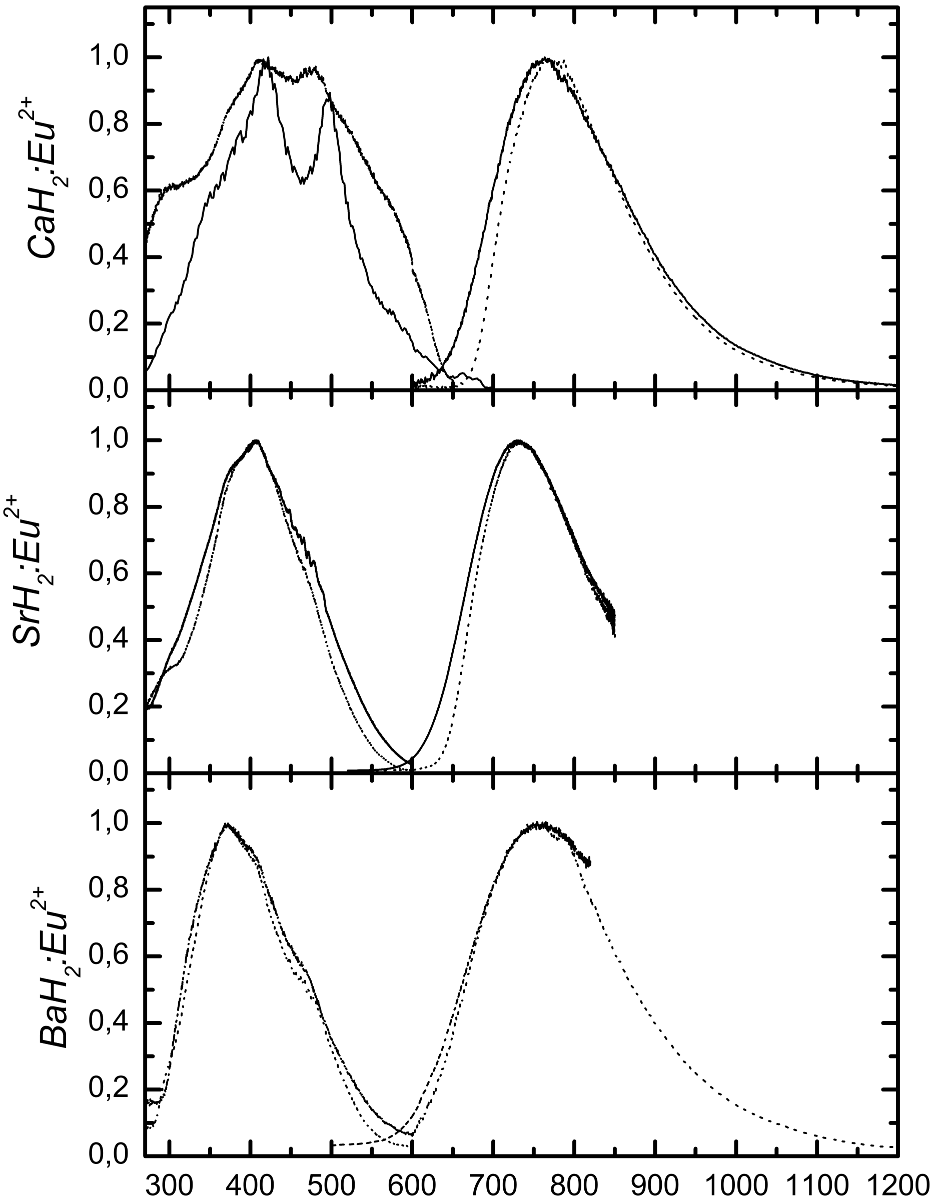

Figure 33: Luminescence spectra (FL322) of $MH_2:Eu^{2+}$ (M = Ca, Sr, Ba) with 0.5% europium at 10 and 300 K; excitation at 420 nm for M = Ca, Ba and 390 nm for M = Sr. Solid: emission and excitation at RT, dotted: emission and excitation at 10K. Intensities are normalized.

4.2 Eu-doped perovskite-type hydrides

4.2.1 $LiSrH_3$:Eu^{2+} and $LiSrD_3$:Eu^{2+}

The alloys $LiEu_xSr_{1-x}$ were prepared by melting reactions of the corresponding elements and hydrogenated or deuterated at approx. 300°C and hydrogen or deuterium pressures of 70-180 bar for about 4-5 days. $LiEu_xSr_{1-x}H_3$ and $LiEu_xSr_{1-x}D_3$ were obtained as light yellow powders showing an intense yellow emission[137]. The europium-free sample $LiSrH_3$ was obtained as a white powder and did not exhibit any visible luminescence confirming that the bright yellow emission originates from Eu(II) emission.

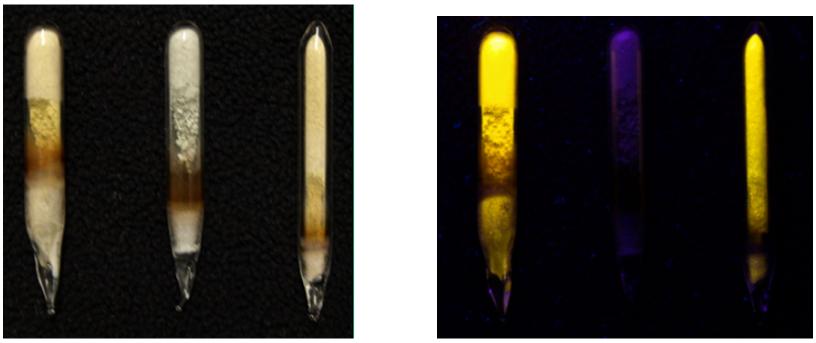

(a) At daylight.

(b) Under UV-excitation.

Figure 34: From left to right: $LiSrD_3$:Eu^{2+} (0.5 mol%), $LiSrH_3$, $LiSrH_3$:Eu^{2+} (0.5 mol%) at daylight (a) and under UV excitation (b).

$LiSrH_3$ as well as $LiSrD_3$ crystallize in the cubic inverse perovskite structure type, where strontium is surrounded by twelve hydrogen or deuterium atoms in a cuboctahedral arrangement. Europium may be expected to be divalent and occupy the high symmetry site ($m\bar{3}m$) of strontium. The inverse cubic structure type has been confirmed unambiguously via neutron powder diffraction experiments that were carried out on the high-flux diffractometer D20 at the Institute Laue-Langevin (Grenoble, France) in high resolution mode with total data collection times of 20 minutes each. The lattice constants and interatomic distances obtained assuming a statistical occupation of the strontium site 1*b* by europium and strontium are listed in Table 4. Exemplary, the Rietveld refinement of $LiSrH_3$:Eu^{2+} (0.5 mol%) is depicted in Fig. 35.

Table 4: Refined lattice parameters and interatomic distances in $LiSrH_3:Eu^{2+}$ and $LiSrD_3:Eu^{2+}$ (in pm), space group $Pm\bar{3}m$, X-ray data were collected on the *X'Pert Pro* diffractometer. Estimated standard deviations provided by the program TOPAS are given in brackets.

$LiSrH_3:Eu^{2+}$ (0.5 mol%) a = 383.498(3), ($LiSrH_3$, a = 383.572(4))	
Eu/Sr-H	271.174(2)
Li-H	191.749(2)
$LiSrD_3:Eu^{2+}$ (0.5 mol%) a = 382.535(3)	
Eu/Sr-D	270.493(2)
Li-D	191.267(2)

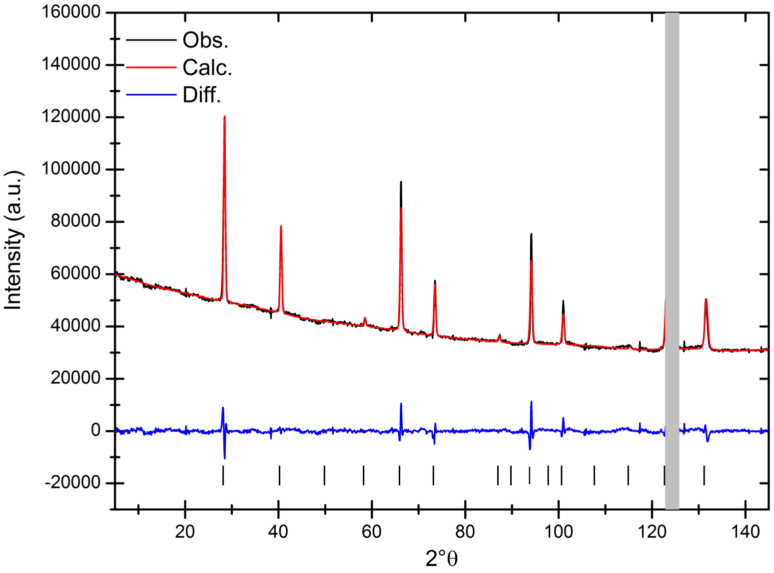

Figure 35: Rietveld analysis of the neutron powder diffraction data of $LiSrH_3$.

4.2.2 Luminescence spectra $LiSrH_3:Eu^{2+}$ and $LiSrD_3:Eu^{2+}$ (0.5 mol%)

At room temperature spectra exhibit broad excitation and emission bands which are assigned to parity-allowed electric dipole transitions between the $4f^7$ and $4f^65d$ levels of Eu^{2+} (emission maximum about 578 nm). In Figs. 36 and 37 the temperature dependent luminescence emission spectra are shown at an excitation wavelength of 360 nm. In the range of 360 - 450 nm, the emission maximum does not exhibit any dependence of the excitation wavelength (see

Appendix, Fig. 122).

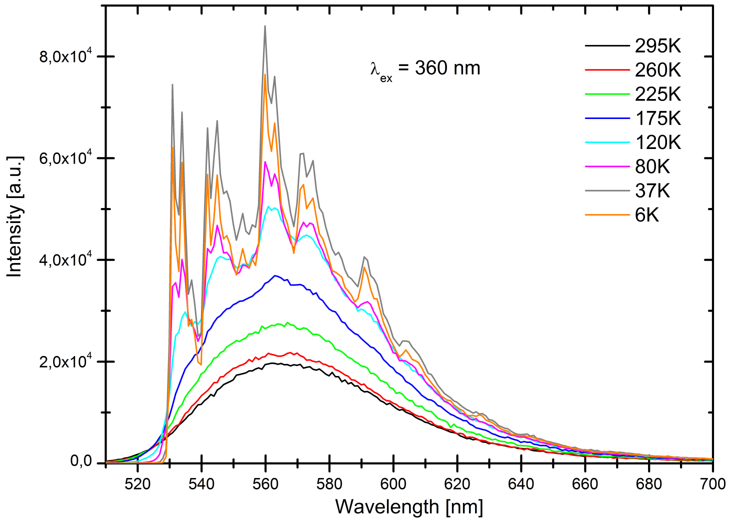

Figure 36: Temperature-dependent luminescence spectra (FL920) of $LiSrH_3:Eu^{+2}$ (0.5 mol%); excitation at 360 nm.

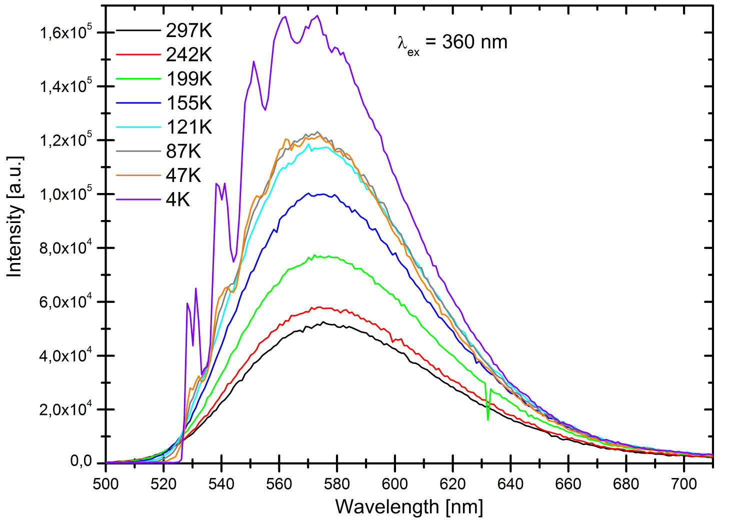

Figure 37: Temperature-dependent luminescence spectra (FL920) of $LiSrD_3:Eu^{2+}$ (0.5 mol%); excitation at 360 nm.

Below 80K, the spectra of $LiSrH_3:Eu^{2+}$ (50K in case of $LiSrD_3:Eu^{2+}$) start showing a vibrational fine structure, which is more pronounced for the hydride and the lines show a better resolution for the hydride than for the deuteride. Emission intensities increase below 120K and are generally about three times higher for the deuteride compared to the hydride. However, a qualitative comparison of the intensities is hampered by slight differences of the ampoules and their alignment. The temperature dependence of the intensities is shown in Fig.38.

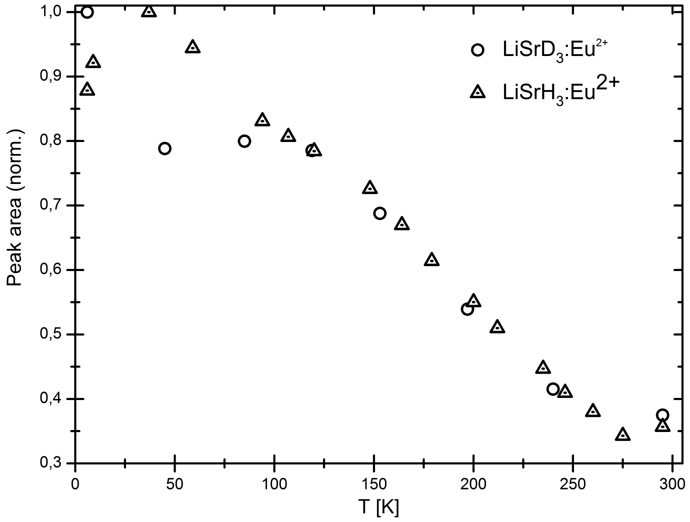

Figure 38: Temperature dependence of the emission intensities of $LiSrH_3:Eu^{2+}$ and $LiSrD_3:Eu^{2+}$(0.5 mol%); excitation at 360 nm.

Details of the emission and excitation spectra at 4 K are depicted for $LiSrH_3:Eu^{2+}$ (Fig. 39 and 41) and $LiSrD_3:Eu^{2+}$ (Fig. 40 and 42).

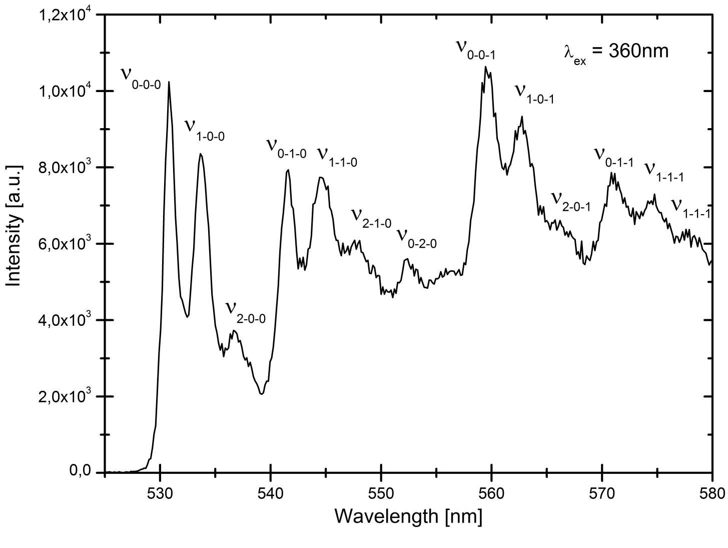

Figure 39: Higher resolution emission spectrum (FL920) of $LiSrH_3:Eu^{2+}$ (0.5 mol%) at 4K; excitation at 360 nm.

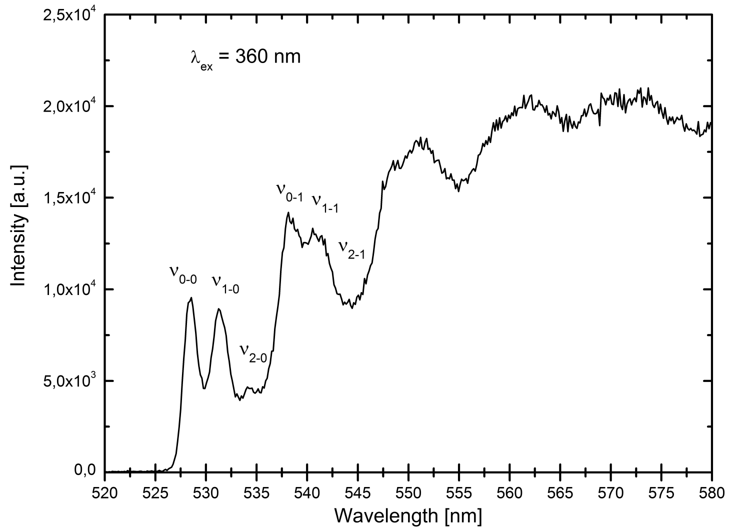

Figure 40: Higher resolution emission spectrum (FL920) of $LiSrD_3:Eu^{2+}$ (0.5 %) at 4K; excitation at 360 nm.

The existence of a vibrational fine structure as it is observed for $LiSrH_3:Eu^{2+}$ or $LiSrD_3:Eu^{2+}$ is typical for intermediate coupling strength of electronic transitions with vibrations. The zero phonon lines (0-0-0) for $LiSrH_3:Eu^{+2}$ or (0-0) for $LiSrD_3:Eu^{+2}$ and the vibronic replica (ν_{x-y-z}) or (ν_{x-y}) are indicated in the spectra and listed in Table 5. In $LiSrH_3:Eu^{2+}$ the vibronic fine structure involves a coupling with at least three different vibrations. A coupling of ~100 cm^{-1} (indicated as x in ν_{x-y-z}) produces a typical pattern of three closely spaced lines which is repeated at ~370 cm^{-1} intervals (indicated as y in ν_{x-y-z}). Furthermore, a coupling to a third vibrational mode of ~970 cm^{-1} (indicated as z in ν_{x-y-z}) is observed. In addition to these vibrational modes, vibronic overtones due to a coupling with those three vibrational modes can be observed, resulting in a group of three lines at ~100 cm^{-1}. The existence of a strong 0-x line and weaker 1-x and 2-x lines indicates a Huang-Rhys coupling parameter S $\approx$ 0.8. For the vibronic lines of the 370 cm^{-1} vibration (y; 0-0-0, 0-1-0) as well as the 970 cm^{-1} (z; 0-0-0, 0-0-1) vibration S is estimated to be 0.7. However, note that an exact determination of S for the higher energy modes is hampered by the increased background. It should be pointed out that the observation of such well-resolved vibrational fine structures allowing the identification of multiple modes is extremely rare for d-f emission. The highest number of couplings observed until now has been the coupling with two vibrations in the emission spectra of Ce^{+3}, Pr^{3+} and

Tb^{3+}[85,138,139] in elpasolites. A coupling with three vibrations or more in df emission has never been observed before.

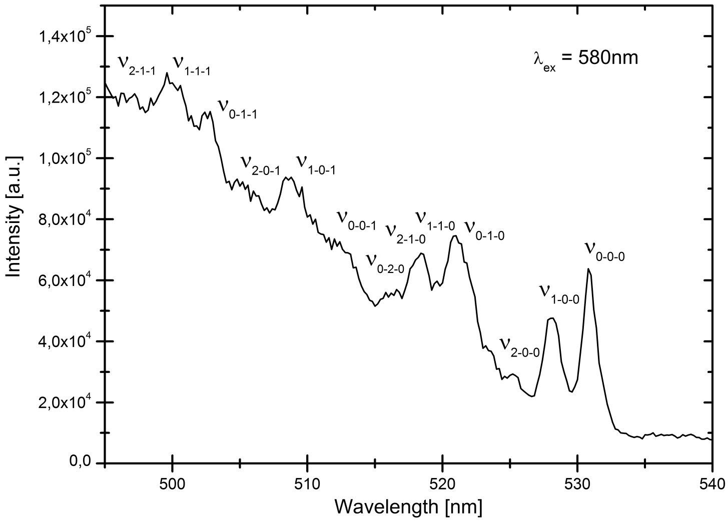

Figure 41: Higher resolution excitation spectrum (FL920) of $LiSrH_3:Eu^{2+}$ (0.5 mol%) at 4K; emission at 580 nm.

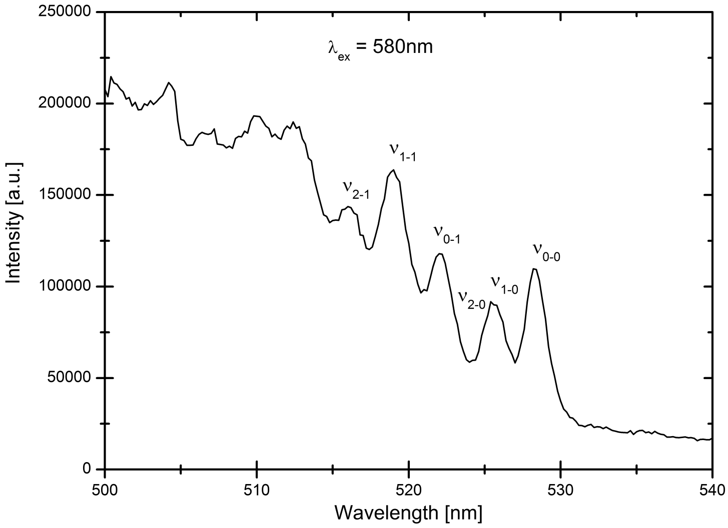

Figure 42: Higher resolution spectrum (FL920) of $LiSrD_3:Eu^{2+}$ (0.5 mol%) at 4K; emission at 580 nm.

Clear vibronic fine structures are also visible in the excitation spectra. However, only the low energy vibrations can be clearly distinguished. As the $4f^65d$ excited state is split into multiple electronic states (7 FJ levels, $4f^6[^7F_0]5d^1$)[140] whose splitting is of the same order as the vibrational energies, the assignment of the higher energy vibrations is hampered. For $LiSrH_3:Eu^{2+}$ the couplings indicated as x and y in ν_{x-y-z} with Huang-Rhys parameters of 0.8 and 0.7 are observed at 93 and 362 cm^{-1} in the excitation spectrum. Interestingly, the vibrational energies in the emission spectrum which represent the ground state vibrations, 99 and 374 cm^{-1}, are slightly higher than those in the excitation spectra. This observation reveals a higher force constant and stronger bonding of the ground state compared to the excited state $4f^65d(eg)$ and is in good agreement with recent experimental and theoretical studies on cerium[85,141]. In case the $5d(e_g)$ is the lowest excited state, a weakening of the bonding is expected; for the $5d(t_{2g})$ being the lowest excited state the opposite is the case. $LiSrD_3:Eu^{2+}$ also shows a vibronic fine structure at low temperatures, however, only two vibrational modes can be clearly distinguished. For the 96 cm^{-1} mode a Huang-Rhys parameter of 0.9 can be estimated, whereas it is not possible to determine S for the 338 cm^{-1} mode. The position of the vibrational modes in the excitation spectrum (86 cm^{-1} for the low energy vibration) also indicates a weaker bonding in the $4f^65d(e_g)$ excited state. A comparison of hydride and deuteride shows that the there is only a slight change in the crystal field splitting which can be explained with the small difference in lattice constants. Surprisingly, no significant change in the vibrational energies is observed (energies for the hydride are about 5-10% larger). However, this finding is in good agreement with previous theoretical and experimental research showing that low energy acoustic phonons (50-300cm^{-1}) -in contrast to higher energy optical phonons- do not show the expected $\sqrt{2}$ -dependence and are very similar for metal hydrides and deuterides[142,143].

Table 5: Vibronics in the excitation and emission spectrum at 4K for the $4f^6 5d$ - $^8S_{7/2}$ transition of Eu^{2+} in $LiSrH_3:Eu^{2+}$ 0.5% and $LiSrD_3:Eu^{2+}$ 0.5 mol% (see Fig. 39, 41, 40 and 42); ΔE gives the energy of the vibrational modes with respect to their zero-phonon lines.

Emission			
	$LiSrH_3:Eu^{2+}$		$LiSrD_3:Eu^{2+}$
Line	ΔE [cm^{-1}]	Line	ΔE [cm^{-1}]
v_{1-0-0}	99	v_{1-0}	96
v_{2-0-0}	204	v_{2-0}	198
v_{0-1-0}	374	v_{0-1}	338
v_{1-1-0}	476	v_{1-1}	420
v_{2-1-0}	591	v_{2-1}	542
v_{0-2-0}	730		
v_{0-0-1}	964		
v_{1-0-1}	1068		
v_{2-0-1}	1195		
v_{0-1-1}	1324		
v_{1-1-1}	1424		
v_{2-1-1}	1532		
Excitation			
	$LiSrH_3:Eu^{2+}$		$LiSrD_3:Eu^{2+}$
v_{1-0-0}	93	v_{1-0}	86
v_{2-0-0}	194	v_{2-0}	123
v_{0-1-0}	362	v_{0-1}	225
v_{1-1-0}	451	v_{1-1}	336
v_{2-1-0}	495	v_{2-1}	440
v_{0-2-0}	548		
v_{0-0-1}	692		
v_{1-0-1}	784		
v_{2-0-1}	908		
v_{0-1-1}	1057		
v_{1-1-1}	1161		
v_{2-1-1}	1322		

From the position of the zero-phonon line (~530 nm) and the onset of the $4f^6 5d(T_{2g})$ excitation band (~375 nm) in the excitation spectra (see Fig. 43, 44) crystal field splittings for the cuboctahedral field between the $4f^6 5d(e_g)$ and $4f^6 5d(T_{2g})$ are estimated to be approx. 7800 cm^{-1} for the hydride and 7660 cm^{-1} for the deuteride. However, the position of the onset of the $4f^6 5d(T_{2g})$ excitation band exhibit a rather large uncertainty, making a very accurate determination impossible.

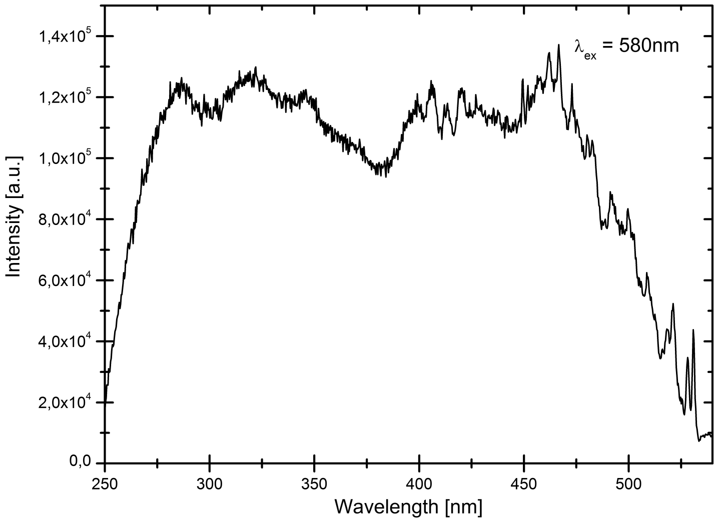

Figure 43: Excitation spectrum (FL920) of $LiSrH_3:Eu^{2+}$ (0.5 %) at 4K; emission at 580 nm.

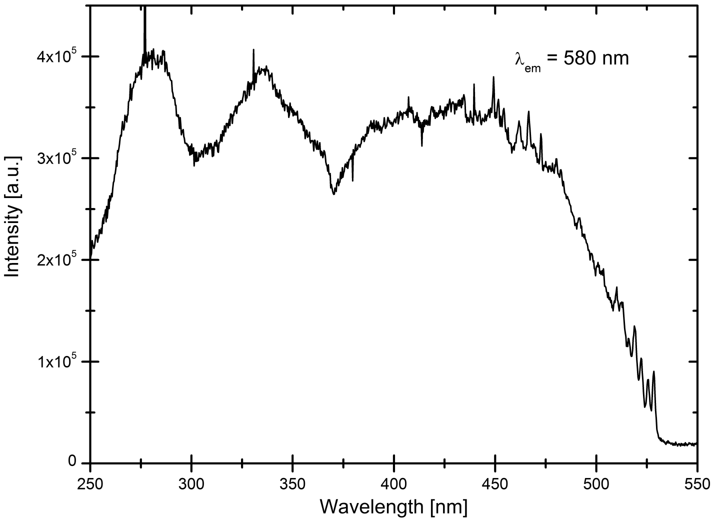

Figure 44: Excitation spectrum (FL920) of $LiSrD_3:Eu^{2+}$ (0.5 %) at 4K; emission at 580 nm.

Luminescence decay curves were analyzed using a single exponential function, ignoring the fact that the curves in the higher temperature region for the partly quenched luminescence deviate sligtly from single exponential behavior. Lifetimes at low temperature are about 420 ns for the hydride and 450 ns for the deuteride. This is slightly shorter than expected compared to lifetimes of 1 -1.4 μs for Eu(II) emission around 560 nm (parity-allowed transitions between the $^8S_{7/2}$ ($4f^7$) ground state and the $4f^65d$ excited state) given in[144]. As the refractive index has a strong influence on the radiative decay rate, the higher refractive index of hydrides[145] compared to those oxidic materials listed in[144] causes the shorter decay times. The quenching temperatures are 165K and 175K, respectively (see Fig. 45). As the electron-phonon coupling in $LiSrH_3$ and $LiSrD_3$ is rather weak (S = 0.7-0.8), temperature quenching due to a thermally activated cross-over from the excited state to the ground state is unlikely. A more appropriate model is the thermally activated photoionization, that implies the location of the $4f^65d$ excited state just below the conduction band[103,146,147]. The emission is then quenched by thermally activated ionization from the $4f^65d$ state to the conduction band. Using Equation 13, the energy barrier for thermal quenching is estimated to be 0.24 eV for the hydride and 0.26 eV for the deuteride.

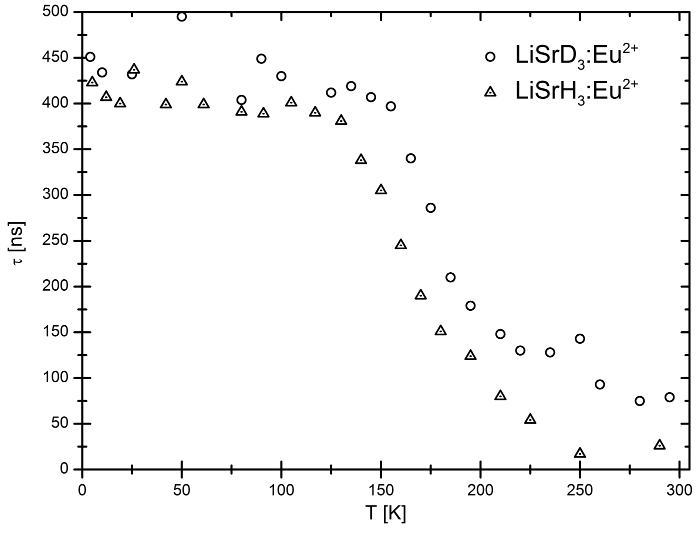

Figure 45: Temperature dependence of τ of $LiSrH_3:Eu^{2+}$ (0.5 mol%) and $LiSrD_3:Eu^{2+}$(emission at 580 nm, FL9-20). Quenching temperatures 165K and 175K, respectively.

4.2.3 $LiBaH_3$:Eu^{2+} and $LiBaD_3$:Eu^{2+}

The hydrides $LiEu_xBa_{1-x}H_3$ were prepared similarly to the strontium compound. $LiBaH_3$ was obtained as a white powder whereas $LiBaH_3$:Eu^{2+} and $LiBaD_3$:Eu^{2+} (0.5 mol%) were obtained as a straw yellow powders showing an intense lime-green emission[137]. The europium-free sample did not exhibit any luminescence. In some samples small amounts of BaH_2 were present.

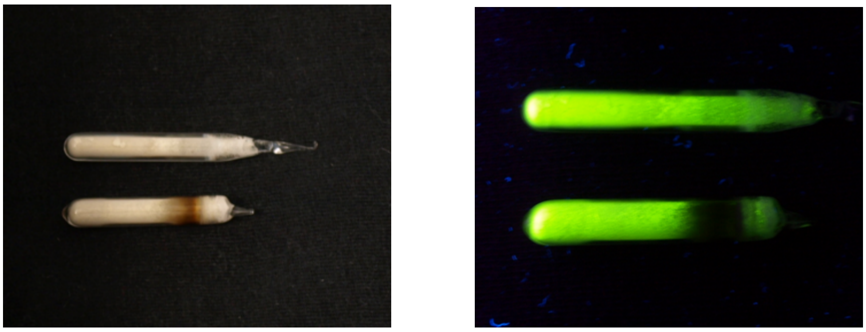

(a) At daylight.

(b) Under UV-excitation.

Figure 46: From top to bottom: $LiBaD_3$:Eu^{2+}, $LiBaH_3$:Eu^{2+} at daylight (a) and under UV excitation (365 nm) (b).

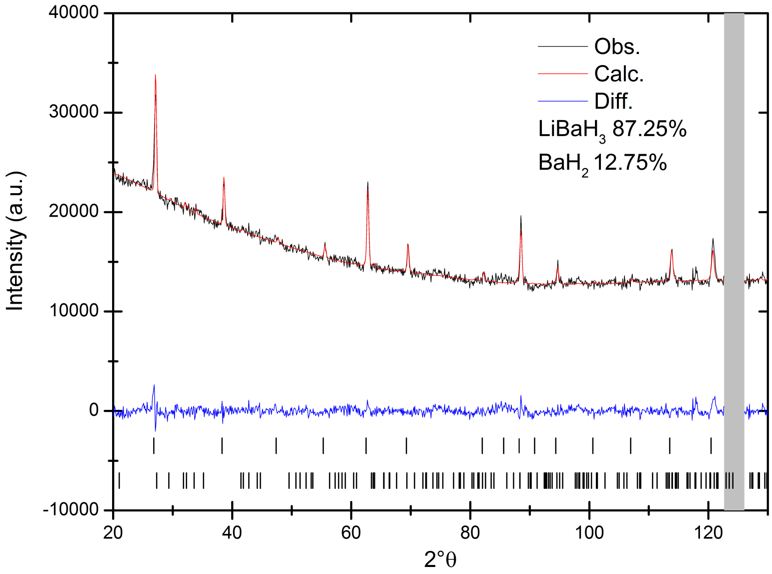

Figure 47: Rietveld analysis of the neutron powder diffraction data of $LiBaH_3$.

Neutron powder diffraction experiments show that, like the above mentioned strontium homologue, $LiBaH_3$ and $LiBaD_3$ crystallize in the cubic inverse perovskite structure type, thus confirming earlier results obtained from neutron diffraction experiments[37]. Assuming a stastistic occupation of the barium site 1*b* by barium and europium, the distances given in Table 6 were obtained. Slightly smaller differences were obtained for the deuteride.

Table 6: Refined lattice parameters and interatomic distances in $LiBaH_3:Eu^{2+}$ and $LiBaD_3:Eu^{2+}$ (in pm), space group $Pm\bar{3}m$, X-ray data were collected on the *X'Pert Pro* diffractometer. Estimated standard deviations provided by the program TOPAS are given in brackets.

$LiBaH_3:Eu^{2+}$ (0.5 mol%) a = 402.284(3), ($LiBaH_3$, a = 402.395(1))	
Eu/Ba-H	284.458(2)
Li-H	201.142(2)
$LiBaD_3:Eu^{2+}$ (0.5 mol%) a = 401.459(3)	
Eu/Ba-D	283.750(2)
Li-D	200.730(2)

Since the temperature dependent intensities showed an rather unusual behavior (see the following section 4.2.4), XRDs of $LiBaH_3:Eu^{2+}$ (0.5 mol%) were also recorded at temperatures between 20 and 100 K in order to check for the occurrence of a phase transition.

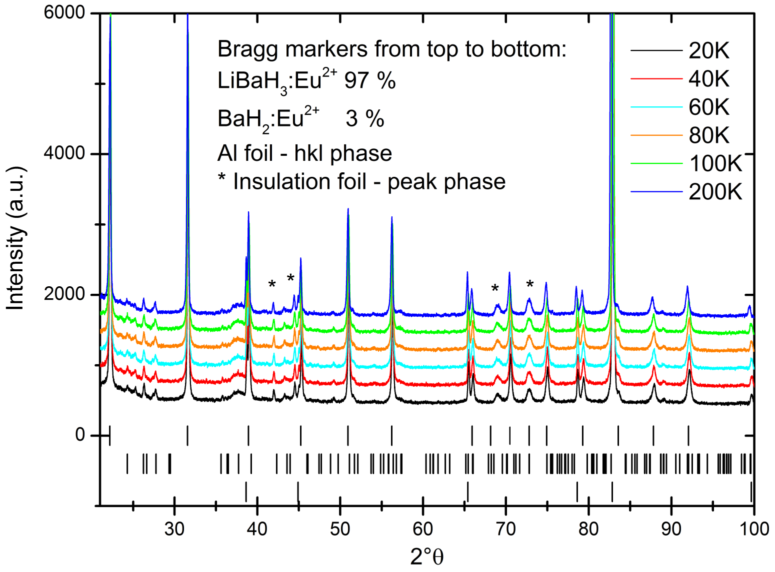

Figure 48: Temperature dependent X-ray data of $LiBaH_3:Eu^{2+}$ (0.5 mol%) enclosed in apiezon grease and aluminum foil measured on a Guinier camera.

However, no significant change could be observed between 20 and 200K and therefore a phase transition in this temperature range is excluded. Lattice constants are tabulated in Table 7 and the coefficient for linear thermal expansion of the lattice parameter a between 20 and 100 K was determined via a linear regression to be $6.2(9)\cdot10^{-6}$ K^{-1}. The temperature dependence between 20 to 200 K can be described via polynomials of second order, $a(T) = a_0 + a_1\cdot T + a_2\cdot T^2$ with $a_0 = 400.51(1)$, $a_1 = 0.0012(4)$ and $a_2 = 1.2(1)\cdot10^{-5}$.

Table 7: Temperature dependence of the lattice constant and ε_0 of $LiBaH_3:Eu^{2+}$ (0.5 mol%).

T [K]	a [pm]	ε_0
20	400.549(5)	0.081(1)
40	400.564(5)	0.079(1)
60	400.638(5)	0.078(2)
80	400.675(5)	0.075(1)
100	400.753(6)	0.073(2)
200	401.216(5)	0.074(1)

4.2.4 Luminescence spectra of $LiBaH_3:Eu^{2+}$ and $LiBaD_3:Eu^{2+}$ (0.5 mol%)

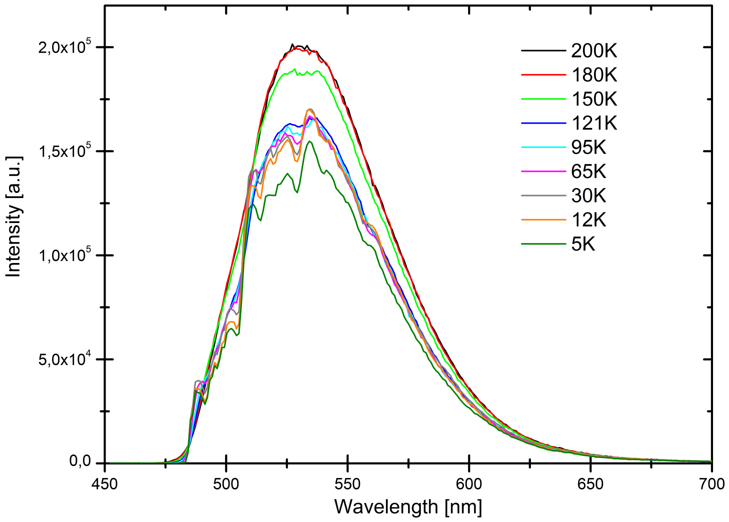

Figure 49: Temperature-dependent luminescence spectra (FL920) of $LiBaH_3:Eu^{2+}$ (0.5 mol%); excitation at 360 nm.

In Fig.49 and 50 temperature-dependent luminescence emission spectra for Eu^{2+}in $LiBaH_3$ and $LiBaD_3$ are shown. At room temperature a broad band in the green spectral region (maximum around 530 nm) is observed. In contrast to the Eu^{2+} emission in $LiBaF_3$ [45], no $^8S_{7/2} \rightarrow {}^6P_{7/2}$ transition is observed in $LiBaH_3$, but only the parity-allowed electric dipole transition $^8S_{7/2} \rightarrow 4f^65d$ is visible.

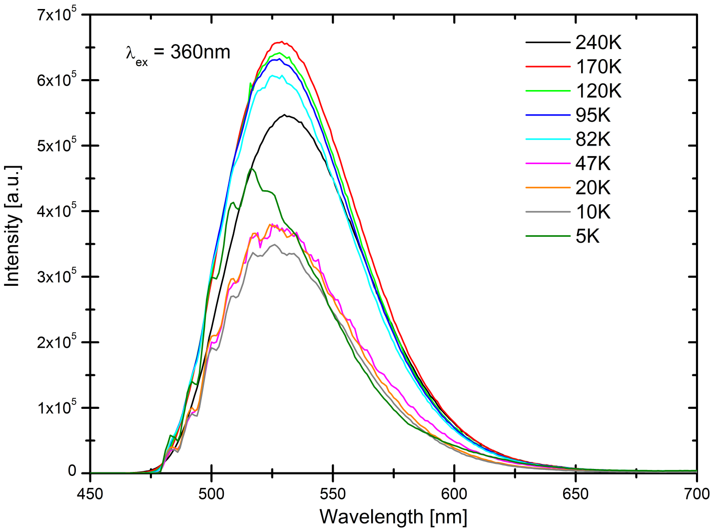

Figure 50: Temperature-dependent luminescence spectra (FL920) of $LiBaD_3$:Eu^{2+} (0.5 mol%); excitation at 360 nm.

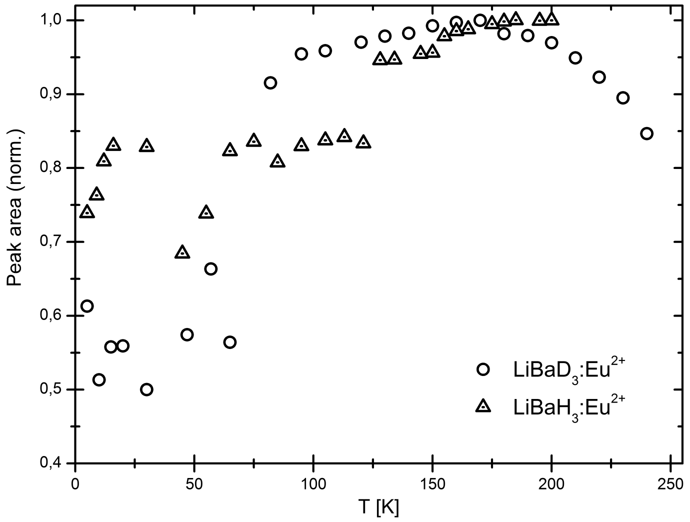

Figure 51: Temperature dependence of the emission intensities of $LiBaH_3$:Eu^{2+} and $LiBaD_3$:Eu^{2+} (0.5 mol%); excitation at 360 nm.

With decreasing temperature, intensities first increase slightly, but then below approx. 130 K they show a significant decrease. Below 65 K, the spectra of $LiBaH_3:Eu^{2+}$ (50 K in case of $LiBaD_3:Eu^{2+}$) show a vibrational fine structure (see Fig. 49, 50), whose resolution is, however, not as good as for the strontium homologues. As observed for the strontium isotype, emission intensities of the deuteride are about three times higher than of the hydride. The temperature dependence of the emission intensities is shown in Fig.51.

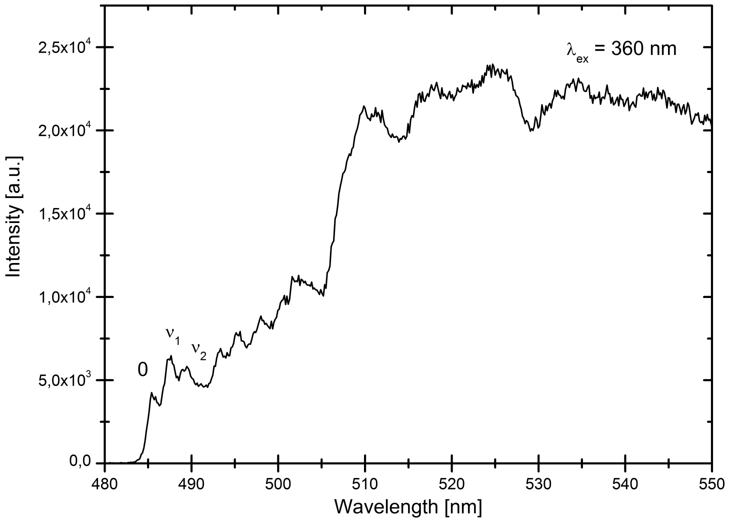

Figure 52: Details in the emission spectrum (FL920) of $LiBaH_3:Eu^{2+}$ (0.5 mol%) at 4K; excitation at 360 nm.

Details of the emission and excitation spectra at 4 K are depicted for $LiBaH_3:Eu^{2+}$ (Fig. 52 and 54) and $LiBaD_3:Eu^{2+}$ (Fig. 53 and 55).

In the range from about 420 to 500 nm a vibrational fine structure is also visible in the excitation spectra. However, due to the lower resolution and the lamp spectrum as well as signals originating from the split $4f^6 5d$ excited state interfering with the vibrational fine structure in the excitation spectra, the assignment of vibrational modes was limited to only few lines (Table 8). Higher vibrational energies are found in the emission spectra, indicating a stronger bonding of Eu^{2+} in the ground state. In the hydride, ν_1 is about 90 cm^{-1} in the emission and only 77 cm^{-1} in the excitation spectrum. The same observation is made for the deuteride, where ν_1 is about 100 cm^{-1} in the emission and only 86 cm^{-1} in the excitation spectrum.

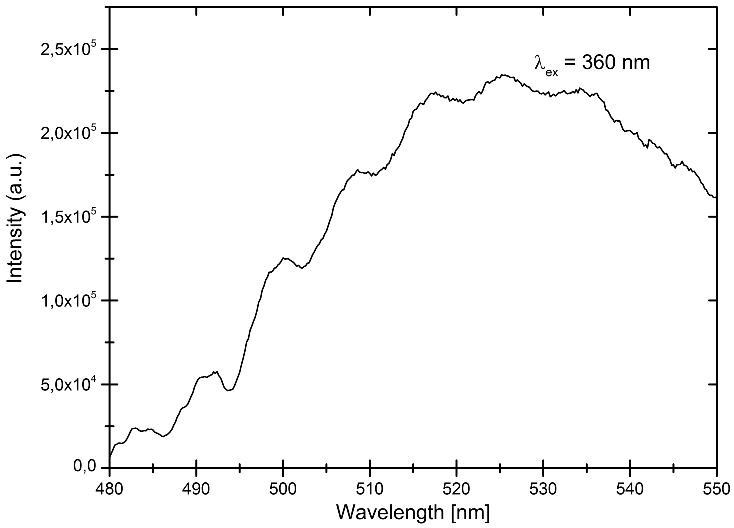

Figure 53: Details in the emission spectrum (FL920) of $LiBaD_3$:Eu^{2+} (0.5 mol%) at 4K; excitation at 360 nm.

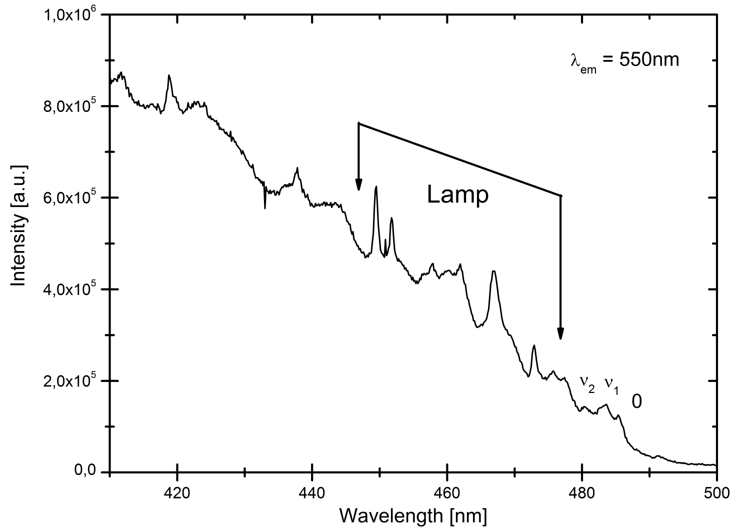

Figure 54: Details in the excitation spectrum (FL920) of $LiBaH_3$:Eu^{2+} (0.5 mol%) at 4K; emission at 550 nm.

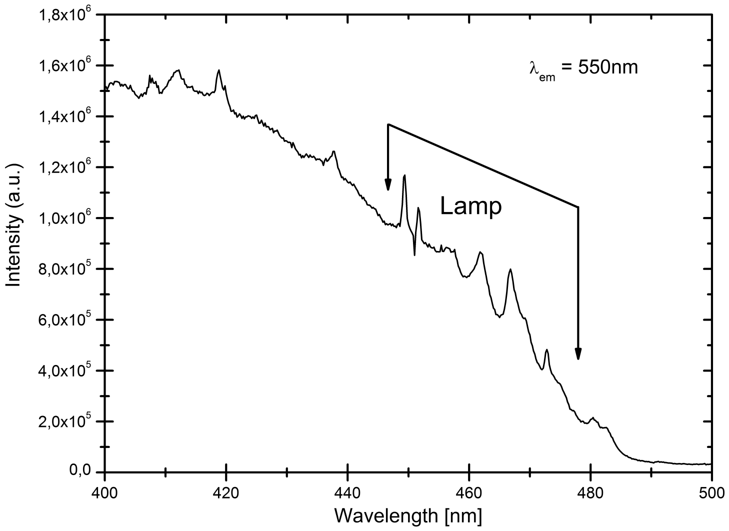

Figure 55: Details in the excitation spectrum (FL920) of $LiBaD_3$:Eu^{2+} (0.5 mol%) at 4K; emission at 550 nm.

Table 8: Vibronics in the excitation and emission spectrum at 4K for the $4f^65d$ - $^8S_{7/2}$ transition of Eu^{2+} in Eu^{2+} in $LiBaH_3$:Eu^{2+} (0.5 mol%) (see Fig. 52, 54, 53 and 55); ΔE gives the energy of the vibrational modes with respect to their zero-phonon lines.

Emission			Excitation		
	$LiBaH_3$:Eu^{2+}	$LiBaD_3$:Eu^{2+}		$LiBaH_3$:Eu^{2+}	$LiBaD_3$:Eu^{2+}
Line	ΔE [cm^{-1}]	ΔE [cm^{-1}]	Line	ΔE [cm^{-1}]	ΔE [cm^{-1}]
ν_1	89	103	ν_1	77	86
ν_2	164	188	ν_1	128	178

From the position of the zero-phonon line (~485 and 483 nm) and the onset of the $4f^65d(T_{2g})$ excitation band (~355 nm) in the excitation spectra (see Fig. 56, 57) crystal field splittings for the cuboctahedral field between the $4f^65d(e_g)$ and $4f^65d(T_{2g})$ are estimated to be approx. 7550 cm^{-1} for the hydride and 7470 cm^{-1} for the deuteride. However, as already mentioned before, the position of the onset of the $4f^65d(T_{2g})$ excitation band exhibit a rather large uncertainty.

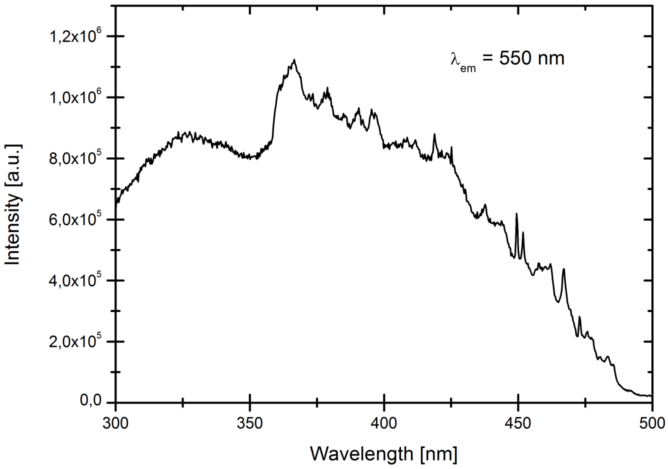

Figure 56: Excitation spectrum (FL920) of $LiBaH_3$:Eu^{+2} (0.5 mol%) at 4K; emission at 550 nm.

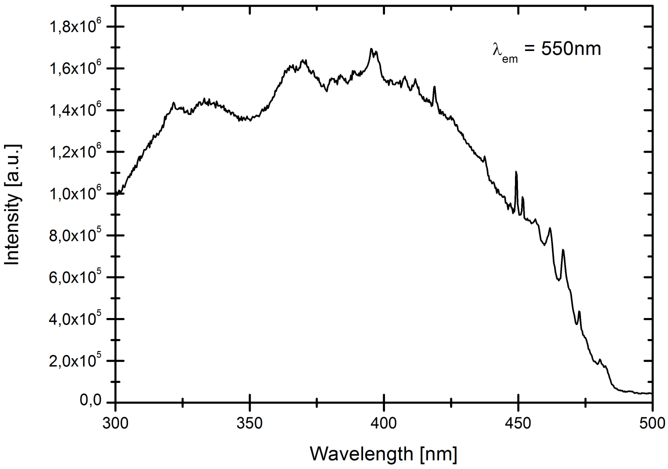

Figure 57: Excitation spectrum (FL920) of $LiBaD_3$:Eu^{+2} (0.5 mol%) at 4K; emission at 550 nm.

Lifetimes at low temperature are about 295 ns for the hydride and 280 ns for the deuteride. Decay curves of the hydride measured for an emission at 490 nm give a lifetime of about 270 ns, indicating the presence of two slightly different luminescence centers. As the emission wavelength is shorter than in the strontium compound (M = Ba 530 nm, M = Sr 570 nm)), the luminescence lifetimes are also shorter. Based on the λ^3-dependence of the luminescence lifetime a 1.25 shorter lifetime is expected. Due to luminescence quenching the lifetimes decrease at temperatures above 200 K (see Fig. 58). As in the case of $LiSrH_3$, thermally activated photoionization is proposed as quenching mechanism.

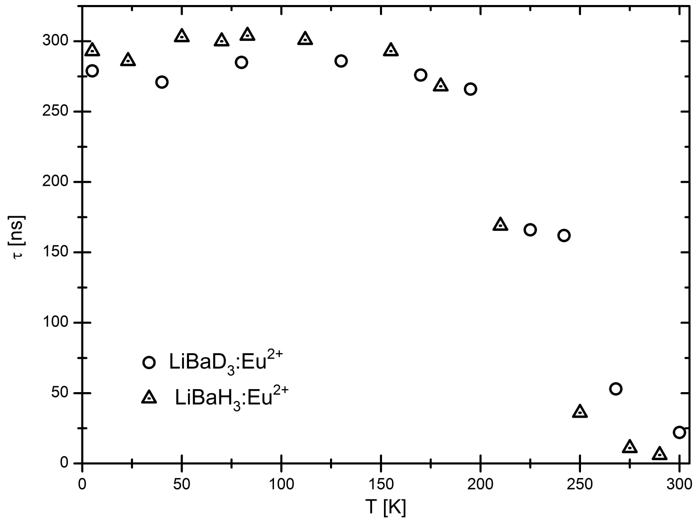

Figure 58: Temperature dependence of τ of $LiBaH_3$:Eu^{2+} (0.5 mol%) and $LiBaD_3$:Eu^{2+}(Emission at 550 nm, FL9-20). Quenching temperatures 210K and 230K, respectively.

Since no phase transition was observed for the hydride in the temperature-dependent XRD measurements (see Fig.48) despite of the occurrence of an unusual temperature dependence of the emission intensities (see Fig.49) and the lifetime measurements with different excitation wavelengths suggest the presence of two slightly different luminescence centers, it is thinkable that Eu(II) is not always located at the center of the cuboctahedron. As the crystal radius of Ba(II) is larger than the crystal radius of Eu(II)[27], local distortions of the cuboctahedra might be induced by Eu(II)-doping. At higher temperatures more Eu(II) ions might be located exactly at the center and result in higher emission intensities. Subsequently, a larger displacement at lower temperatures might result in lower emission intensities and be a possible explanation the unusual temperature dependence. An alternative explanation could be a change in the absorption strength at the excitation wavelength at low temperatures as proposed before in case of an oxonitridosilicate phosphor[148]. This explanation is also in agreement with the observation that no unusual temperature dependent behavior of the lifetimes occurs. A further possible, yet improbable reason might be an inappropriate alignment of the samples.

4.2.5 $LiSr_{1-y}Ba_yH_3:Eu^{2+}$ (0.5 mol%)

The samples $LiSr_{1-y}Ba_yH_3:Eu^{2+}$ (0.5 mol%) were obtained through hydrogenation of the corresponding alloys at about 300°C and approx.100 bar for about 4-5 days as powders in different shades of yellow. They showed bright luminescence emission with luminescence colors varying from light green for y = 1.0 over different shades of greenish yellow to bright yellow for y = 0.0.

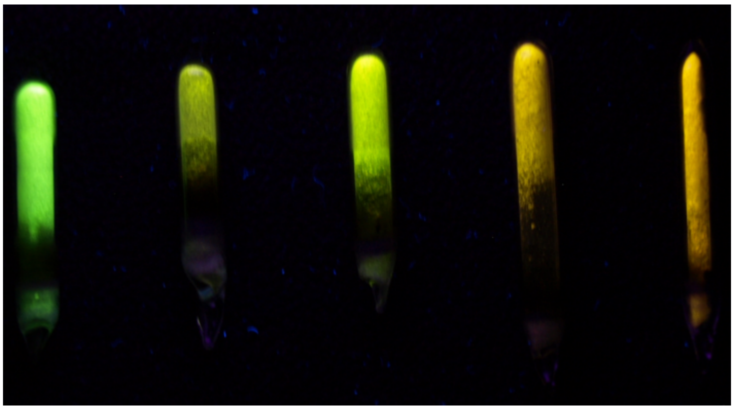

Figure 59: $LiSr_{1-y}Ba_yH_3:Eu^{2+}$ (0.5 mol%) under UV-light (365 nm). From left to right y = 1.0, 0.642, 0.492, 0.351, 0.0.

In some cases, a mixture of phases was obtained. Nominal compositions are listed in Table 9; y is the barium content whereas the strontium content is 1.0-y-0.005. X-ray powder diffraction data were collected on the *X'Pert Pro* diffractometer and Rietveld refinement was carried out using the program TOPAS. Estimated standard deviations are given in brackets. Additionally to the cubic perovskite phases, small amounts of binary hydrides were sometimes present. In order to clarify if the occurrence of phase mixtures is caused by a miscibility gap or rather a non-equilibrium state of the samples which might be due to the low reaction temperatures that could be applied using the autoclave, ε_0 is given as a measure of strain in Table 9. The Rietveld refinement of the compound with y = 0.193 is exemplary depicted in Fig. 60. For the end members, ε_0 is rather small, whereas it is significantly larger for all other members of the mixed crystals. The occurrence of a considerable strain might due to local changes of the d-values caused by substitution or to a non-equilibrium state of the system. In order to clarify if the system exhibits miscibility gap, the preparation method needs to be optimized. In particular, it would be necessary to carry out reactions at higher temperatures and high hydrogen pressures.

Table 9: Nominal composition in $LiSr_{1-y}Ba_yH_3:Eu^{2+}$ (0.5 mol%), number of cubic perovskite phases found, refined lattice parameters (determined by XRD, recorded at the *X'Pert Pro*), maximum emission wavelengths and FWHM (determined from spectra measured at the Fluoromax-4).

y	nr. of phases	a [pm]/ε_0	λ_{em} [nm] (FWHM [nm])
0.0 (11/11/2011 Nr1)	1	383.498(3)/0.049(7)	580 (98)
0.193	1	387.536(4)/0.169(3)	581 (105)
0.298	1	389.81(2)/0.250(5)	579 (105)
0.351	1	391.21(1)/0.23(1)	582 (108)
0.492	3	401.02(1)/0.15(2); 396.98(1)/0.57(2);) 385.15(1)/0.17(5)	560 (107)
0.642	3	401.62(1)/0.121(9); 398.5(1)/0.37(3); 386.68(4)/0.09(1)	565 (113)
0.89	1	401.250(3)/0.107(2)	533 (88)
1.0 (22/11/2011)	1	402.284(3)/0.035(1)	524 (87)

Spectra were recorded at the FluoroMax-4 and partly at the FLS920 spectrofluorometer. It should be mentioned that on the strontium-rich side of the system excitation wavelengths from 320 - 420 nm result in similarly high emission intensities. Using an excitation of 465 nm (corresponding to a blue LED) only leads to a decrease of the emission intensity of a few percent compared to an excitation with higher energy. In the following, normalized excitation and emission spectra of $LiSr_{1-y}Ba_yH_3:Eu^{2+}$ (0.5 mol%) measured at the FL920 (Fig.61) and the correlation between the initial weight, lattice parameters and emission maxima determined from emission spectra measured at the FluoroMax-4 (Fig.62) are depicted. For spectra measured at the FluoroMax-4 see Appendix (Fig.123). Emission spectra of impure samples are not depicted in Fig. 61, but emission maxima of those are included in Fig. 62.

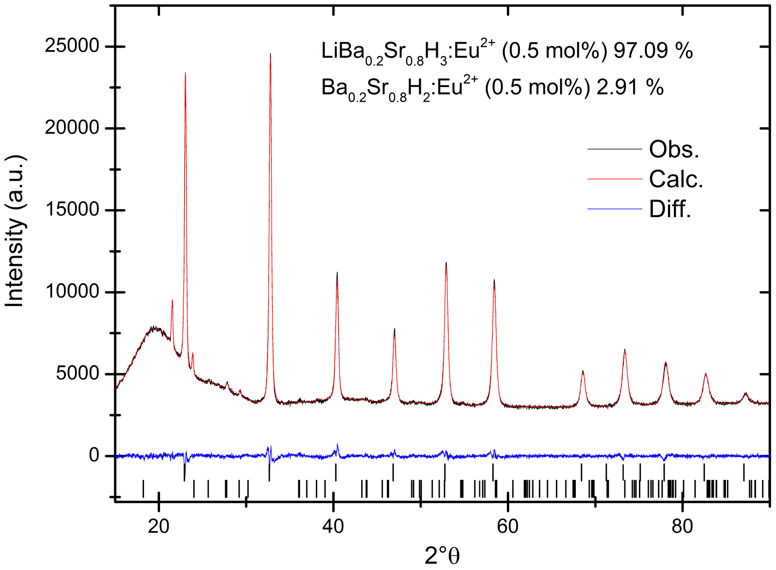

Figure 60: Rietveld refinement of the crystal structure of $LiSr_{0.807}Ba_{0.193}H_3$:$Eu^{2+}$ (0.5 mol%).

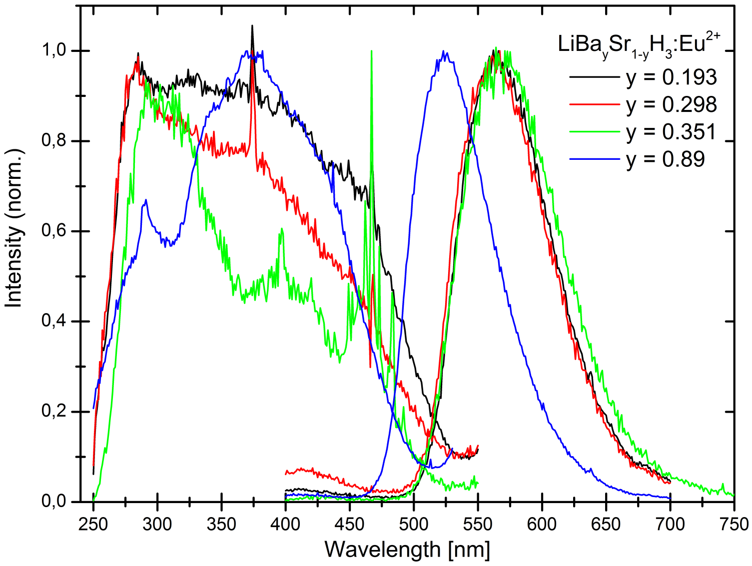

Figure 61: Luminescence spectra (FL920) of $LiSr_{1-y}Ba_yH_3$:Eu^{+2} (0.5 mol%) at 293 K (y corresponds to the initial weight).

In order to estimate the composition of the different phases in the phase mixtures, a behavior of the lattice constant of the system $LiSr_{1-x}Ba_xH_3$:Eu^{2+} (0.5 mol%) according to Vegard's law was assumed. (The straight line between the pure compounds $LiSr_{1-x}Ba_xH_3$:Eu^{2+}, calculated from the arithmetic average of at least two measurements of the pure samples, is a = 383 pm + x 19 pm.) Consequently, in the sample with nominal y = 0.492 three phases with approx. y = 0.95, 0.74 and 0.11 seem to be present. For the nominal y = 0.642, y = 0.98, 0.82 and 0.12 seem to be present. As a result of the existence of more than one phase, spectra of these samples also show a slight broadening of the emission bands (see Appendix Fig.123). Decay times are listed in Table 10.

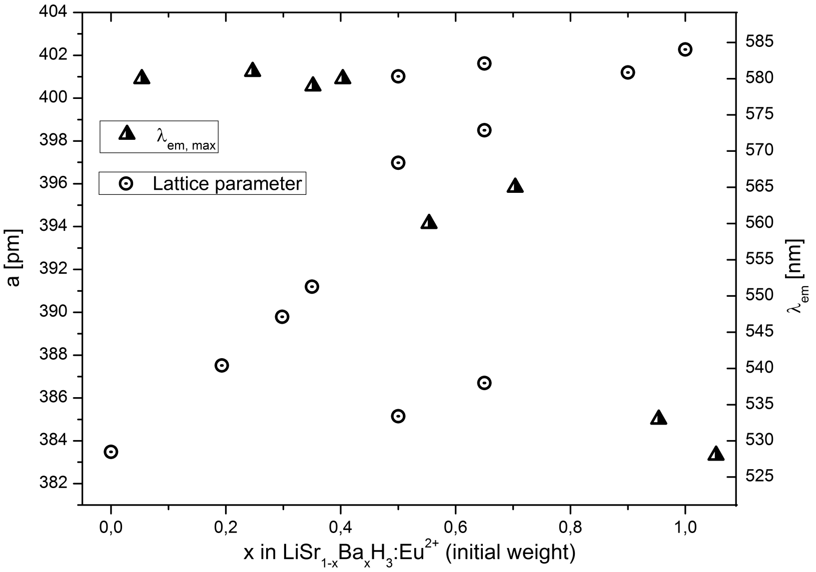

Figure 62: Correlation of lattice parameter a and maximum emission wavelength of $LiSr_{1-y}Ba_yH_3$:Eu^{+2} (0.5 mol%) at 293 K.

Table 10: Decay times of $LiSr_{1-x}Ba_xH_3$:Eu^{2+} measured at RT. Analysis was carried out using a single exponential function. Emission wavelength 550 nm.

x	0.193	0.298	0.89
τ (ns)	3	3	6

4.2.6 $KMgH_3$:Eu^{2+}

KH (50 w% in paraffin, washed several times in hexane and dried in vacuum) was mixed with EuH_2 and fine Mg powder and heated twice to approx. 450°C under 150 bar H_2 pressure for 2 days. Note that significantly longer hydrogenation times lead to a loss in the potassium content. The desired phase was obtained almost exclusively and showed an extremely bright yellow luminescence (see Fig.63). An alternative synthesis route, mixing liquid potassium with MgH_2 or MgH_2 and EuH_2, respectively and heating to approx. 300°C at a hydrogen pressure of 120 bar during 2 weeks did not yield the desired product in a satisfying amount.

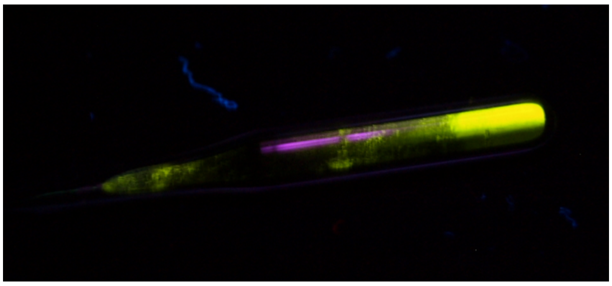

Figure 63: $KMgH_3$:Eu^{2+} (1.0 mol%) under UV-light (365 nm).

Even though no neutron data of $KMgH_3$ were collected, in accordance with single crystal XRD measurements[42] and theoretical calculations (see Fig.114 in Sect.6.3.2) it is presumed to crystallize in the normal cubic perovskite structure type. Europium is expected to be divalent and, taking the significantly smaller crystal radius of Mg^{2+} into account[27], to occupy the high symmetry site ($m\bar{3}$m) of potassium. For a hypothetical statistical occupation of the potassium *1b* site by Eu(II), the interatomic distances listed in Tabl.11 are obtained.

Table 11: Refined lattice parameters and interatomic distances in $KMgH_3$:Eu^{2+} (in pm), space group $Pm\bar{3}m$, X-ray data were collected on the *X'Pert Pro* diffractometer. Estimated standard deviations provided by the program TOPAS are given in brackets.

$KMgH_3$:Eu^{2+} (1 mol%) a = 402.869(4), ($KMgH_3$, a = 402.606(6))	
Eu/K-H	284.685(3)
Mg-H	201.435(2)

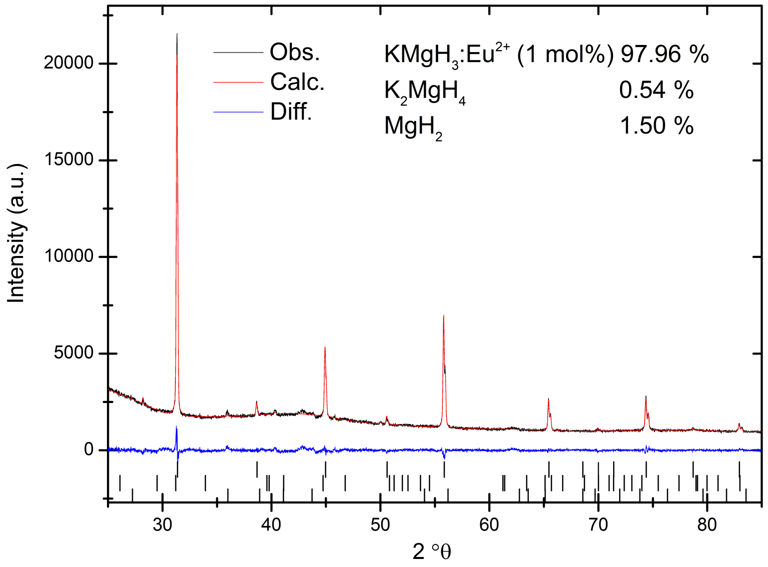

Figure 64: Rietveld refinement of the crystal structure of $KMgH_3:Eu^{2+}$ (approx.1 mol%), normal cubic perovskite.

Additionally, temperature-dependent XRD measurements were carried out (see Fig.65).

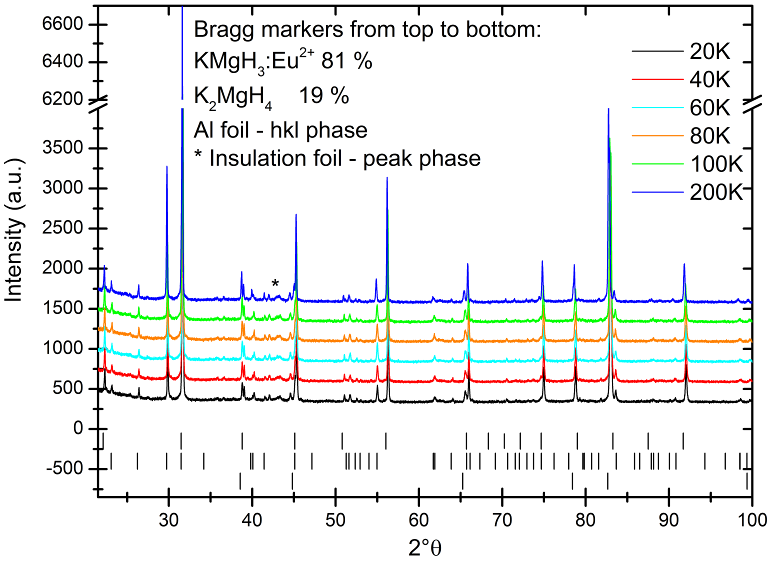

Figure 65: Temperature dependent X-ray data of $KMgH_3$ enclosed in apiezon grease and aluminum foil measured on a Guinier camera.

No significant change could be observed between 20 and 200K and therefore a phase transition in this temperature range is excluded. The tetragonal impurity phase reflections were assigned to K_2MgH_4[149] whose formation was probably caused by an excess of KH. Lattice constants are tabulated in Table 12. The temperature dependence between 20 to 200 K can be described via polynomials of second order, $a(T) = a_0 + a_1 \cdot T + a_2 \cdot T^2$ with $a_0 = 400.90(2)$, $a_1 = 0.0011(5)$ and $a_2 = 1.4(2) \cdot 10^{-5}$. The coefficient for linear thermal expansion of the lattice parameter a between 20 and 100 K was determined via a linear regression to be $7.4(9) \cdot 10^{-6} K^{-1}$.

Table 12: Temperature dependence of the lattice constant and ε_0 of $KMgH_3$.

T [K]	a [pm]	e_0
20	400.95(2)	0.022(3)
40	400.95(2)	0.014(4)
60	401.00(2)	0.013(4)
80	401.07(2)	0.018(4)
100	401.16(1)	0.015(4)
200	401.68(3)	0.0(2)

In Fig.66 temperature-dependent luminescence emission spectra of $KMgH_3:Eu^{2+}$ are shown.

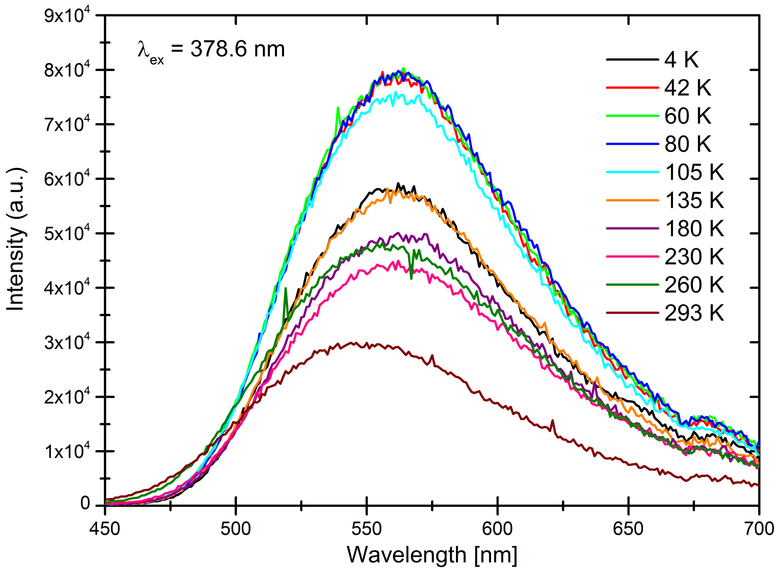

Figure 66: Temperature-dependent emission spectra (FL920) of $KMgH_3:Eu^{2+}$ (approx.1 mol%). Excitation at 376.8 nm.

The emission maximum of the broad df-band is located at approx. 560 nm, but shows a slight temperature dependence (blueshift with decreasing temperature). Luminescence studies were carried out on a sample containing only 0.5 w% K_2MgH_4 so that an Eu(II) emission in K_2MgH_4 can be excluded.

With decreasing temperature intensities increase; below 105 K they are three times higher than at room temperature (see also Fig.68). The decrease in intensity of the spectrum measured at 4 K is an artefact due to liquid helium. The excitation spectrum at 5 K is depicted in Fig.67. No fine structure is visible at low temperatures, indicating a rather large Huang-Rhys coupling parameter. Lifetimes at low temperatures are about 700 ns and the quenching temperature is approx. 240 K. With Equation 13, the energy barrier for thermal quenching is crudely estimated to be 0.35 eV. Both intensities and lifetimes increase with decreasing temperature (see Fig.68); intensities at 4K are about 2 times higher than at room temperature. The small offset in the intensities between 150 and 170 K is due to small fluctuations in temperature while heating and cooling the cryostat.

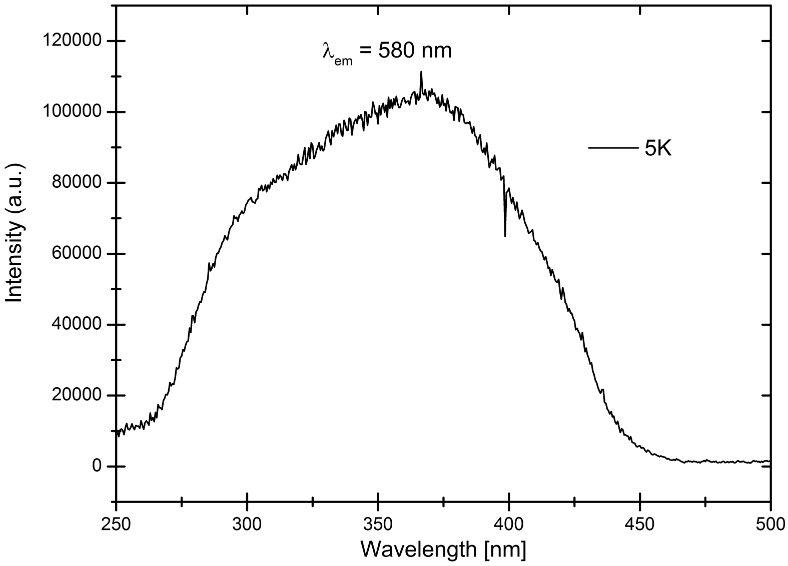

Figure 67: Excitation spectrum (FL920) of $KMgH_3$:Eu^{2+} (approx.1 mol%) at 5K. Emission at 580 nm.

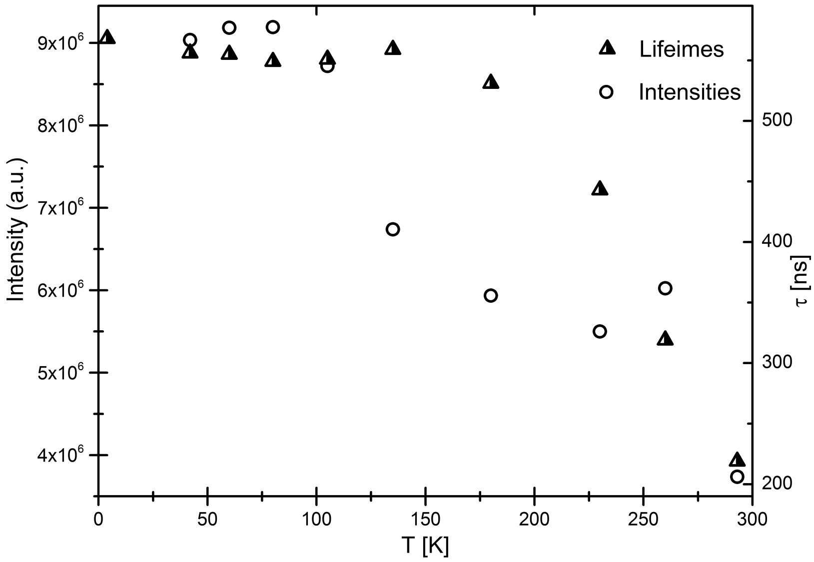

Figure 68: Temperature dependence of the emission intensities and decay times of KMgH$_3$:Eu^{2+} (approx.1 mol%). Excitation at 376.8 nm, emission at 570 nm. Quenching temperature approx. 240 K.

4.2.7 NaMgH$_3$:Eu^{2+}

NaH and EuH$_2$ were mixed with fine Mg powder and heated twice to approx. 480°C under 100 bar hydrogen pressure for two days.

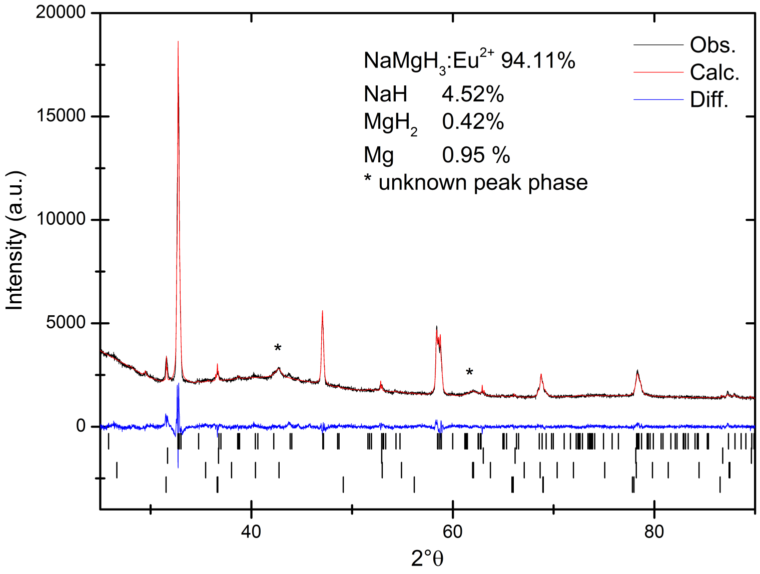

Figure 69: Rietveld refinement of the crystal structure of NaMgH$_3$:Eu^{2+} (approx. 1 mol%).

The desired phase was obtained as a yellow-orange powder with small amounts of NaH and showed a weak dark red luminescence. An alternative synthesis route via the melting reaction of Na, Eu and Mg did not yield the desired product. $NaMgH_3$ crystallizes in the orthorhombic $GdFeO_2$ structure type[44], for structural data see appendix Tabl.39) with Mg on the *4b* and Na on the *4c* site. Assuming Eu^{2+} to occupy the Na^+ site, since the magnesium site seems to be too small, it is coordinated by ten hydrogen ligands forming a dicapped distorted cube with distances between 227.5 and 300.4 pm (average 263.7 pm).

$NaMgH_3$:Eu^{2+} shows almost no emission intensity at RT, but with a decrease in temperature the emission intensities increase significantly (Fig.70).

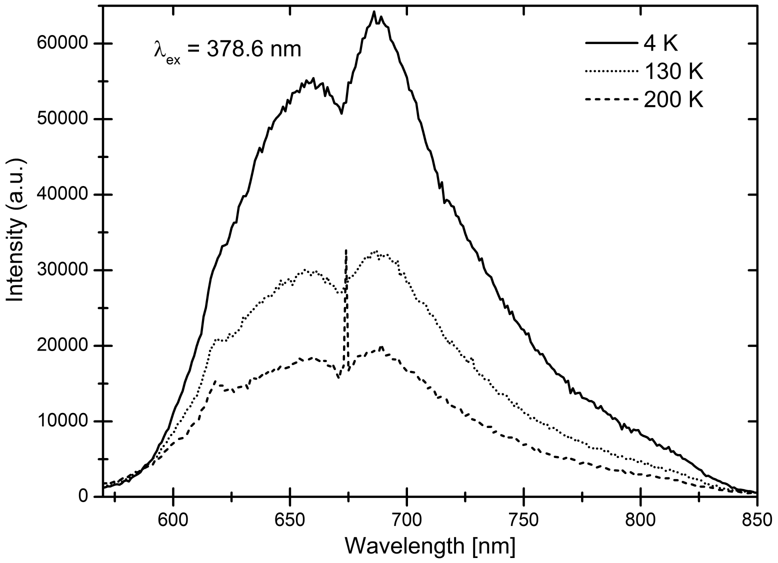

Figure 70: Temperature-dependent emission spectra (FL920) of $NaMgH_3$:Eu^{2+} (approx. 1 mol%). Excitation at 376.8 nm.

At 4 K the emission is more than three times higher compared to 200 K. The observation of two emission peaks is an artefact due to the missing corrector for lamp sensitivity. Since the correction functions possess a too large factor at long emission wavelengths, it does not reproduce the spectra correctly and was therefore switched off. However, a spectrum corrected for lamp sensitivity is shown in the Appendix (see 8.3, Fig.124). The emission maximum is at about 700 nm, however, due to the appearance of the two peaks it is impossible to define the emission maximum correctly. Thus the emission occurs at almost as long wavelengths as in CaH_2:Eu^{2+}, for which even shorter average metal-hydrogen distances (234 pm) were observed than for $NaMgH_3:Eu^{2+}$ (259 pm).

The decay times are extremely short even at 4 K, indicating that the emission is still partly quenched. The fitting of the decay curve at 4 K was carried out using a bi-exponential function and yielded lifetimes of 20 and 80 ns.

4.2.8 Comparison of spectroscopic properties of the $4f^6 5d$ states of Eu(II) in perovskites

A comparison of the spectroscopic properties of the $4f^6 5d$ states of Eu(II) in the host lattices $LiMH_3$ (M = Sr, Ba) and $LiBaF_3$, which all have the same perovskite structure type, is made (see Table 13). A striking feature of the hydridic host lattices is the wide redshift of the emission energies of Eu(II) compared to the known isotypic fluoride compound $LiBaF_3$.

In order to explain the redshift of the emission in hydrides in comparison to fluorides, the contribution due to the nephelauxetic effect and the crystal field splitting is separated.

Table 13: Comparison of spectroscopic properties of the $4f^6 5d$ states of Eu(II) in fluoride perovskites and hydride perovskites studied within this work.

Compound	Onset e_g (nm)	Onset t_{2g} (nm)	Crystal field splitting (cm^{-1})	Bary-center (cm^{-1})
$LiBaF_3:Eu^{2+}$	335	275	6500	33450
$LiBaH_3:Eu^{2+}$	485	355	7550	24570
$LiBaD_3:Eu^{2+}$	483	355	7470	24600
$LiSrH_3:Eu^{2+}$	530	375	7800	22880
$LiSrD_3:Eu^{2+}$	528	376	7660	22900

The crystal field splitting for the cuboctahedral field between the $4f^6 5d(e_g)$ and $4f^6 5d(T_{2g})$ is estimated from the position of the zero-phonon line and the onset of the $4f^6 5d(T_{2g})$ excitation band in the excitation spectra, whereas the barycenter is the degeneracy weighted average of the $4f^6 5d(e_g)$ and $4f^6 5d(T_{2g})$. The data clearly show a shift of the barycenter to some 10000 cm^{-1} lower energy caused by the strong nephelauxetic effects of the covalent hydride ligand. The crystal field splitting is also larger, however, its influence is ten times smaller. For $KMgH_3:Eu^{2+}$ and $NaMgH_3:Eu^{2+}$ the crystal field splitting cannot be calculated due to the insufficient resolution of the excitation spectrum which does not allow an assignment of the e_g states.

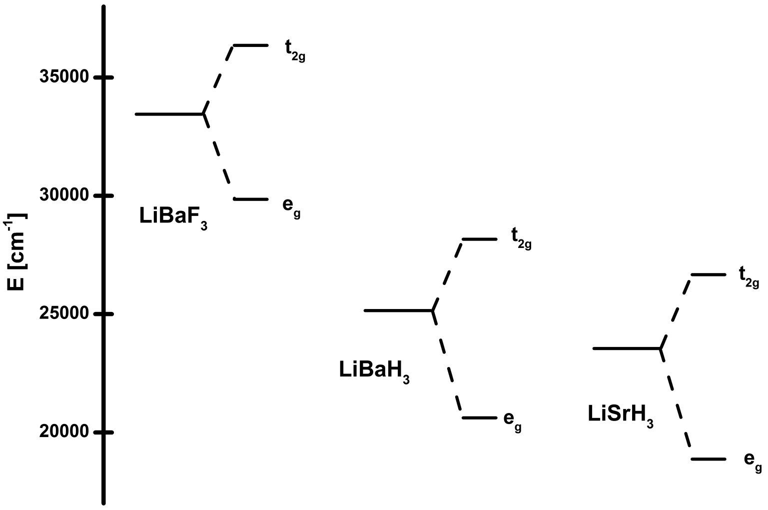

Figure 71: Schematic comparison of spectroscopic properties of the $4f^65d$ states of Eu(II) in $LiBaF_3$, $LiBaH_3$ and $LiSrH_3$.

4.2.9 Comparison of Goldschmidt's tolerance factors in perovskites used as host lattices

Tolerance factors according to Goldschmidt are given for normal and inverse perovskites used as host lattice (see Table 14). Tolerance factors were determined from the crystal radii given by Shannon[27] and, in case of hydrides, a crystal radius for hydride of 140 pm (t) or 153 pm (t_M) as suggested by Gibb and Morris[54,72]. Furthermore, for the hydrides tolerance factors based on cation-hydride distances calculated from the lattice parameters and the crystal radii by Shannon of the cations (from both, B- and A-site cations) are given. For the inverse cubic perovskites $LiSrH_3$, $LiBaH_3$, $LiBaF_3$ and the normal cubic perovskite $KMgH_3$ tolerance factors between 0.9 and 1.0 are determined, which is in agreement with the experimental observation. However, in accordance with previous estimations[79], the tolerance factor for $NaMgH_3$ indicates the existence of a cubic perovskite, but the experimentally observed structure shows a distortion[44]. A hypothetical cubic perovskite structure was calculated (see Section 6.3.2 for details and Bader charges) and a lattice constant of 386.2 pm was obtained. A comparison of the atomic distances gives 193.0 pm (Mg-H) and 272.9 pm (Na-H) for the hypothetical cubic structure and 196.1-198.0 (average 197) pm (Mg-H) and 227.5-300.4 (average 263.7) pm (Na-H) for the existing orthorhombic variant. The Na-H distance in a hypothetical cubic structure is thus only slightly smaller than the K-H distance in $KMgH_3$ (approx. 283.5 pm), even though the difference in the effective ionic radii or the crystal radii for a twelve-fold coordination amounts to 25 pm[27] and the Na-H distance in NaH is approx. 244 pm (lattice constant 488 pm[150]). Since the distortion and tilting of the octahedra leads to only a small change in the Mg-H bond, but a shortening of the Na-H bond, the formation of energetically favorable interatomic distances might be the reason for the existence of a distorted perovskite variant.

Table 14: Hydride crystal radii and tolerance factors for normal and inverse cubic perovskites.

ABX_3	t (t_M)	r_{H^-} [pm] from B-cation	t_B	r_{H^-} [pm] from A-cation	t_A	cub.
$SrLiH_3$	0.9162 (0.905)	101.79	0.9578	113.23	0.9437	y
$BaLiH_3$	0.9684 (0.9545)	101.79	1.0205	109.54	1.0083	y
$BaLiF_3$	0.9947	-	-	-	-	y
$KMgH_3$	0.9949 (0.9793)	115.31	1.0303	106.7	1.0447	y
$KMgF_3$	1.024	-	-	-	-	y
$NaMgH_3$	0.91 (0.9053)	-	-	-	-	n

4.3 Ternary magnesium hydrides doped with Eu(II)

4.3.1 $Eu_xSr_{1-x}MgH_4$

Heating the alloys $Eu_xSr_{1-x}Mg$ in the autoclave at high hydrogen pressures and temperatures of about 300°C for about 4-5 days did not yield pure samples. It is remarkable that samples with small x are generally easier to prepare than such with high europium content and that samples hydrogenated via DSC at 450°C and 50 bar (reaction time about 10 hours) always contained more of the desired phase than those prepared in the autoclave at 300°C and 80 bar. Additional information about hydrogenation conditions can be found in[34]. Samples with $x \leq 0.2$ merely contained the binary hydrides as impurity phases, whereas samples with $x > 0.2$ additionally contained the phases $Eu_xSr_{1-x}Mg_2H_6$, $Eu_xSr_{2-x}MgH_6$ as well as Mg in different proportions. An exemplary overview of the identified phases within the samples of nominal composition $Eu_xSr_{1-x}MgH_4$ for $x \leq 0.02$, which were prepared from the alloys by hydrogenation at 300°C and 80 bar, is given in Table 15. The mole fractions might vary slightly in other samples, however, preparation via the alloys and the hydrogenation conditions mentioned above always led to the formation of the binary hydrides as impurity phases. Samples with higher europium content are mentioned in[34], but will not be considered here further, since only samples with low europium content were of interest for luminescence experiments.

Table 15: Exemplary overview of identified phases within the samples of nominal composition $Eu_xSr_{1-x}MgH_4$; synthesis via hydrogenation of the alloys.

x	Identified phases (Mole fraction [%])
0.0	$SrMgH_4$ (87.8), SrH_2 (12.2)
0.005	$Eu_{0.0005}Sr_{0.0995}MgH_4$ (61.04), $Eu_{0.0005}Sr_{0.0995}H_2$ (27.27), Mg (11.69)
0.01	$Eu_{0.001}Sr_{0.099}MgH_4$ (51.4), $Eu_{0.001}Sr_{0.099}H_2$ (48.6)
0.02	$Eu_{0.002}Sr_{0.098}MgH_4$ (65.3), $Eu_{0.002}Sr_{0.098}H_2$ (34.7)

$SrMgH_4:Eu^{2+}$ (1 and 2 mol%) showed a lime green luminescence (Fig. 72); lumiscence spectra of $SrMgH_4:Eu^{2+}$ (1 mol%) are shown in Fig. 73. The lifetime at RT is approx. 417 ns. It is interesting to notice that the lifetime at RT is still rather long and thus the luminescence is not completely quenched.

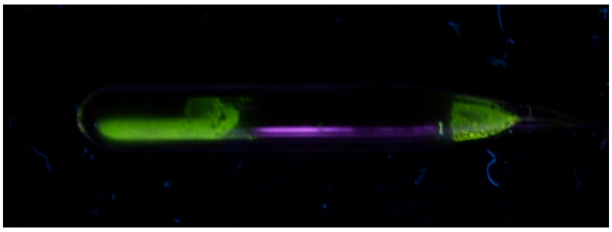

Figure 72: $SrMgH_4:Eu^{2+}$ (1.0 mol%) under UV-light (365 nm).

The emission spectrum shows a broad band emission as it is typically observed for Eu(II) emission from the $4f^65d$ level. The emission maximum is at about 536 nm. The green luminescence is strongly visible even though large amounts of the binary SrH_2 are present. A luminescence of SrH_2 visible in the spectra can be excluded, because its luminescence is known to be in the red color region and of very weak intensity.

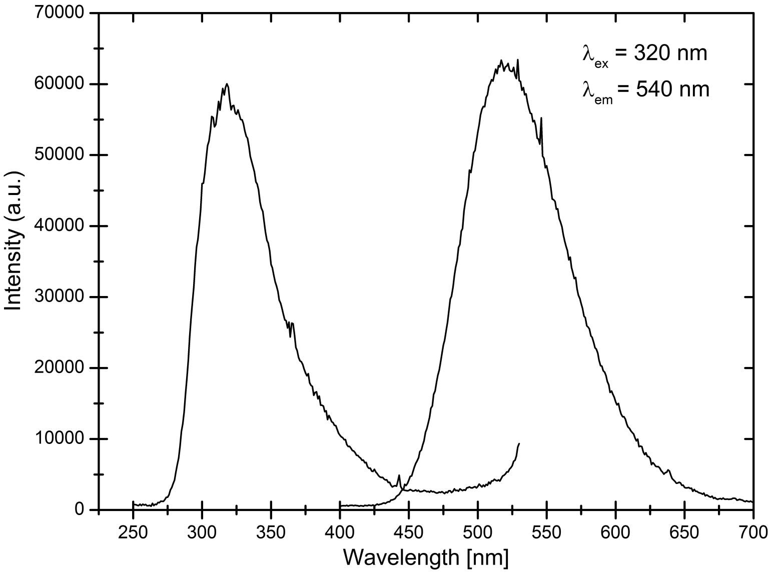

Figure 73: Luminescence excitation and emission spectra (FL920) of $SrMgH_4:Eu^{2+}$ (1.0 mol %) at 293 K. Emission maximum 536 nm.

As hydrogenating the alloys $Eu_xSr_{1-x}Mg$ at the conditions mentioned above did not yield pure samples, another preparation method was tested. A stoichiometric mixture of $Eu_xSr_{1-x}H_2$ (x = 0, 0.005) and Mg powder were heated twice in an autoclave at about 480°C and 140 bar hydrogen pressure for 5 days. The desired products $Eu_xSr_{1-x}MgH_4$ (x = 0, 0.005) were obtained with only small amounts (1-3 w%) of $Eu_xSr_{1-x}H_2$ present. The Rietveld refinement of the crystal structure of $SrMgH_4:Eu^{2+}$ (0.5 mol%) is shown in Fig. 74. Assuming a crystal structure as given in[47] for $SrMgH_4$, the refined lattice parameters a = 397.478(3) pm, b = 1372.21(1) pm and c = 558.752(5) pm and for $SrMgH_4:Eu^{2+}$ (0.5 mol%) a = 397.532(4) pm, b = 1372.41(1) pm and c = 558.817(6) pm were obtained. If Eu(II) occupies the strontium position, it is coordinated by nine hydrogen atoms forming a distorted trigonal prism with europium-hydrogen distances between approx. 245 pm and 280 pm. For a hypothetical occupation of the magnesium site, the coordination polyhedron is a distorted octahedron with europium-hydrogen distances between 182 pm and 199 pm.

Table 16: Overview of the identified phases within the samples of nominal composition $Eu_xSr_{1-x}MgH_4$, synthesis via solid state reaction of $SrH_2(:Eu^{2+})$ and Mg powder under H_2 pressure.

x	Identified phases (Weight fraction [%])
0.0	$SrMgH_4$ (97.25), SrH_2 (2.75)
0.005	$Eu_{0.0005}Sr_{0.0995}MgH_4$ (97.72), $Eu_{0.0005}Sr_{0.0995}H_2$ (2.28)

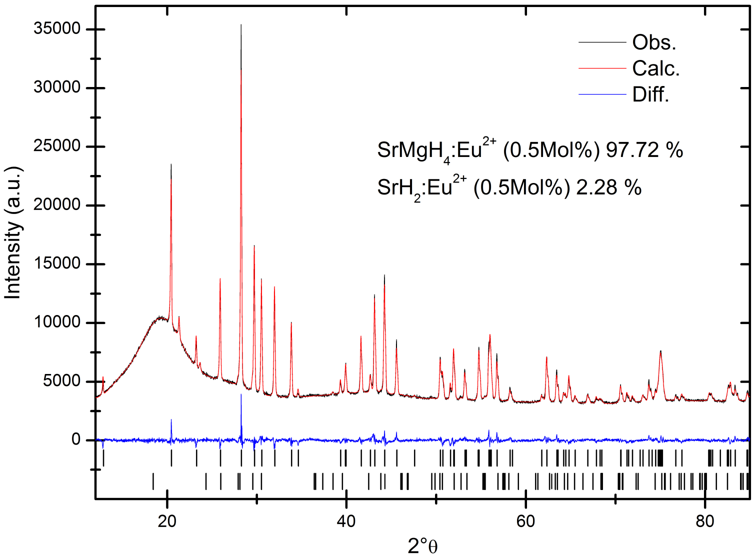

Figure 74: Rietveld refinement of the crystal structure of $SrMgH_4:Eu^{2+}$ (0.5 mol%).

However, $SrMgH_4:Eu^{2+}$ (0.5 mol%) did not show any luminescence. This suggests that the different preparation methods lead to different arrangements of the coordination spheres surrounding europium. Starting from the reactant $SrH_2:Eu^{2+}$, europium possibly occupies merely the strontium site, whereas starting from the alloy europium might partly occupy the magnesium site or an interstitial site as well.

4.3.2 $BaMgH_4:Eu^{2+}$

Heating a mixture of $BaH_2:Eu^{2+}$ (0.5 mol%) and fine magnesium powder to about 450°C at 120 bar hydrogen pressure for 7 days yielded only a small amount of the desired phase $BaMgH_4:Eu^{2+}$, but larger amounts of $Ba_6Mg_7H_{26}:Eu^{2+}$ (about 2/3) and traces of $Ba_2MgH_6Eu^{2+}$. The sample showed a bright yellow emission under UV-light (see Fig.76), but different grains in the sample could be distinguished. It is not clear to which of the phases the emission belongs or if it is caused by a mixture of the different phases. Heating the sample two more times for 3 days under high hydrogen pressures (80-100 bar) led to a decrease in the amount of $Ba_6Mg_7H_{26}:Eu^{2+}$, a slight increase in $BaMgH_4:Eu^{2+}$ and a rather large increase in $Ba_2MgH_6:Eu^{2+}$ (see Table 17 for estimated weight fractions). No change in luminescence color nor significant change in intensities was observed. However, no single phase samples could be obtained. In order to carry out reliable luminescence studies, it is therefore indispensable to optimize the preparation method.

Table 17: Overview of the weight fractions (w%) of the identified phases within a mixture of $BaH_2:Eu^{2+}$ (0.5 mol%) and fine magnesium powder after heating n times (approx.450°C and 120 bar).

n	$BaMgH_4:Eu^{2+}$	$Ba_2MgH_6:Eu^{2+}$	$Ba_6Mg_7H_{26}:Eu^{2+}$
1	15.58	18.51	65.92
2	19.41	38.38	42.20
3	19.89	43.67	36.44

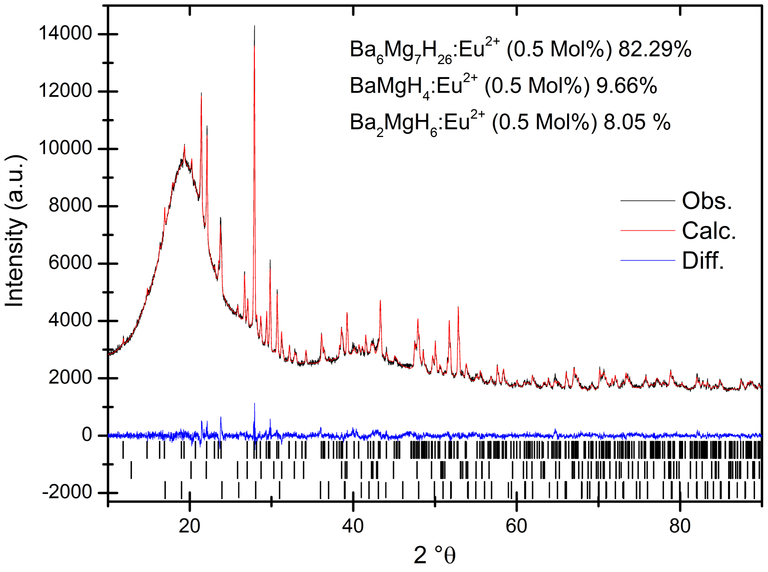

Figure 75: Rietveld refinement of the crystal structure of $Ba_6Mg_7H_{26}$:Eu^{2+} (0.5 mol%).

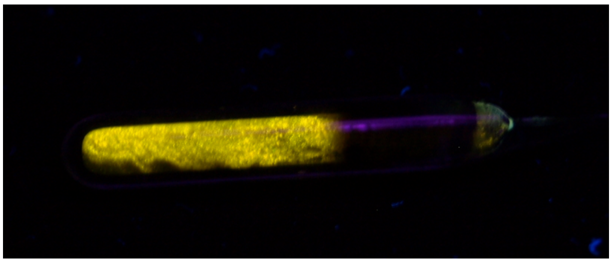

Figure 76: $Ba_6Mg_7H_{26}$:Eu^{2+}/$BaMgH_4$:Eu^{2+}/$Ba_2MgH_6Eu^{2+}$ (0.5 mol%) under UV-light (365 nm).

Luminescence excitation and emission spectra (FL920) of the mixture $Ba_6Mg_7H_{26}$:Eu^{2+} (0.5%) and $BaMgH_4$:Eu^{2+} (0.5%) after heating once are shown in Fig.77. The emission maximum is about 577 nm and the lifetime of the mixture at RT is approx. 570 ns.

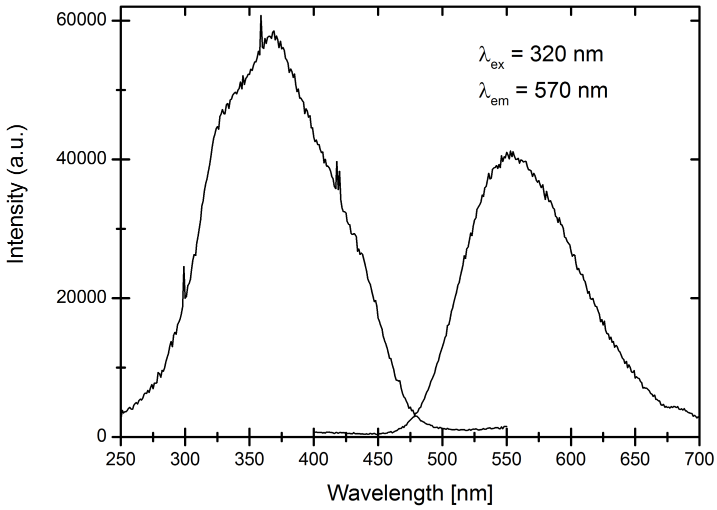

Figure 77: Luminescence excitation and emission spectra (FL920) of the mixture $Ba_6Mg_7H_{26}$:Eu^{2+} (0.5 mol%) and $BaMgH_4$:Eu^{2+} (0.5 mol%) at 293 K. Emission maximum about 577 nm.

4.3.3 $Ca_4Mg_3H_{14}$:Eu^{2+}

Attempts to obtain pure $Eu_xCa_{4-x}Mg_3H_{14}$ from $Eu_xCa_{1-x}H_2$ and Mg powder under hydrogen pressure were not successful. Even after heating the samples several times to 480°C under 120-150 bar for 4 days, only small amounts (max. 20%) of the desired phase and large amounts of CaH_2 and MgH_2 were obtained. Samples show a very weak red emission which might also originate from CaH_2:Eu^{2+}.

Table 18: Overview of the weight fractions (w%) of the identified phases within a mixture of CaH_2:Eu^{2+} (0.5 mol%) and fine magnesium powder after heating n times (approx. 450°C and 120 bar).

n	$Ca_4Mg_3H_{14}$:Eu^{2+}	$Ca_{19}Mg_8H_{54}$:Eu^{2+}	CaH_2:Eu^{2+}	Mg	MgH_2
1	2.60	0.00	52.64	9.72	35.05
2	24.88	0.00	50.72	7.89	16.51
3	17.99	0.72	58.67	5.93	16.69

4.4 Fluorides and hydride-fluorides

4.4.1 EuH_xF_{2-x}

Heating different ratios of EuF_2 and EuH_2 for approx. 3 days at 470°C under approx. 30 bar hydrogen pressure lead to yellow powders emitting an orange-red luminescence (see Fig. 78).

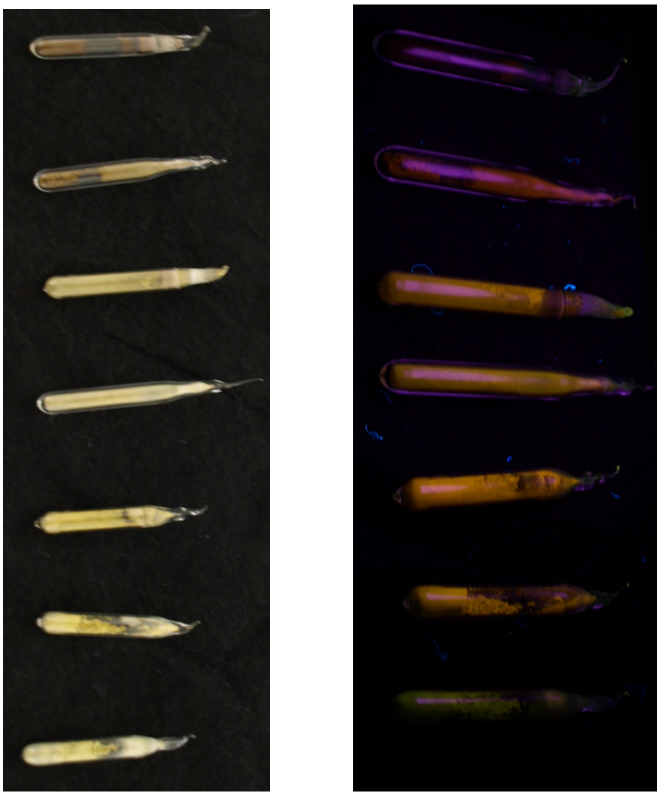

(a) At daylight. (b) Under UV-excitation.

Figure 78: From top to bottom EuH_xF_{2-x} with x: 0.666, 0.506, 0.400, 0.330, 0.278, 0.248, 0.200 at daylight (a) and under UV excitation (365 nm) (b).

X-ray diffraction data showed the presence of large amounts of a cubic EuH_xF_{2-x} phase (fluorite type) and in some samples small amounts of an orthorhombic EuF_xH_{2-x} phase ($PbCl_2$ structure type). Occupation numbers have been refined. However, due to the small difference in the scattering behavior of hydride and fluoride in an X-ray pattern next to a heavier element such as europium, these occupation numbers are of limited accuracy. It seems that the refined occupation number for fluoride is overestimated by TOPAS. In Table 19 the refined lattice parameters and occupation numbers are listed.

Table 19: Refined lattice parameters (pm) and occupation numbers in EuH_xF_{2-x} (x according to initial weight), space groups $Fm\bar{3}m$ and *Pnma* (X-ray data were collected on the *D8* diffractometer) and emission maxima at RT (data collected on the FLS920). Estimated standard deviations provided by the program TOPAS are given in brackets. (*rest EuO)

x	0.666	0.506	0.400	0.330
λ_{em} [nm]	685	636, (685)	605, (685)	605, (685)
fluorite structure type				
w%	90.21	96.50	97.9	98.83
a [pm]	584.027(7)	584.078(2)	584.439(2)	584.009(3)
F	0.85(1)	0.885(6)	0.941(5)	0.948(6)
$PbCl_2$ structure type				
w%	2.29*	3.50	2.10	1.17
a [pm]	630.1(3)	632.1(3)	630.3(3)	626.8(5)
b [pm]	378.1(2)	380.2(1)	381.1(1)	382.3(2)
c [pm]	724.7(5)	723.8(2)	722.7(3)	724.9(5)
F	0.1	0.0	0.25(50)	0.1(9)
x	0.278	0.248	0.200	0.104
λ_{em} [nm]	605, (685)	595, (685)	570, (685)	-
fluorite structure type				
w%	100	100	100	100
a [pm]	584.244(2)	584.006(3)	584.166(1)	584.238(2)
F	0.931(6)	0.975(6)	0.992(5)	1.000(5)

Table 20: Decay times of EuH_xF_{2-x} measured at RT. Analysis was carried out using a single exponential function. Emission wavelength 580 nm, except for x = 0.5, 600 nm.

x	0.5	0.4	0.33
τ (ns)	14	13	14

Luminescence emission and excitation spectra, as well as decay times, were measured at RT. Luminescence spectra are shown in Fig. 80 and 81 and decay times are listed in table 20. The emission maxima are listed in Table 19.

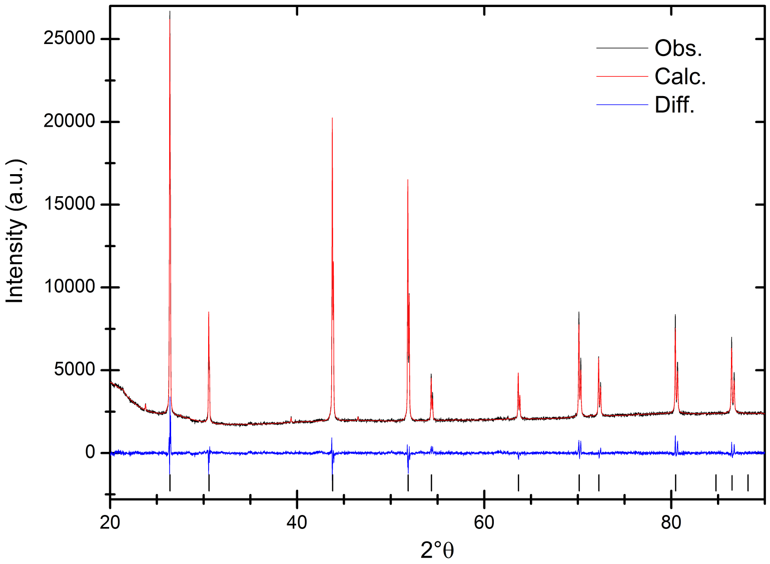

Figure 79: Rietveld refinement of the crystal structure of $EuH_{0.278}F_{1.722}$.

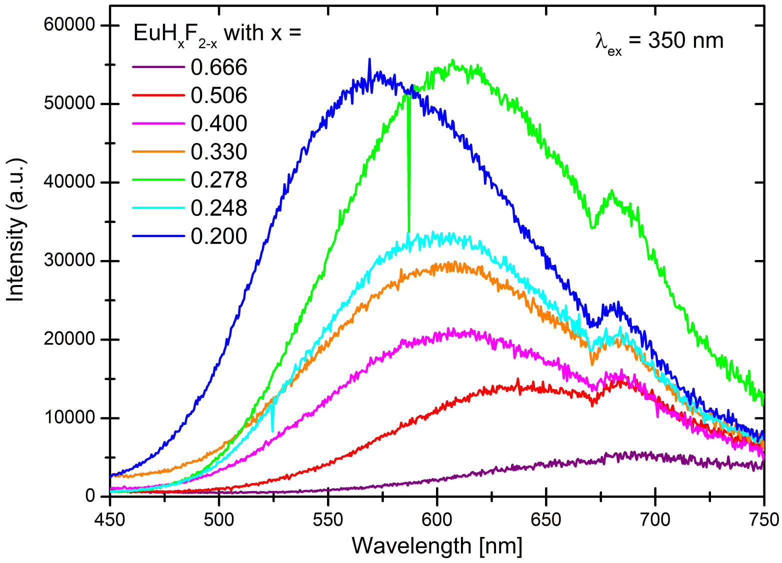

Figure 80: Luminescence emission spectra (FL920) of EuH_xF_{2-x} at 293 K. Emission maxima are listed in Table 19. All spectra measured under the same instrumental conditions.

The sample with x = 0.666 shows only an emission maximum at 685 nm, whereas all other samples show a minor maximum at 685 nm and a main maximum at shorter wavelength which is shifted to higher energies for increasing fluoride contents. This indicates two slightly different luminescence centers and formation of a rather inhomogeneous hydride-fluoride solid solution series with the preference to form clusters with increased hydride content. The ratios of the main and minor maxima are given in Table 21. Note that the ratio is only estimated, since it is calculated based on the height of the emission maxima. A calculation based on the peak area is hampered by the overlap of both emission peaks. However, the wider emission peak of the main maximum suggests a higher content of the luminescence center I.

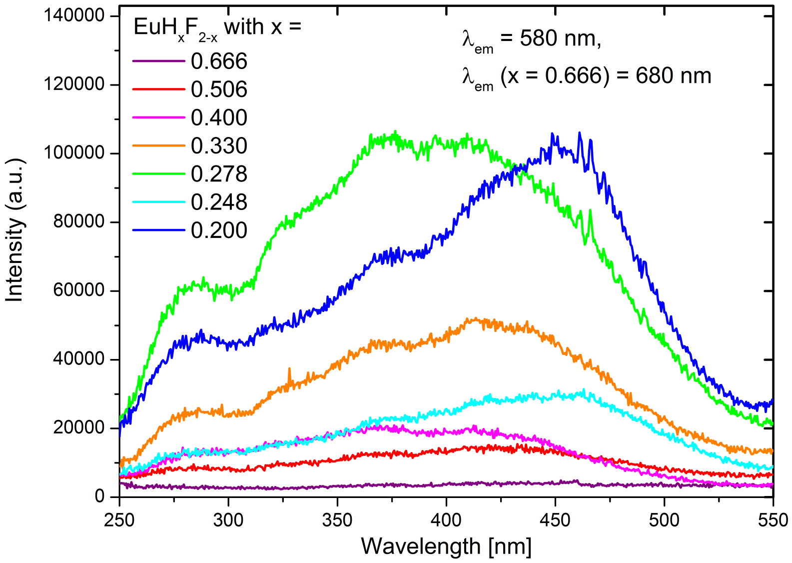

Figure 81: Luminescence emission spectra (FL920) of EuH$_x$F$_{2-x}$ at 293 K.

Table 21: Ratio of the main (I) and minor (II) emission maximum of EuH$_x$F$_{2-x}$ measured at RT and determined from the height of the emission maxima. Ratio (II) = 1- ratio (I). Excitation wavelength 350 nm.

x	0.666	0.506	0.400	0.330	0.278	0.248	0.200
I	0	0.49	0.57	0.59	0.60	0.61	0.69

The blueshift of the main emission maximum with increasing fluoride content is extremely large, which might be due to the large difference in chemical hardness and covalence between fluoride and hydride.

Exemplary, temperature dependent emission spectra and decay curves of $EuH_{0.278}F_{1.722}$ were recorded.

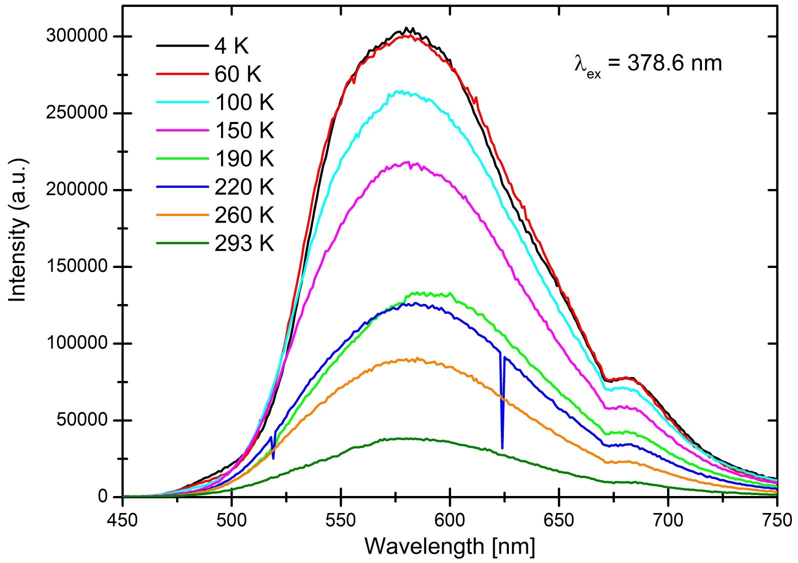

Figure 82: Temperature dependent luminescence emission spectra (FL920) of $EuH_{0.278}F_{1.722}$.

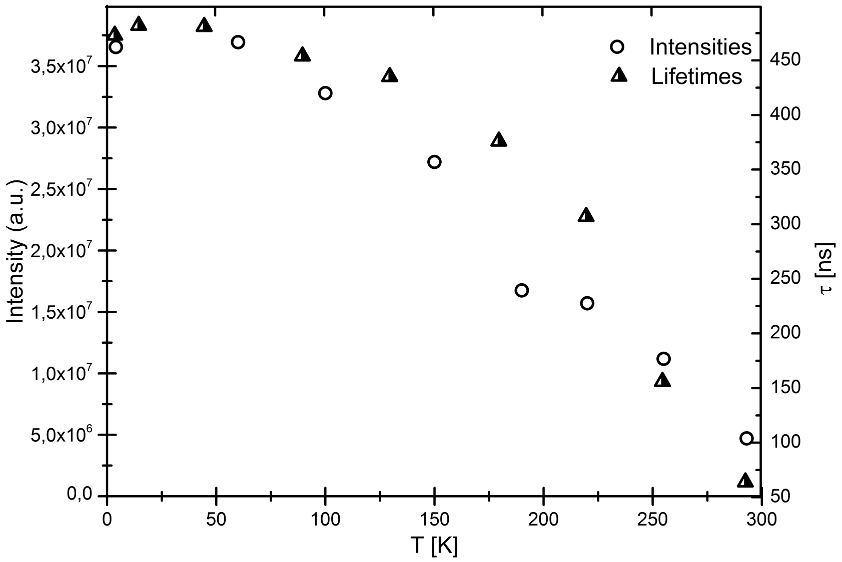

Figure 83: Temperature dependence of the emission intensities and decay times of $EuH_{0.278}F_{1.722}$. Excitation at 376.8 nm, emission at 570 nm. Quenching temperature approx. 200 K.

The temperature dependent spectra are shown in Fig.82. Intensities at low temperatures are about 10 times higher than at RT. The temperature dependence of the emission intensities and the lifetimes are shown in Fig.83. Since the decay curves showed a biexponential behavior even at 4 K, a biexponential fit was used. The biexponential fits yielded a longer lifetimes which is in the typical time range for Eu(II) and an extremely short lifetime. Only the longer lifetime is depictured in Fig.83; for a list of both lifetimes see Appendix (8.3 Table 45). Both emission intensities and lifetimes show an increase by the factor 10 at low temperatures compared to RT.

4.4.2 $SrH_xF_{2-x}:Eu^{2+}$

Mixtures of SrF_2 and $SrH_2:Eu^{2+}$ (0.5 mol%) (x = 0.5) or SrF_2, SrH_2 and EuH_2 (x = 0.2) were heated for approx.3 days at 470°C under approx.30 bar hydrogen pressure. A rather weak reddish emission of $SrH_{0.5}F_{1.5}:Eu^{2+}$ (0.125 mol%) under UV light was visible, whereas $SrH_{0.2}F_{1.8}:Eu^{2+}$ (0.5 mol%) did not show luminescence. Luminescence excitation and emission spectra were measured at RT. The lifetime at RT is 46 ns for $SrH_{0.5}F_{1.5}:Eu^{2+}$ (0.125 mol%).

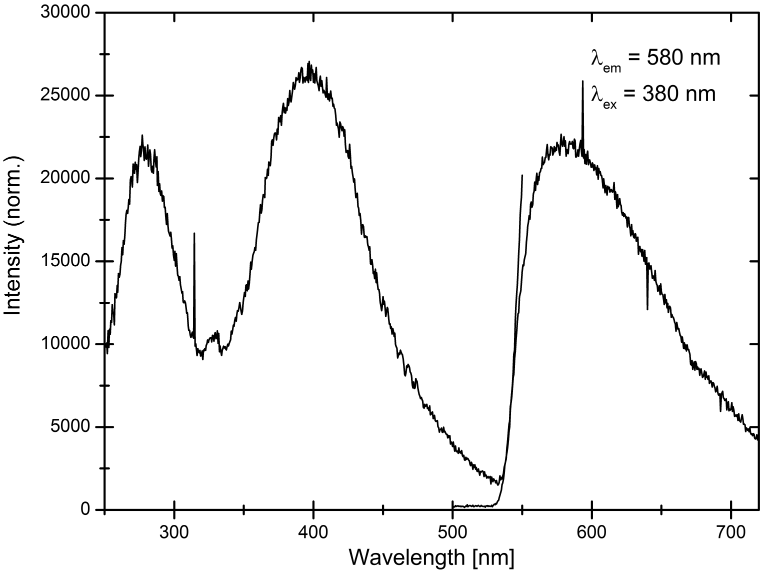

Figure 84: Luminescence excitation and emission spectra (FL920) of $SrH_{0.5}F_{1.5}:Eu^{2+}$ (0.1 mol%) at 293 K.

Similar to EuH_xF_{2-x}, X-ray diffraction data of samples of $SrH_xF_{2-x}:Eu^{2+}$ showed the presence of large amounts of a cubic SrH_xF_{2-x} phase (fluorite type). Furthermore, small amounts of SrO were present. Occupation numbers have been refined, but are to be doubted as discussed before.

In Table 22 the refined lattice parameters and occupation numbers are listed.

Table 22: Refined lattice parameters (pm) and occupation numbers in SrH_xF_{2-x}:Eu^{2+} (x according to initial weight), space group $Fm\bar{3}m$, X-ray data were collected on the *D8* diffractometer. Estimated standard deviations provided by the program TOPAS are given in brackets.

x	0.5 (Eu 0.125 mol%)	0.2 (Eu 0.5 mol%)
fluorite structure type		
w%	95.88, rest SrO	97.75, rest SrO
a [pm]	581.115(5)	580.050(2)
F	0.882(3)	1.0

4.4.3 $LiSrH_xF_{3-x}$(:Eu^{2+})

x = 0 Even though, according to literature, the hypothetic cubic perovskite $LiSrF_3$ supposedly does not form[38], the synthesis was tried. However, heating the binary fluorides in a Pt crucible in vacuum to 600°C, 700°C, 750°C and 800°C did not yield even a slight fraction of the desired product thus confirming earlier observations.

x = 1 1:1 mixtures of LiH and SrF_2 were heated for 4h together with small amounts of EuH_2 in a silica-pressure-cell under about 10 bar hydrogen and at 650°C using the laser heating system or inside a tube furnace. The reaction yielded an inhomogeneous product with white, orange and light purple powders. Those phase mixtures emitted a weak orange light (see for example Fig.85). Usually only between 3 -6 w% of a perovskite phase with a lattice parameter of approx. 383-384 pm and large amounts of unreacted educts were obtained. Therefore further test with the silica high-pressure cell are necessary in order to reach higher reaction temperatures and to clarify if the compound $LiSrHF_2$ exists.

Figure 85: Sample with traces of $LiSrHF_2:Eu^{2+}$ under UV light.

4.4.4 $LiBaH_xF_{3-x}(:Eu^{2+})$

x = 0 A solid-state reaction with dried BaF_2 and LiF in a slight excess (approx. 10%) was carried out inside a platinum crucible in an argon flow at approx. 770°C for seven days. Structural refinement of the X-ray powder data clearly show that $LiBaF_3$ crystallizes in the inverse cubic perovskite type. For the inverse model a R_{wp} of 6.1 % (R_{bragg} 4.3 %) was obtained, whereas the R_{wp} for the structural refinement assuming a normal cubic perovskite structure was 15.3 % (R_{Bragg} 18.9 %) and the reflections at 39.08 and 79.5 2°θ cannot be properly described using the normal model. A lattice constant of 399.692(1) pm was obtained.

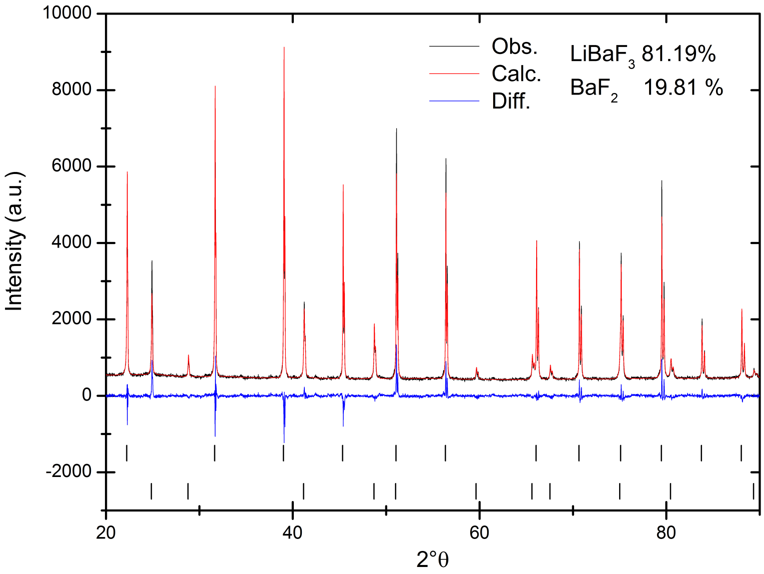

Figure 86: Rietveld refinement of the crystal structure of $LiBaF_3$.

x = 1 A 1:1 mixture of LiH and BaF_2 as well as small amounts of EuH_2 were heated two times to 480°C under 35 bar hydrogen pressure for about three days. The sample showed a bright green luminescence (see Fig.87). Rietveld refinement suggests the presence of three cubic perovskite phases and rests of unreacted BaF_2 (Fig.88).

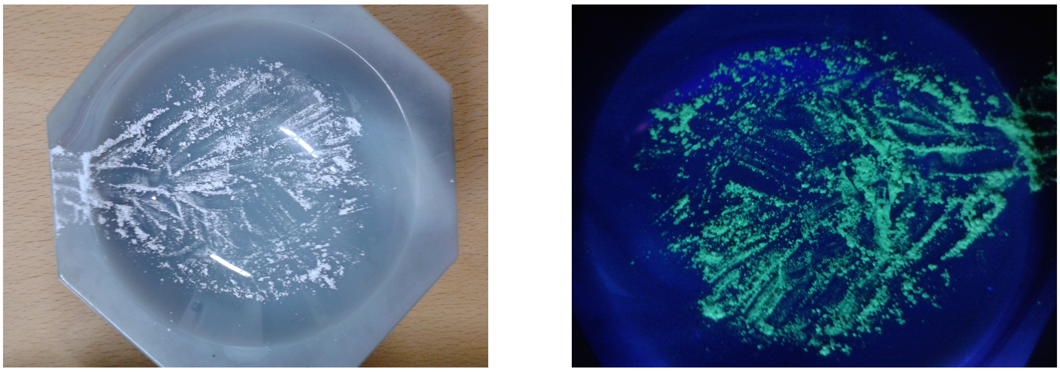

(a) At daylight.

(b) Under UV-excitation.

Figure 87: $LiBaHF_2:Eu^{2+}$ (1.0 mol%) (a) and under UV excitation (365 nm) (b).

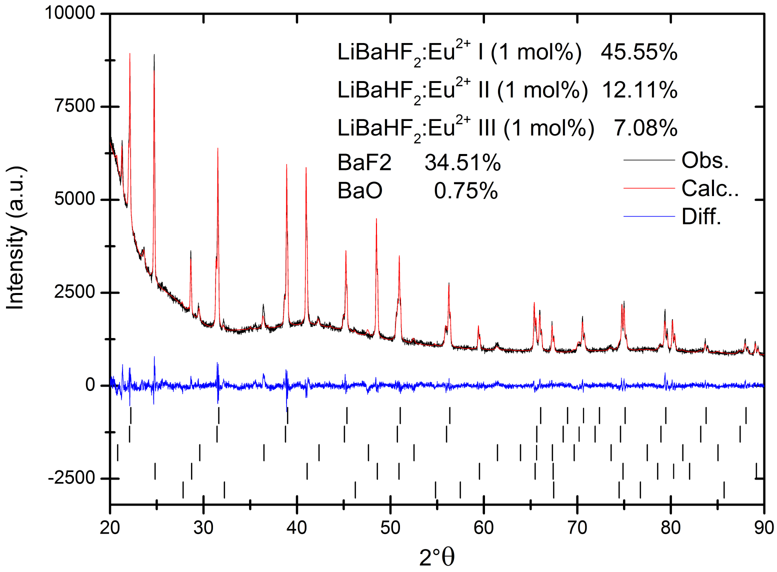

Figure 88: Rietveld refinement of the crystal structure of $LiBaHF_2:Eu^{2+}$ after heating once.

The lattice parameters of the three phases were 399.66(4) pm, 401.93(1) pm and 426.43(4) pm. After heating once the sum of all perovskite phases was 60 w%; after heating a second time it increased to 80 w%. The perovskite phase with the largest lattices parameter almost completely disappeared and the refined amount of BaF_2 also decreased significantly. The lattice parameter a of the other two perovskite phases were now 399.69(4) pm and 401.8(1) pm. This observation suggests that the reaction temperature might not be high enough and the sample not homogenous. Luminescence excitation and emission spectra are shown in Fig.89. The maximum of the emission is at 520 nm, which corresponds to a blueshift of 10 nm compared to the pure metal hydride.

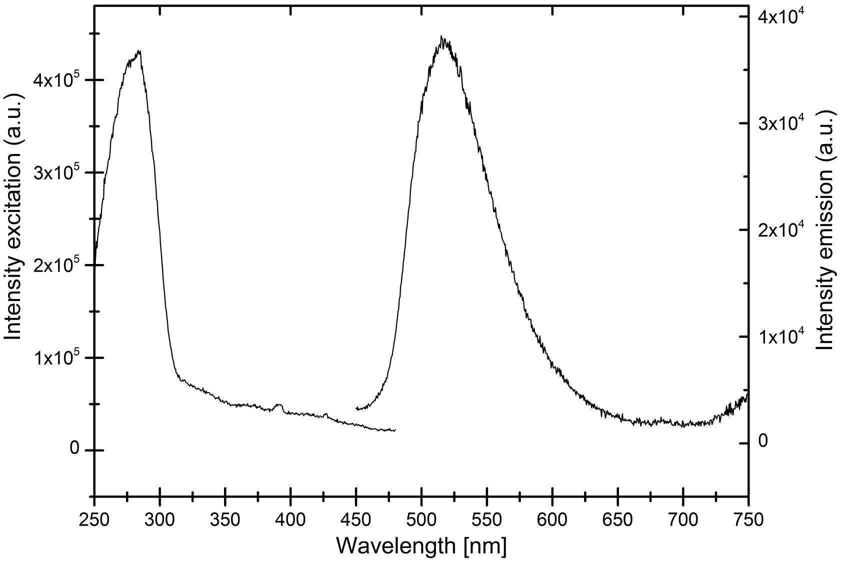

Figure 89: Luminescence excitation and emission spectra (FL920) of $LiBaHF_2$:Eu^{2+} (0.5 mol%) at 293 K.

4.4.5 $KMgH_xF_{3-x}$(:Eu^{2+})

x = 1 $KMgHF_2$:Eu^{2+} was synthesized via a solid state reaction of MgF_2, KH and EuH_2 in the silica high-pressure cell using an indium seal under 11 bar hydrogen for 4h at 650°C. Under UV light a green luminescence was visible (Fig.90) whose intensity was rather inhomogeneous. Relatively largely amounts of a normal cubic perovskite phase and rests of unreacted MgF_2 were obtained (Fig.91). The lattice parameter of the perovskite was refined to be 399.241(6) pm, which is slightly larger than the 398.35 pm given in literature[151] for $KMgF_3$ and smaller than the 402.869(4) pm obtained for $KMgH_3$:Eu^{2+} (1 mol%). The refinement of the occupation numbers yielded 0.199(1) for hydride. Taking the underestimation of hydrogen occupation numbers by TOPAS as already seen in Sect.4.4.2 into account, this value is approximately in agreement with the expected value of 1/3.

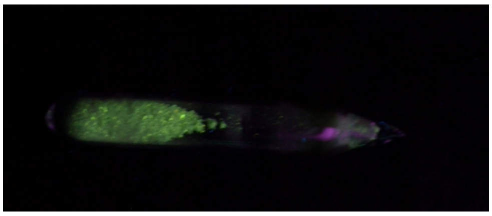

Figure 90: KMgHF_2:Eu^{2+} (0.5 mol%) under UV-light (365 nm).

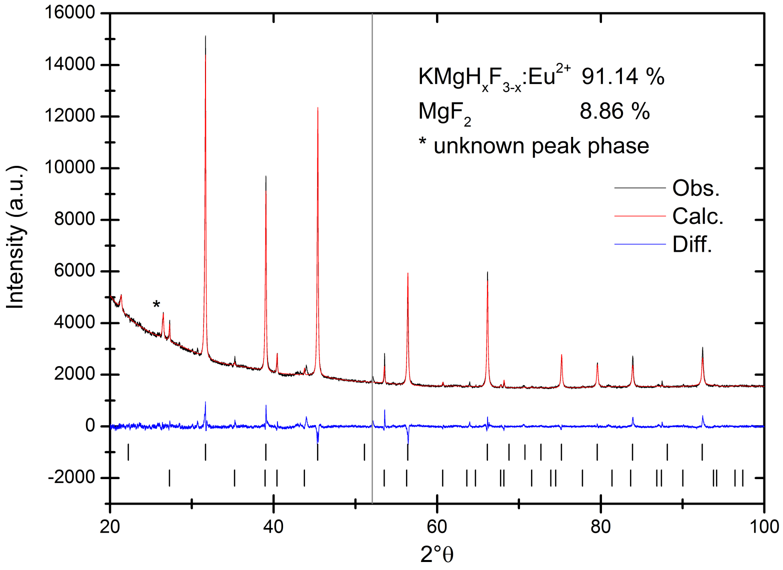

Figure 91: Rietveld refinement of the crystal structure of KMgHF_2:Eu^{2+} after heating once.

Luminescence excitation and emission spectra are shown in Fig.92. The maximum of the emission is at approx. 505 nm, which corresponds to a blueshift of 60 nm compared to the pure metal hydride. However, the inhomogeneity of the luminescence intensity suggests concentration gradients of europium or hydride and fluoride, so that the exact chemical composition of the brightly emitting phase is not known.

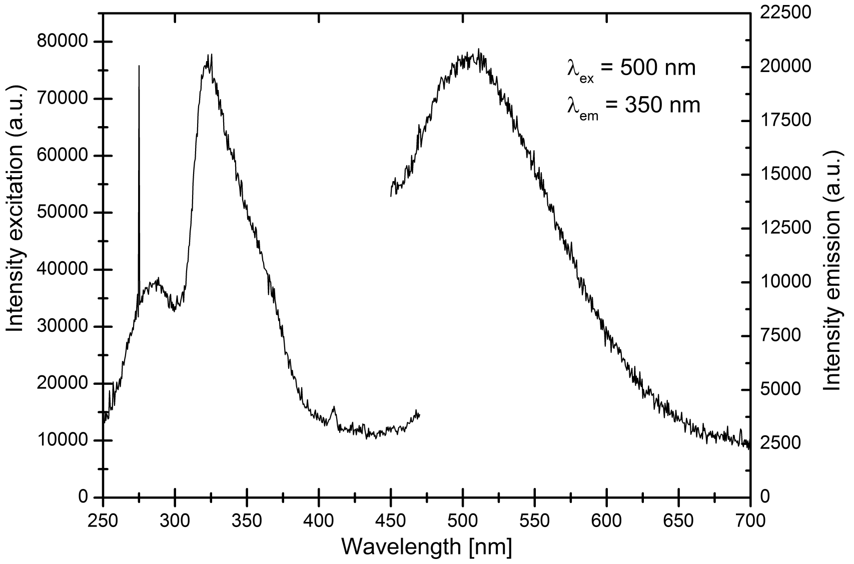

Figure 92: Luminescence excitation and emission spectra (FL920) of $KMgHF_2:Eu^{2+}$ (0.5 mol%) at 293 K.

4.5 Hydride-chlorides of europium

For syntheses of hydride-chlorides, commercial $EuCl_2$ containing considerable amounts of $EuCl_3$, EuO, Eu_4OCl_6, EuClO and an unknown phase, was used as educt. Consequently, products contained impurities. Eu(II) luminescence in Eu_4OCl_6 was studied before and an emission at approx. 467 nm was observed[152].

4.5.1 Eu_2H_3Cl

In order to obtain Eu_2ClH_3, stoichiometric mixtures of EuH_2 and $EuCl_2$ were heated twice in an autoclave under hydrogen pressure for 5 days (approx. 483°C and 120 bar). Anyhow, considerable amounts of EuHCl and only traces of Eu_2ClH_3 were obtained (Fig. 94). The following structure models for Eu_2ClH_3 were considered: I structural data from single crystal measurements[153], II Eu_2ClH_3 refined according to the Ba_2ClH_3 structure[154] and III alternative single crystal data[155]. Rietveld refinement (Fig.94) suggested the presence of Eu_2ClH_3 in the types I (3 w%) and II (2 w%). Furthermore, traces of at least one unknown phase were present. For structural data of those single crystals, see Appendix (Sect. 8.2.7).

The mixture showed a bright green emission under UV-light. Room temperature excitation and emission spectra, as well as decay curves, were recorded. The lifetime at RT is approx. 286 ns.

(a) At daylight.

(b) Under UV-excitation.

Figure 93: Phase mixture as shown in Fig.94 at daylight (a) and under UV excitation (365 nm) (b).

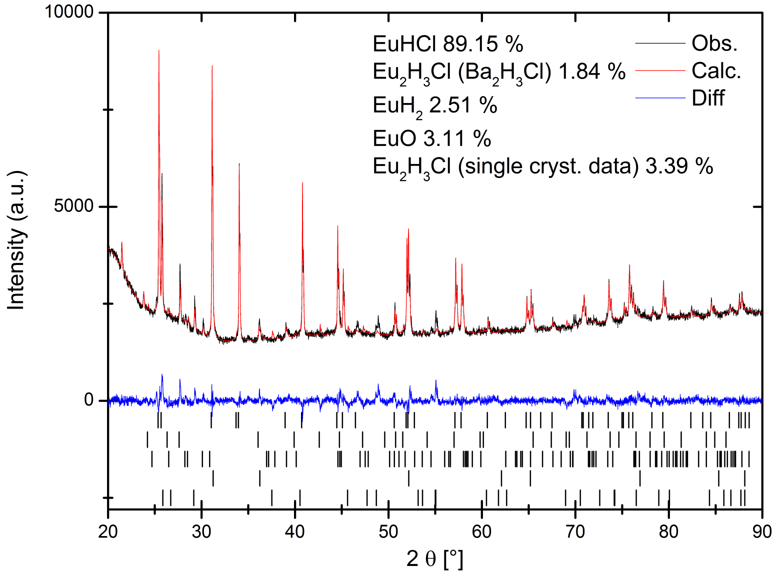

Figure 94: Rietveld refinement of the X-ray diffraction data of the phase mixture.

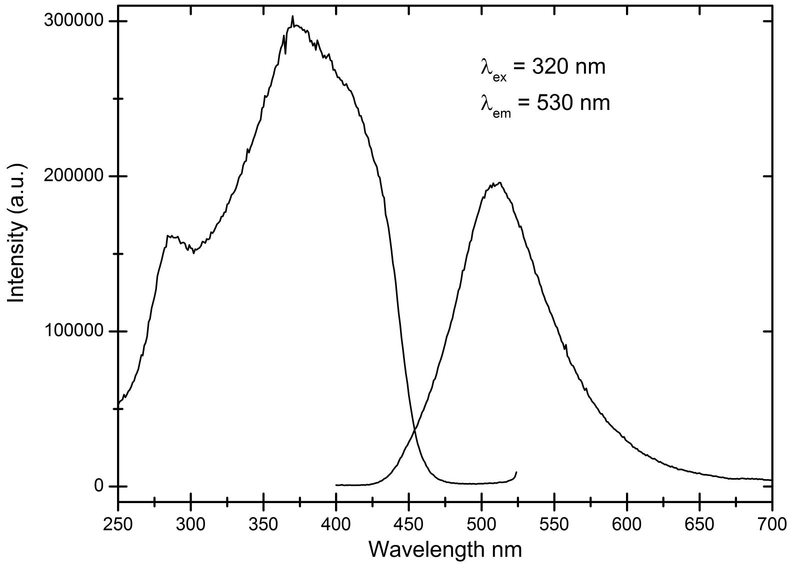

Figure 95: Luminescence excitation and emission spectrum (FL920) of the phase mixture of the sample “Eu_2H_3Cl” as shown in Fig.94 at 300 K. Emission maximum 520 nm.

4.5.2 EuHCl

A 1:1 mixture of EuH_2 and $EuCl_2$ was heated in an autoclave under hydrogen pressure for 5 days (approx. 483°C and 120 bar). EuHCl, about 4.5 w% of the main impurity phase Eu_4OCl_6

and small amounts of an unknown phase were obtained. The sample showed a bright bluish white luminescence.

(a) At daylight.

(b) Under UV-excitation.

Figure 96: EuHCl at daylight (a) and under UV excitation (365 nm) (b).

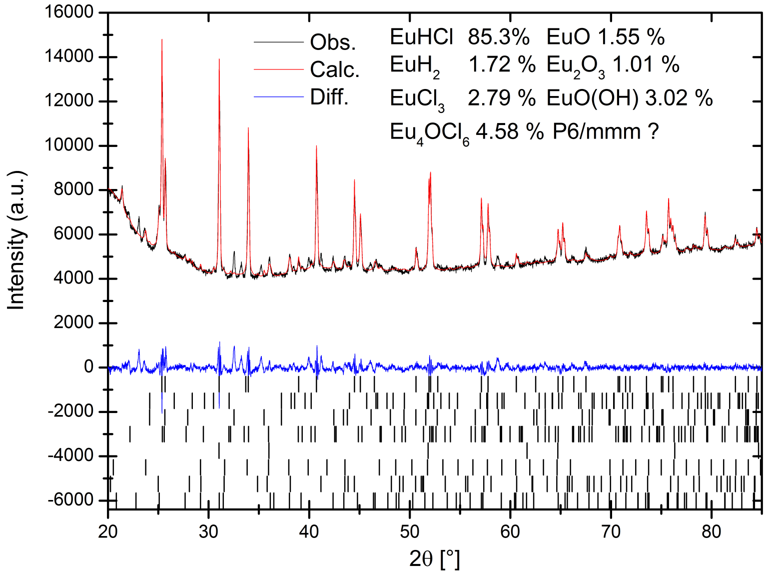

Figure 97: Rietveld refinement of the X-ray diffraction data of the phase mixture. Bragg markers from top to bottom: EuHCl, EuH_2, $EuCl_3$, Eu_4OCl_6, EuO, Eu_2O_3, EuO(OH), unknown phase.

A comparison of the luminescence emission and excitation spectra recorded at RT of the phase mixtures of the samples Eu_2H_3Cl and EuHCl is depicted in Fig.98. Note that the emission spectrum of “EuHCl” was recorded at the Fluoromax-4.

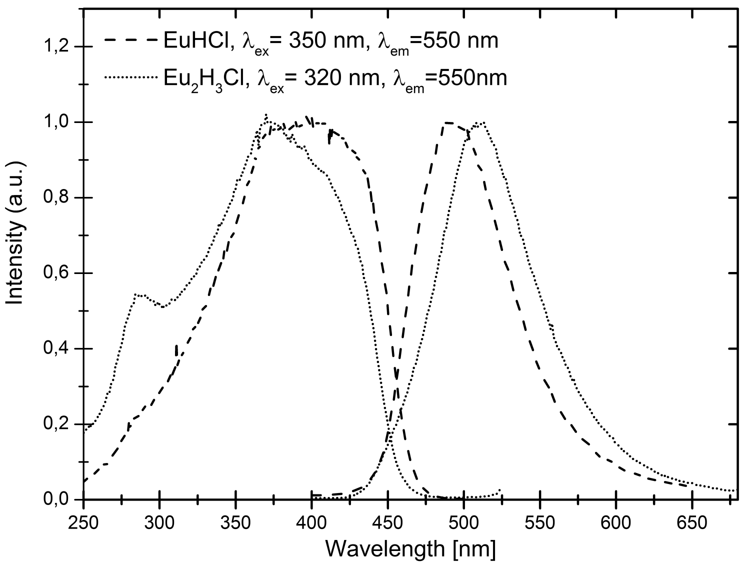

Figure 98: Luminescence excitation and emission spectrum (FL920) of the phase mixture of the sample “Eu_2H_3Cl” as shown in Fig.94 and “EuHCl” as shown in Fig.97 at 300 K. Emission maxima at 495 and 510 nm. Spectra recorded at FLS920 except emission of “EuHCl”.

Since Eu_4OCl_6 is known to emit at 467 nm[152], the luminescence of the sample EuHCl does not originate from the impurity phase, but the product, even though the presence Eu_4OCl_6 luminescence cannot be completely excluded. The emission of “Eu_2H_3Cl” shifted to longer wavelengths in comparison to the emission band of “EuHCl”. The excitation spectrum of “Eu_2H_3Cl” is shifted to slightly higher energies compared to the excitation spectrum of “EuHCl” and shows an additional minor maximum at 280 nm. Even though one luminescent phase or luminescence center may be present in both phase mixtures, the spectra indicate the presence of other, different luminescence centers. It is unclear if the luminescence emission is only related to the main phase or caused by impurity phases. However, the observation of a bright and apparently homogeneous emission suggests that the main phase in both samples, EuHCl, causes at least a part of the luminescence emission.

Temperature-dependent decay curves are shown in Fig. 99. Due to technical problems decay curves were only recorded from RT to 100 K. In this temperature range a significant increase in the lifetimes and therefore also the emission intensities is observed.

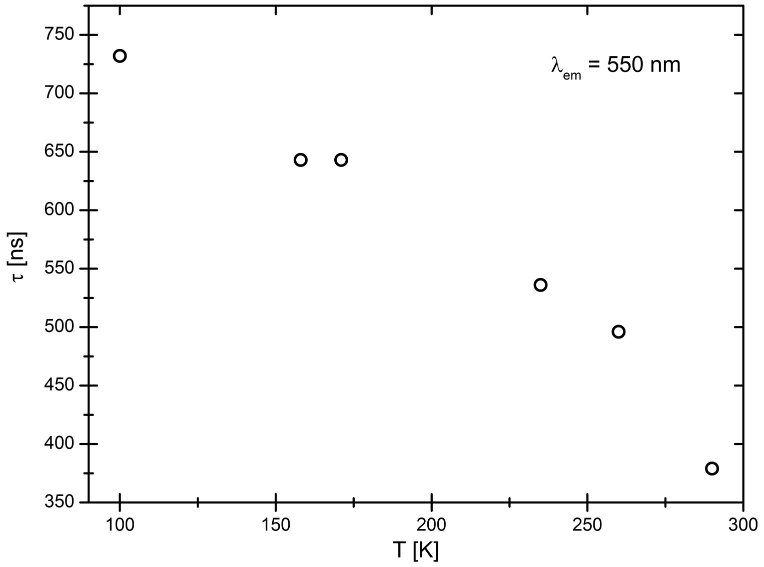

Figure 99: Temperature dependence of the lifetimes of “EuHCl”.

4.6 Comparison of the emission energies of the $4f^6 5d$ states of Eu(II) in different host lattices and coordination environments of Eu(II)

Emission energies as well as coordination numbers and interatomic distances of pure hydride host lattices are listed in Table 23 and of hydride-fluorides and hydride-chlorides in Table 24.

Table 23: Comparison of the emission energies of the $4f^6 5d$ states of Eu(II) in different hydride host lattices and coordination environments of Eu(II) studied within this work. The assumed occupation site is given in brackets.

Compound	Emission onset (nm)	Emission max. (nm)	Coordination nr. and polyeder	Eu-anion (pm) (av. (pm))
$SrMgH_4$ (Sr site)	446	517	distorted tricapped trigonal prism (CN 9)	244-280 (261)
$LiBaD_3$ (Ba site)	483	528	cuboctahedron (CN 12)	283.7
$LiBaH_3$ (Ba site)	485	530	cuboctahedron (CN 12)	284.5
$LiSrD_3$ (Sr site)	528	575	cuboctahedron (CN 12)	270.5
$LiSrH_3$ (Sr site)	530	565	cuboctahedron (CN 12)	271.2
$KMgH_3$ (K site)	538	565	ocuboctahedron (CN 12)	284.9
$NaMgH_3$ (Na site)	580	700	dicapped distorted cube (CN 10)	227.5-300.4 (263.7)
SrH_2	637	728	distorted tricapped trigonal prism (CN 9)	243-284 (260)
BaH_2	603	755	distorted tricapped trigonal prism (CN 9)	254-296 (279)
CaH_2	670	765	distorted tricapped trigonal prism (CN 9)	205-270 (234)

Potential local lattice distortions caused by europium doping as well as the potential occupation of interstitial sites are ignored. Interatomic distances are given for doping concentrations ≤ 1 mol%. As doping concentrations may vary slightly, interatomic distances are approximate. In case of $SrMgH_4$, $SrF_{1.5}H_{0.5}$, $EuF_{2-x}H_x$ and EuHCl, the emission onsets were determined at RT for lack of low temperature data and might therefore be inaccurate. Since the lattice parameter a in EuH_xF_{2-x} does not show a significant change with varying x for the studied range of x, a and therefore also the interatomic distances are assumed to be constant.

Table 24: Comparison of the emission energies of the $4f^65d$ states of Eu(II) in different hydride-fluoride or hydride-chloride host lattices and coordination environments of Eu(II) studied within this work. The assumed occupation site is given in brackets.

Compound	Emission onset (nm)	Emission max. (nm)	Coordination nr. and polyeder	Eu-anion (pm) (av. (pm))
EuHCl ("EuHCl´´)/	421/	491/	capped quadratic	248 (H), 305-310 (Cl)
("Eu_2H_3Cl´´)	425	510	antiprism (CN 9)	(280)
$KMgHF_2$	unknown	505	cuboctahedron (CN 12)	282.3
$LiBaHF_2$	455	515	cuboctahedron (CN 12)	282.6, 284.1
$EuH_{0.2}F_{1.8}$	455	570 (685)	cube (CN 8)	253
$EuH_{0.25}F_{1.75}$	460	595 (685)	cube (CN 8)	253
$EuH_{0.28}F_{1.72}$	463	605 (685)	cube (CN 8)	253
$EuH_{0.33}F_{1.67}$	464	605 (685)	cube (CN 8)	253
$EuH_{0.4}F_{1.6}$	468	605 (685)	cube (CN 8)	253
$EuH_{0.5}F_{1.5}$	478	636 (685)	cube (CN 8)	253
$EuH_{0.67}F_{1.33}$	534	685	cube (CN 8)	253
$SrH_{0.5}F_{1.5}$	539	583	cube (CN 8)	252

Those data show that in case of pure hydride host lattices the decrease in the interatomic Eu-ligand distance leads to a shift to longer wavelengths. Exceptions are $SrMgH_4$ which shows a much shorter wavelength than expected based on the interatomic distances for Eu on the Sr-site and BaH_2 and $KMgH_3$. However, as mentioned in Sect.4.3.1, it is not clear on which lattice site Sr is located in $SrMgH_4$. An explanation for the unexpected emission wavelength might be that Sr is located on an interstitial. The long wavelength for BaH_2 can be explained by anomalous emission caused by the smaller size of Eu(II) compared to Ba(II) as discussed in Sect.4.1.4. The emission wavelength in $KMgH_3$ is also slightly longer than expected based on the comparison of interatomic distances. However, in $KMgH_3$ Eu(II) is presumed to occupy a monovalent lattice site, whereas for all the other studied lattices except $NaMgH_3$, Eu(II) is supposedly located on a divalent lattice site. The need for charge compensation might then lead to local distortions which are not considered here. Such local distortions might also be the reason for the extremely long wavelength and the low quenching temperature found for $NaMgH_3$.

In contrast to pure hydridic lattices, the hydride fluoride ratio in hydride-fluorides plays a much greater role in the emission wavelength shifts than slight changes in interatomic distances. It is clear that an increase in the fluoride content always leads to a strong blueshift of the emission. For $KMgHF_2$, for instance, the maximum is shifted about 60 nm to shorter wavelengths compared to $KMgH_3$.

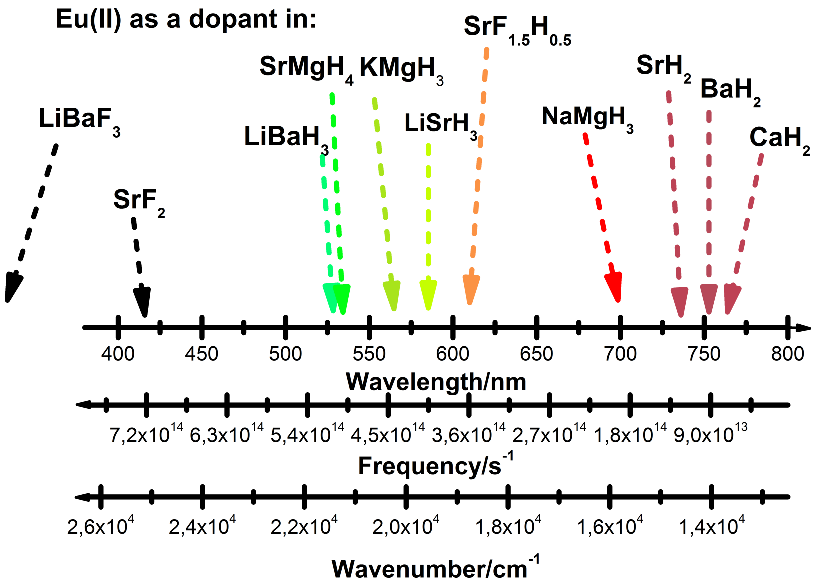

Figure 100: Schematic comparison of the emission wavelengths of Eu(II) in selected compounds.

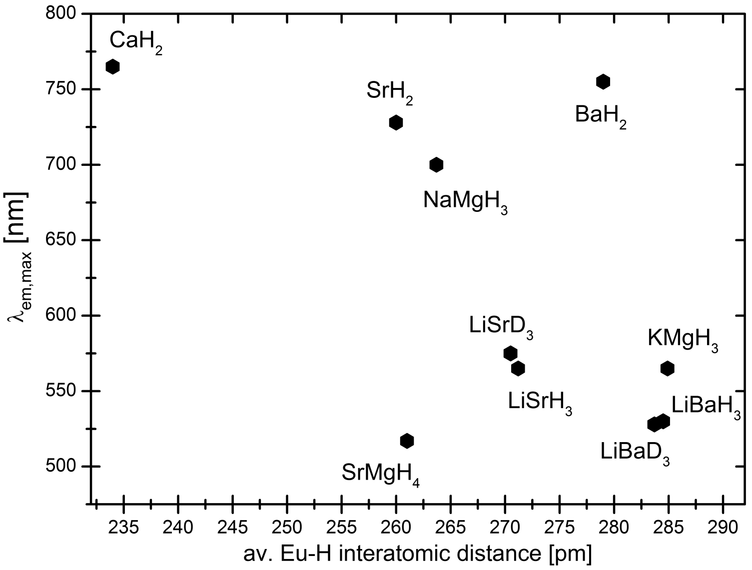

Figure 101: Relation of the emission wavelength maximum of Eu(II) and the average interatomic Eu-H distances in metal hydrides.

4.7 Host lattices containing other activator ions

4.7.1 $Ca_4Mg_3H_{14}$:Ce

Pure $Ce_xCa_{4-x}Mg_3H_{14}$ from $Ce_xCa_{1-x}H_2$ and Mg powder under hydrogen pressure could not be obtained (480°C, 100-100 bar, reaction times of 5-7 days). Annealing the samples for several days yielded only small amounts (max. 20%) of the desired phase and large amounts of CaH_2 and MgH_2. Samples did not show luminescence visible with the naked eye.

4.7.2 $LiSrH_3$:Sm

$LiSrH_3$:Sm (0.5 mol%) was obtained through hydrogenation of the corresponding alloy at about 300°C and approx. 80 bar for 4 days as a white powder. Small amounts of SrH_2 were present. The refinement of the lattice constants of $LiSrH_3$:Sm (0.5 mol%), space group $Pm\bar{3}m$ from X-ray data collected on the *X'Pert Pro* diffractometer yielded 383.658(7) pm. Luminescence measurements on the FL9-20 showed that the weak yellow emission originates from europium contamination rather than from Sm(II) emission. ICP-MS analysis[136] yielded a europium content of 0.25 ppm of the strontium metal used for synthesis. Hydrogenation of the alloys might, however, be inappropriate due to the much higher melting temperature of Sm compared to Sr.

4.7.3 $LiMH_3$:Yb (M = Sr, Ba)

$LiMH_3$: (0.5 mol%) (M = Sr, Ba) were obtained through hydrogenation of the corresponding alloys at about 300°C and approx. 80 bar for 4 days as white powders. Refinement of the crystal structure yielded a lattice constant of 402.392(5) for M = Ba and 383.73(1) (pm) for M = Sr. Due to europium contamination of the strontium metal, the sample with M = Sr showed a very weak yellow emission, whereas the barium sample did not show any emission.

4.7.4 CaH_2:Yb

CaH_2:Yb was obtained as a purple powder through hydrogenation of the corresponding alloy at 85 bar and 300°C for 3 days and does not show does not exhibit any visible luminescence. Possibly, this is due to impurities such as trivalent ytterbium, which might be removed by a different thermal treatment. However, observation of the luminescence of divalent ytterbium is rather difficult and requires a sufficiently large band gaps, because the first df transition is parity-forbidden.

4.7.5 MH_2:Mn (M = Ca, Ba)

Samples with divalent manganese could not be obtained by melting manganese with barium or calcium and hydrogenation of the alloy. After hydrogenation (300°C, 80-100 bar, reaction times 3-4 days) samples contained the binary hydride and fine manganese powder.

4.8 YbH_x

In the system YbH_x compounds with x up to 2.67 are known to be metastable at atmospheric pressure and room temperature[26]. As mentioned in Sect.2.2, the existence and structure of YbH_{2+x} with $0.04 \leq x \leq 0.74$ has been controversially discussed. It would therefore be interesting to clarify the existence and hydrogen content of such compounds and to investigate if a compound with x larger than 2.67 is existing at high pressures using *in situ* methods.

4.8.1 Synthesis via DSC

Hydrogenation of ytterbium pieces at 15 bar hydrogen pressure and maximal 450°C using the DSC yielded a black and white powder. X-ray data indicate the presence of YbH_2 and at least another unknown phase. Due to the presence of these unknown reflections, X-ray data were not refined via Rietveld.

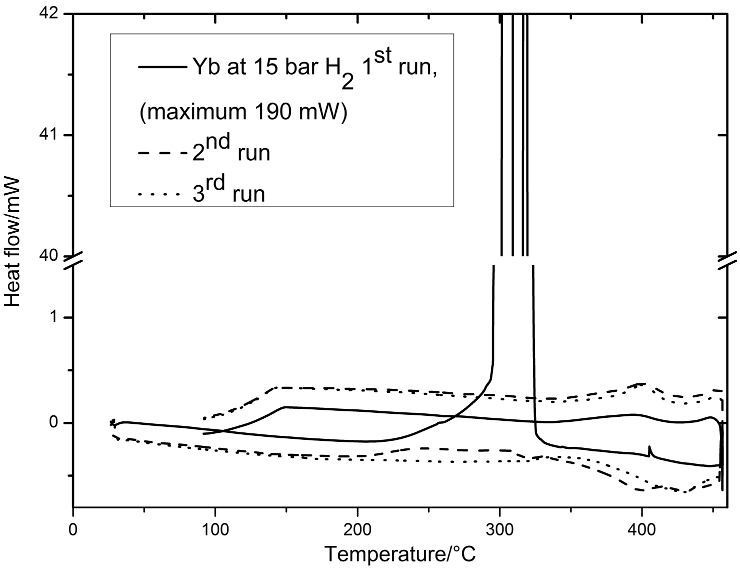

Figure 102: Heat flow - temperature diagram of Yb at 15 bar hydrogen pressure. Positive signals are exothermal.

4.8.2 Synthesis via autoclave

Hydrogenation of ytterbium pieces at 80 bar hydrogen pressure and 300°C in an autoclave for 2-3 days yielded a black powder whose structure was refined from X-ray powder diffraction data according to the structure data of Auffermann[26] with a trigonal metric, P$\bar{3}$1m, a = 635.3(1) pm, c = 897.5(3) pm.

DSC measurements of these samples at hydrogen pressures from 35-50 bar showed a reversible signal at about 350°C (see Fig. 103) indicating a hydrogen uptake or phase transition.

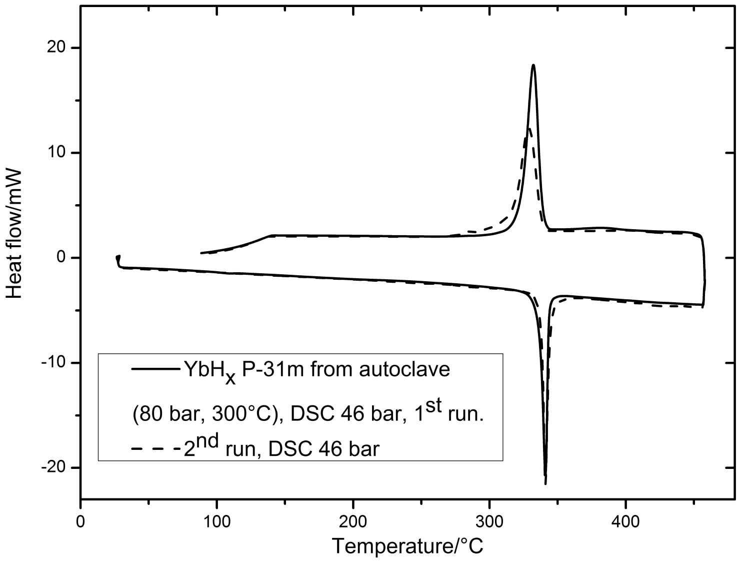

Figure 103: Heat flow - temperature diagram of pure YbH$_x$ (P$\bar{3}$1m, synthesized at 80bar and 300°C in an autoclave) at 46 bar hydrogen pressure. Positive signals are exothermal.

Therefore, *in-situ* neutron powder diffractions experiments were carried out as described in the following.

4.8.3 Neutron powder diffraction

In order to clarify if the phase transition observed in the DSC (see Fig.103) is due to a hydrogen uptake or a phase transition and if an ytterbium hydride with a higher hydrogen content than 2.67 exists, black YbD$_{2+x}$ obtained via hydrogenation of Yb in an autoclave was studied in a single crystal sapphire cell at high deuterium pressure and high temperatures at the D20/ILL (wavelength approx. 186.7 pm, might differ slightly in the different experiments).

Temperatures given in the *in-situ* plots (Fig.104) are approximate temperatures as given by the calibration curve of the pyrometer obtained for Pd. Even though both the silicon powder used for temperature calibration and the YbD_{2+x} are of black color, the temperature calibration curve of the pyrometer using silicon could not be applied, since it is only valid up to 400°C and cannot be extrapolated for higher temperatures due to the non-linear form of the calibration curve. It is not clear if the alternative calibration curve obtained for Pd is suited, since the metallic appearance of Pd powder cannot be compared to the black YbD_{2+x}. Furthermore, the calibration curve is only valid for temperatures up to 400°C, so that an extrapolation for higher temperatures has to be carried out. However, since the phase transition is observed at approx. 340°C in the DSC and at 400°C (measured via pyrometer without calibration curve) in the *in-situ* neutron powder diffraction experiments, which corresponds to 338°C according to the calibration curve for Pd, the calibration curve for Pd is assumed to be suited and will be used in the following. For the determination of the temperature dependence of the lattice constants, both the measured temperatures without calibration curve and the temperatures obtained from the calibration curve for Pd will be used. A detailed list of temperatures and lattices constants is given in the Appendix (8.4).

The experiment was repeated three times. Twice, the formation of a new phase with slightly different reflection positions could be observed at about 350°C and 80 (50) bar deuterium pressure. An example for an *in-situ* neutron powder diffraction experiment is shown in Fig. 104; intensities are given in false colors. However, before the reaction was completed a sudden drop of pressure due to a leakage or breaking of the cell occurred and the product decomposed to YbD_2. Once, while heating under an argon atmosphere, the starting material decomposed to YbD_2. Structure refinements of the assumed $YbD_{2.67}$ were carried out using the structure model of Auffermann[26] and an additional *2d* site for deuterium. The structure model can be derived from the BiF_3 structure typ for a hypothetical YbD_3 (Yb in *4a*, D in *4b* and *8c*) via transformation to $P\bar{3}1m$ (see Fig.105). Symmetry reduction starting from the BiF_3 structure type yields two additional deuterium positions compared to the structure model of Auffermann, *1b* and *2d*. The site *1b* is excluded, since it leads to very short deuterium-deuterium distances, whereas *2d* is included. Structure refinement then yielded occupation numbers for *2d* which were significantly different from zero.

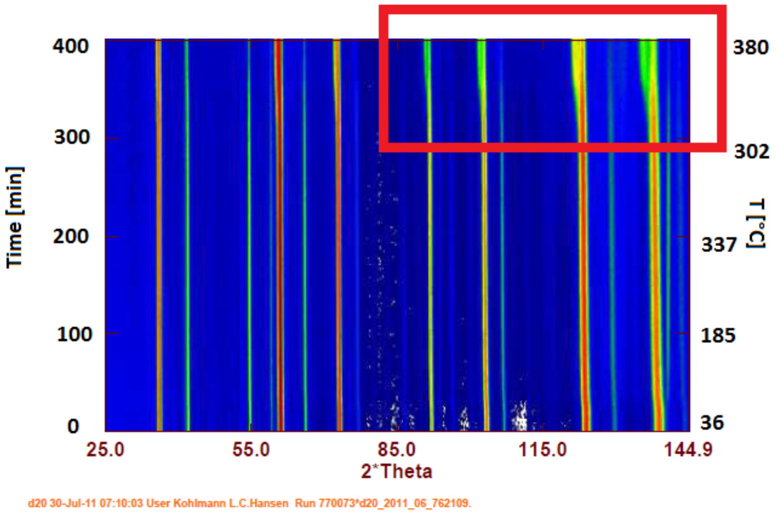

(a) Complete log plot.

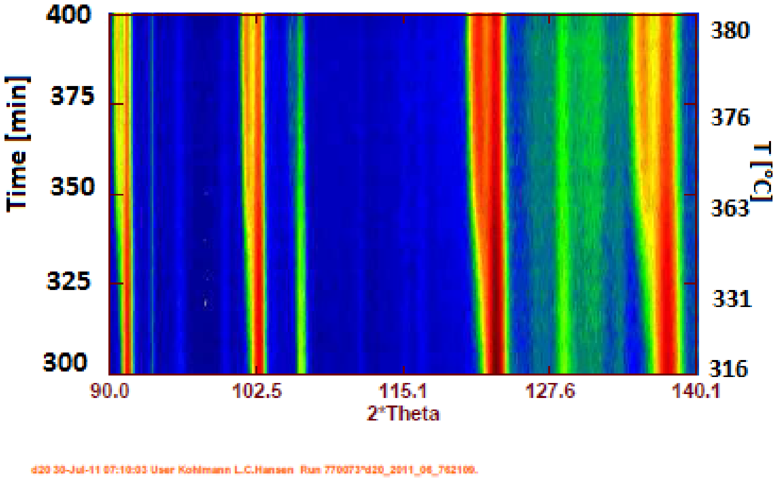

(b) Detail.

Figure 104: In situ neutron powder diffraction with YbD_x at 80 bar deuterium pressure. Complete log plot in false colors from 36 to 380°C (a) and detail from 90 to 140° 2θ and 316 to 380°C (b). Temperatures were obtained from the calibration curve for Pd.

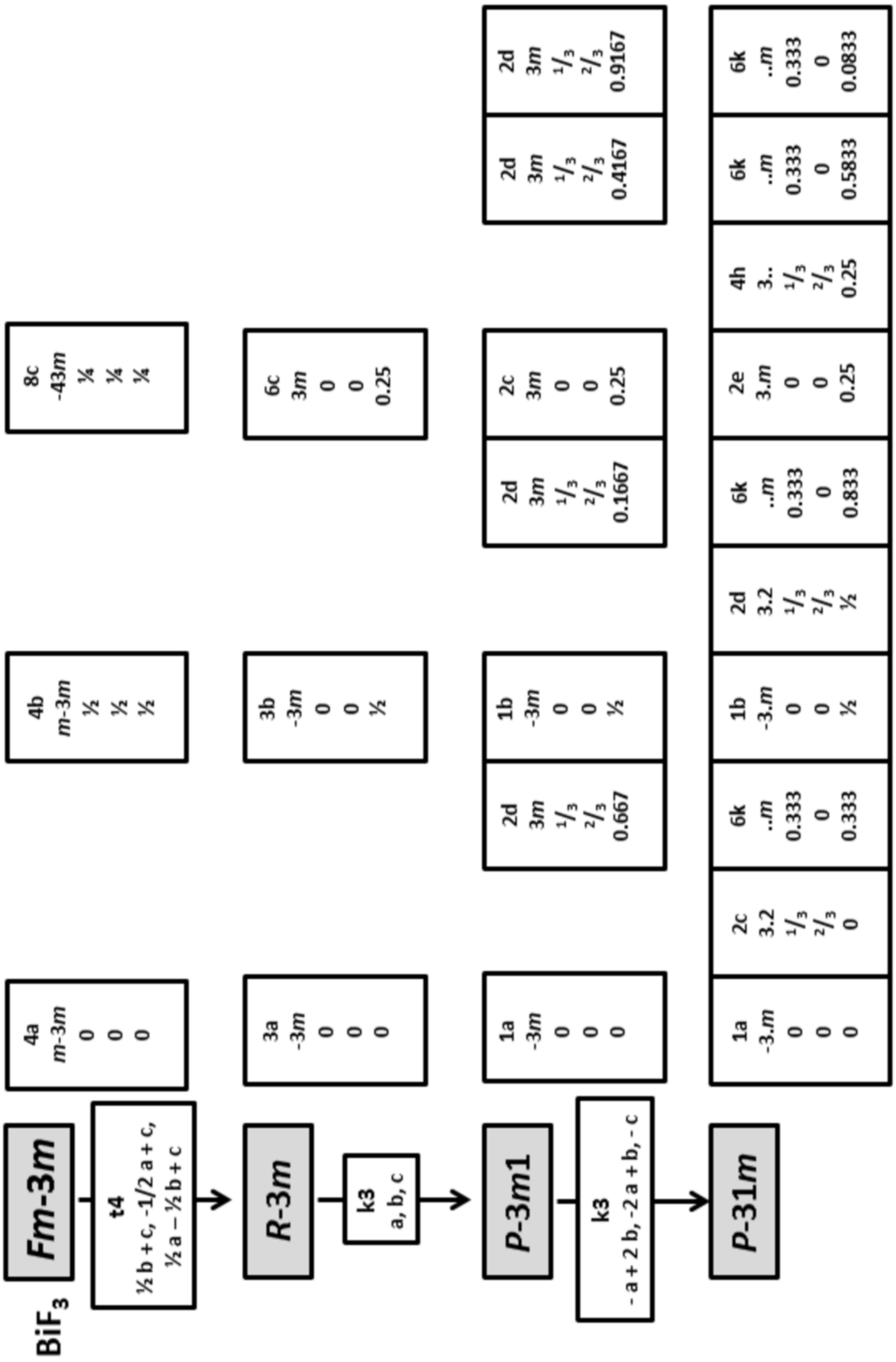

Figure 105: Symmetry relation between SG 225 and 162.

No refinement of the positions, but only of the deuterium occupation numbers was carried out, structural data are given in the Appendix (8.4). The refined structure at RT (YbD_{2+x} phase I) is shown in Fig. 108; it consists of a slightly distorted closest packing of metal atoms with a partial deuterium occupation in octahedral and tetrahedral voids.

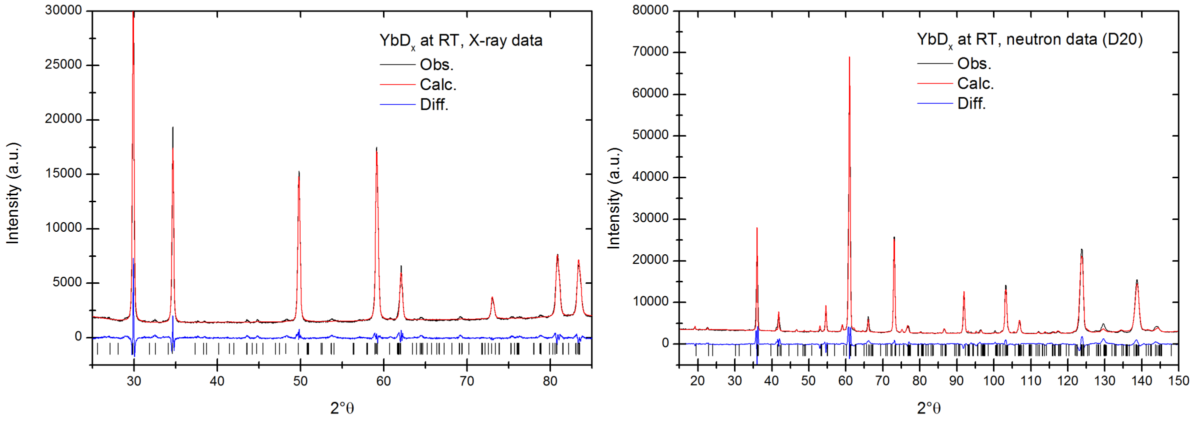

Figure 106: Rietveld refinement of the structure of YbD$_x$ at RT and atmospheric pressure. Co-refinement of X-ray (see left side) and neutron (see right side) data in the space group 162, structural data according to[26] and additional *2d* site. a = 633.49(1) pm, c = 898.71(3) pm.

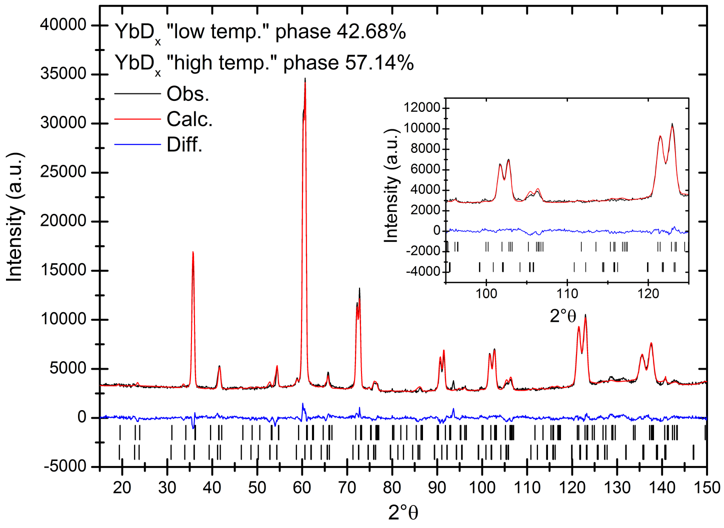

Figure 107: Rietveld refinement of the structure of the two YbD$_x$ phases at 380°C and 80 bar. Bragg markers on top: “low” temperature phase (I), Bragg markers at bottom: “high” temperature phase (II). P$\bar{3}$1m, structural data according to[26] and additional *2d* site; I: a = 635.92(3) pm, c = 902.2(1) pm; II: a = 640.7(1) pm, c = 906.9(4) pm.

At elevated temperatures, beside the phase mentioned above, reflections belonging to slightly larger d-values, which seemed to originated from a similar structure with slightly larger lattice parameters, appeared (see Fig.107). As the reaction was not completed, structure refinement was carried out for data with both phases present, thus making a correct refinement of deuterium positions and occupancies difficult. Therefore, only occupancies and no positions were refined.

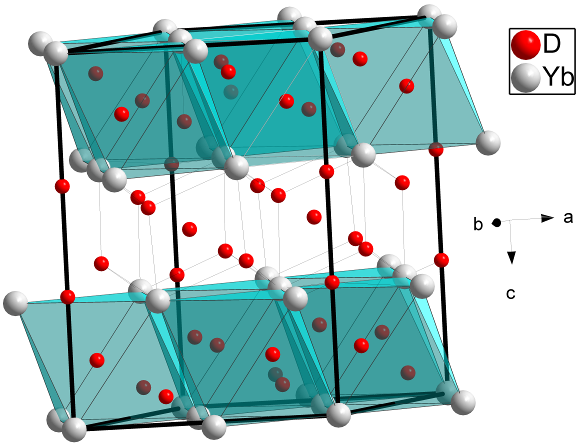

Figure 108: Structure of YbD_x phase I at RT obtained via refinement according to[26] and additional *2d* site. Distorted ytterbium octahedra with central deuterium atoms are depicted.

The approximate temperature dependence of the ratio of phase I and II is shown in Fig. 109.

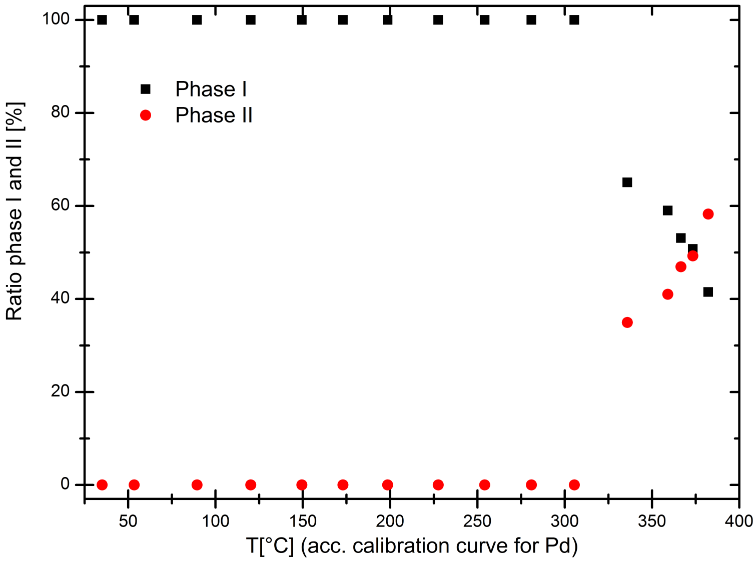

Figure 109: Temperature dependent ratio of phase I and II.

Since the splitting of the reflections is first observed at 336°C, the temperature dependence of the ratio of both phases shows a discontinuity. Below 336°C refinement was carried out using only phase I, whereas above 336°C both phases were considered. Data for higher temperatures for the displayed experiment are not available due to a sudden loss of pressure. Furthermore, approximate temperature dependence of lattice parameters and volumes are depicted in Fig.110-112. Refinement of the occupation number yielded a molecular formula of $YbD_{2.25}$ for the RT phase and at 382°C $YbD_{2.44}$ for phase I and $YbD_{2.07}$ for phase II.

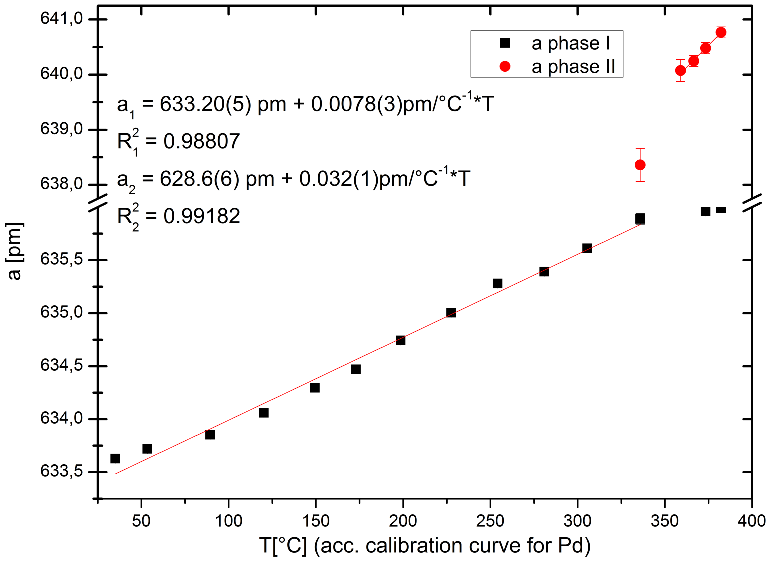

Figure 110: Temperature dependence of lattice parameter a of phase I and II.

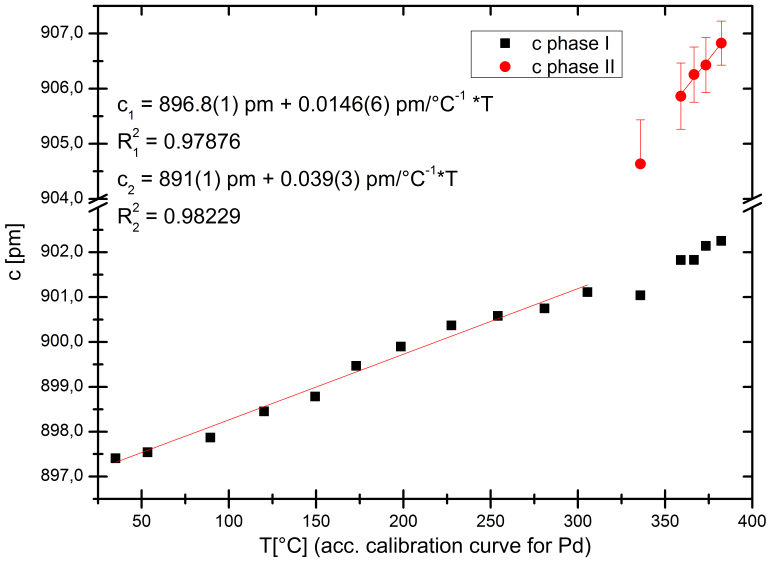

Figure 111: Temperature dependence of lattice parameter c of phase I and II.

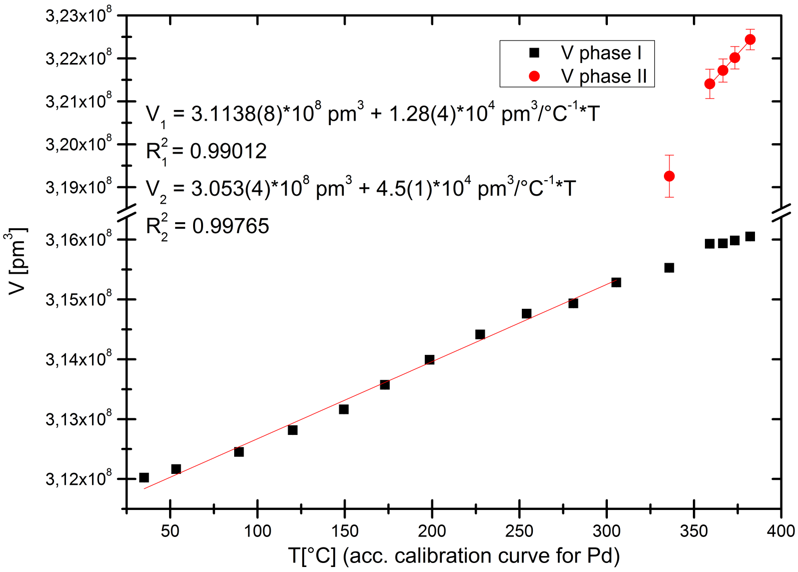

Figure 112: Temperature dependence of the cell volume V of phase I and II.

The shortest Yb - D interatomic distance for phase I at RT is 190.5 pm for Yb2 - D4, all other Yb-D distances vary between 215 and 290 pm. The shortest D-D interatomic distance is 211.9 pm and the shortest Yb-Yb distance 362.8 pm. Since the position were fixed, the interatomic distances of phase I and II at higher temperatures increase slightly due expansion of the lattice. For a complete list of interatomic distances see Appendix, Table 50. For comparison, the shortest interatomic distances between Yb - F, F - F and Yb - Yb are 233 pm, 252 pm and > 400 pm for the hexagonal modification of YbF_3[156] and 204 pm, 246 pm and 355 pm for the orthorhombic modification[157]. Furthermore, the shortest interatomic distances Yb - D, D - D and Yb - Yb in orthorhombic YbD_2[23] are 238.6 pm, 267 pm and 347.9 pm. Thus the shortest interatomic distance Yb - D of YbD_{2+x} is significantly shorter than any known Yb - D or Yb - F distances, all other Yb - D distances are within the range of known values. The shortest D - D distance is also significantly shorter than D - D or F- F distances of the other compounds, however, assuming an overall oxidation state of almost III for Yb, one might presume that the absolute value of the charge of hydride or deuteride is significantly smaller than 1. The Yb - Yb distances lie within the range of known values.

Coefficients of linear expansion between 35 and 340°C (calibration curve for Pd; values without calibration: 25 - 400°C) for the low temperature phase YbD_{2+x} (phase I) were estimated to be $1.23(3) \cdot 10^{-5}$ °C^{-1} ($1.01(1) \cdot 10^{-5}$ °C^{-1}) for a and $1.63(6) \cdot 10^{-5}$ °C^{-1} ($1.35(6) \cdot 10^{-5}$ °C^{-1}) for c, which are slightly larger than those found in similar compounds ($8 \cdot 10^{-6}$ °C^{-1})[158]. It is not clear if the expansion is only due to thermal behavior or if a deuterium uptake occurs. For the high-temperature phase (phase II), coefficients of linear expansion between 340 and 380°C (400 - 461°C) were estimated to be $5.0(1) \cdot 10^{-5}$ °C^{-1} ($3.2(1) \cdot 10^{-5}$ °C^{-1}) for a and $4.3(3) \cdot 10^{-5}$ °C^{-1} ($2.9(2) \cdot 10^{-5}$ °C^{-1}) for c. However, it should be noted that these values for higher temperatures cannot be compared with the literature values obtained for temperatures between 25 and 125°C. Furthermore, the behavior of the lattice constants above 336°C, especially of phase I, is not linear, which might be due to difficulties refining both phases at the same time.

For phase I, an increase of the occupation numbers of the deuterium sites *2d* and *6k* (0.332 0 0.582; 0.353 0 0.0717; 0.2383 0 0.8293), but also a decrease in *2e* and *4h* is observed (for structural data see Appendix 8.4). However, the refinement of the occupation numbers at 382°C is hampered by the overlap of reflections of both phases. It is therefore also not clear if the decrease in the deuterium occupation numbers in phase II compared to phase II are reliable or an artefact of the refinement. Further *in-situ* experiments are necessary to prepare a pure sample of phase II which might allow the correct determination of the structure of phase II.

5 Electronic structure calculations - Theoretical background

A given system of nuclei and electrons can be described using the stationary Schrödinger-equation[159]:

$$\hat{H}\Psi = E\Psi \tag{14}$$

with the wave function Ψ, the *eigenvalue* E and the Hamiltonian $\mathscr{H}$, which is the sum of the kinetic and potential energy. For a system with N nuclei and n electrons, and neglecting relativistic effects, the exact many-particle Hamiltonian is:

$$\begin{aligned}\hat{H} = & -\frac{\hbar^2}{2}\sum_i^N \frac{\nabla^2_{\vec{R}_i}}{M_i} - \frac{\hbar^2}{2}\sum_i^n \frac{\nabla^2_{\vec{r}_i}}{m_e} \\ & - \frac{1}{4\pi\varepsilon_0}\sum_i^N\sum_j^n \frac{e^2 Z_i}{|\vec{R}_i - \vec{r}_j|} + \frac{1}{8\pi\varepsilon_0}\sum_{i\neq j}^n \frac{e^2}{|\vec{r}_i - \vec{r}_j|} + \frac{1}{8\pi\varepsilon_0}\sum_{i\neq j}^N \frac{e^2 Z_i Z_j}{|\vec{R}_i - \vec{R}_j|}\end{aligned} \tag{15}$$

with M_i mass of a nucleus in $\vec{R}_i$, m_e mass of an electron located at $\vec{r}_i$ and

$$\nabla^2 = \frac{\delta^2}{\delta x^2} + \frac{\delta^2}{\delta y^2} + \frac{\delta^2}{\delta z^2} \tag{16}$$

The first two terms are the kinetic energy operators for the nuclei and the electrons. The remaining three terms originate from the Coulomb interactions between electrons and nuclei (Coulomb attraction) and among the electrons as well as the nuclei (repulsion)[160].

Since it is impossible to solve Equation 15 exactly, firstly approximations need to be introduced. Due to the fact that the nuclei are much heavier than the electrons, they also move much slower than the electrons. Therefore they can be regarded as frozen and the electrons are assumed to be in instantaneous equilibrium with the nuclei. This approach is called the Born-Oppenheimer approximation and allows the removal of the nuclear coordinates. The Hamiltonian for the electrons now becomes

$$\hat{H}_e = -\frac{\hbar^2}{2}\sum_i^n \frac{\nabla^2_{\vec{r}_i}}{m_e} - \frac{1}{4\pi\varepsilon_0}\sum_i^N\sum_j^n \frac{e^2 Z_i}{|\vec{R}_i - \vec{r}_j|} + \frac{1}{8\pi\varepsilon_0}\sum_{i\neq j}^n \frac{e^2}{|\vec{r}_i - \vec{r}_j|} \tag{17}$$

or

$$\hat{H}_e = \hat{T} + \hat{V} + \hat{V}_{ext} \tag{18}$$

with the kinetic energy of the electron gas $\hat{T}$, the potential energy due to electron-electron interactions $\hat{V}$ and the potential energy of the electrons in the external field of the nuclei $\hat{V}_{ext}$. To solve Equation 18 several approximated methods have been developed[161], among them, for instance, the Hartree-Fock method.

5.1 DFT

An alternative approach to evaluate the ground state properties is the density functional theory (DFT), which is based upon the two theorems of Hohenberg and Kohn[162]. According to Hohenberg and Kohn, the total energy of a system of interacting electrons within an external potential, or any ground-state property, is given as a functional of the exact ground-state electron density ρ[161,163]. However, for many properties so far only approximations and no exact functionals have been derived.

$$E = E[(\rho)] \tag{19}$$

Furthermore, the ground-state total energy functional is of the following form

$$\begin{aligned} E_{V_{ext}}[\rho] &= \langle \Psi \mid \hat{T} + \hat{V} | \Psi \rangle + \langle \Psi \mid \hat{V}_{ext} \mid \Psi \rangle && (20) \\ &= F_{HK}[\rho] + \int \rho(\vec{r}) V_{ext}(\vec{r}) d\vec{r} && (21) \end{aligned}$$

with a universal function F. Thus the ground-state total energy can be obtained from the electron density ρ for an external potential V$_{ext}$ and moreover, according to the second theorem of Hohenberg and Kohn, it is possible to evaluate the ground-state density using a variational principle. In accordance with Kohn and Sham[164], the so-called Kohn-Sham Hamiltonian for particles of a model system, which has the same density and total energy as a real system and is exposed to the potential of the nuclei and a potential caused by exchange and correlation effects is given by:

$$\begin{aligned} \hat{H}_{KS} &= -\frac{\hbar^2}{2m_e}\vec{\nabla}_i^2 + \frac{e^2}{4\pi\varepsilon_0}\int \frac{\rho(\vec{r}\,')}{|\vec{r} - \vec{r}\,'|} d\,\vec{r}\,' + V_{xc} + V_{ext} \\ &= \hat{T}_0 + \hat{V}_H + \hat{V}_{xc} + V_{ext} && (22) \end{aligned}$$

where the exchange correlation potential is

$$\hat{V}_{xc} = \frac{\delta V_{xc}[\rho]}{\delta \rho} \tag{23}$$

Now the ground-state electron density of a n-electron system can be formulated as follows:

$$\rho(\vec{r}) = \sum_{i=1}^{n} \Phi_i(\vec{r})^* \Phi_i(\vec{r}) \tag{24}$$

with the single-particle wave functions $\Phi_i(\vec{r})$ being the n lowest-energy solutions of the Kohn-Sham equation.

$$\hat{H}_{KS}\Phi_i = \varepsilon_i \Phi_i \tag{25}$$

The Hartree operator V_H, as well as the exchange-correlation operator V_{xc}, depend on the density ρ, which again depends on the Φ_i, which are being sought for. Therefore the problem that needs to be dealt with is a self-consistent one and can be solved through an iterative procedure. A starting density needs to be guessed to construct a Hamiltonian and to solve the *eigenvalue* problem. From this solution a new density, which will probably differ from the first one, is derived. The procedure will be performed until a convergence of the density is achieved. So far the method is exact apart from the Born-Oppenheimer approximation. However, the exchange correlation is unknown and thus needs to be approximated[160].

A method of approximating the exchange correlation is the Local Density Approximation (LDA), which approximates E_{xc}^{LDA} via an exchange correlation energy per particle $\varepsilon(\rho(\vec{r}))$ of a homogeneous electron gas with the density ρ that can be exactly determined numerically. Here the material is divided in infinitesimally small volumes with constant density, which contribute to the total exchange correlation energy by an amount equal to the exchange correlation energy of an identic volume filled with a homogeneous electron gas with the density ρ.

$$E_{xc}^{LDA} = \int \rho(\vec{r})\varepsilon(\rho(\vec{r}))d\vec{r} \tag{26}$$

The Local Density Approximation is rather crude and often fails in accurately describing chemical bonding. An improvement of the LDA is the assumption that the exchange correlation contribution of each infinitesimal volume is not only depend on the local density of that volume, but as well on the density of the neighboring volumes, thus on the gradient of the density. The most popular of those so-called gradient-corrected functionals is called the *Generalized Gradient Approximation* (GGA)[165] that describes the exchange-correlation energy as follows:

$$E_{xc}^{GGA} = \int \rho(\vec{r})F\left\{\rho(\vec{r}), |\nabla\rho(\vec{r})|, \nabla^2\rho(\vec{r})\right\}d\vec{r} \tag{27}$$

The GGA yields significantly improved energetic results, in many cases better geometries and a better description of bond breaking and bond formation[159] than the LDA.

5.2 Bloch's theorem

On the first sight, solving the Schrödinger equation for a solid-state material seems impossible. However, exploitation of the translation symmetry of a crystal using the Bloch theorem[159,166] leads to an immense simplification. Due to the translational symmetry of a crystal, the electronic potential possesses the periodicity of the lattice. Thus the potential V for an ideal infinite lattice with a lattice vector T is:

$$V(r+T) = V(r) \tag{28}$$

The simplification neglects impurities, defects as well as vibrations. Bloch's theorem states that for a given crystal orbital $\Psi(k,r)$ and introducing the vector k the translation by a lattice vector T is equivalent to multiplying by a phase factor:

$$\Psi(k,r+T) = e^{ik\frac{T}{\hbar}}\Psi(k,r) \tag{29}$$

Assuming periodic boundary conditions, the values of k can be determined. In the one-dimensional case of a crystal with the length L consisting of a nearly infinite number of unit cells N each possessing the lattice parameter a ($L = N \cdot a$) we obtain:

$$\Psi(k,0) = \Psi(k,L) = e^{ikL}\Psi(k,0) \tag{30}$$

It is only valid for

$$kL = 2\pi n \tag{31}$$

and therefore

$$-\frac{\pi}{a} \leq k \leq \frac{\pi}{a} \tag{32}$$

In three dimensions, this part of the reciprocal space corresponds to the (first) Brillouin zone. The quality of a calculation depends on the number of k-points. Since a small unit cell in real space possesses a large Brillouin zone in reciprocal space and vice versa, a large number of k-points is needed to obtain an accurate description of a small unit cell in real space, whereas for a large cell in real space only a smaller number of k-points is needed.

5.3 Vanderbilt Ultrasoft Pseudopotentials and PAWs

Within the quantum-mechanical part of this work, both Vanderbilt Ultrasoft Pseudopotentials and Projector Augmented Waves (PAWs) were used as potentials in the theoretical calculations carried out with the Vienna ab initio code (VASP)[167,168]. Therefore, a short description of the methods is given in the following. However, the background such as the mathematical approach is beyond the scope of this work and shall therefore not be discussed. The interested reader is referred to[169–173].

5.3.1 Vanderbilt Ultrasoft Pseudopotentials

Since atomic wave functions are required to comply the orthogonality constraint, those of the same angular dependence must contain nodes in the radial dependence of the functions[161]. Those with different angular dependences automatically satisfy the constraint. The parts of the atomic wave functions that are involved in chemical bonding, however, are located outside the region containing radial nodes. Near the core the electrons possess a large kinetic energy leading to a strong oscillation of the wave function. At the same time, due to the large kinetic energy, a change in the chemical environment barely affects the wave function within this region. In contrast, the energy within the binding region is rather small and thus the wave function rather smooth. Using a given basis set, such as plane waves $e^{i\vec{\kappa}\vec{r}}$, leads to difficulties describing the binding region with high accuracy and, at the same time, to take the strong oscillations near the core into account. A possibility to avoid these difficulties would be the substitution of the atomic wave function in the core region with a smoother one that accurately describes the binding region. If the wave function Ψ is now written as a linear combination of a smooth part and a linear combination of the core wave functions,

$$\Psi = \Phi + \sum_c b_c \Psi_c \qquad (33)$$

with the core wave functions Φ_c and an unknown constant b_c is obtained. b_c can be determined using the orthogonality constraint. Multiplying with a core wave function Ψ_{c0}^* and integrating yields[161]

$$
\begin{aligned}
0 \equiv \langle \Psi_{c_0} \,|\, \Psi \rangle &= \langle \Psi_{c_0} \,|\, \Phi \rangle + \sum_c b_c \langle \Psi_{c_0} \,|\, \Psi_c \rangle \\
&= \langle \Psi_{c_0} \,|\, \Psi \rangle + b_{c_0} \qquad (34)
\end{aligned}
$$

and therefore

$$
b_{c_0} = -\langle \Psi_{c_0} \,|\, \Psi \rangle \qquad (35)
$$

Inserting Equation 33 into the single-particle equation

$$
\hat{h}\Psi = \varepsilon\Psi \qquad (36)
$$

yields

$$
\begin{aligned}
\hat{h}\left[\Phi(\vec{r}) + \sum_c b_c \Psi_c\right] &= \varepsilon\left[\Phi(\vec{r}) + \sum_c b_c \Psi_c\right] \\
\Leftrightarrow \hat{h}\Phi(\vec{r}) + \sum_c b_c \hat{h}\Psi_c(\vec{r}) &= \varepsilon\Phi(\vec{r}) + \sum_c b_c \varepsilon \Psi_c(\vec{r}) \\
\Leftrightarrow \hat{h}\Phi(\vec{r}) - \sum_c \int \Psi_c^*(\vec{r}_1)\Phi(\vec{r}_1)d(\vec{r}_1)\varepsilon_c\Psi_c(\vec{r}) &= \varepsilon\Phi(\vec{r}) - \sum_c \int \Psi_c^*(\vec{r}_1)\Phi(\vec{r}_1)d(\vec{r}_1)\varepsilon\Psi_c(\vec{r}) \qquad (37) \\
\Leftrightarrow \hat{h}\Phi(\vec{r}) + \sum_c (\varepsilon - \varepsilon_c) \int \Psi_c^*(\vec{r}_1)\Phi(\vec{r}_1)d(\vec{r}_1)\Psi_c(\vec{r}) &= \varepsilon\Phi(\vec{r}) \qquad (38)
\end{aligned}
$$

Writing the single particle operator $\hat{h}$ as a kinetic-energy operator plus $\hat{V}_{ps}$ containing everything except the kinetic-energy part, such as the external potential from the nuclei, the Coulomb potential and the exchange-correlation in DFT, for instance, and the non-local operator

$$
\sum_c (\varepsilon - \varepsilon_c) \int \Psi_c^*(\vec{r}_1)\hat{P_{12}}\Phi(\vec{r}_1)d(\vec{r}_1) \qquad (39)
$$

with the permutation operator $\hat{P}_{12}$ yields

$$
\left[-\frac{1}{2}\nabla^2 + \hat{V_{ps}}(\vec{r})\right]\Phi(\vec{r}) = \varepsilon\Phi(\vec{r}) \qquad (40)
$$

$\hat{V}_{ps}$ is complicated and often approximated using $V_{ps}(\vec{r})$, the so-called pseudopotential. The use of psuedopotentials leads to a loss of information regarding the charge density and wave function near the core, but allows the use of a rather small basis set of plane waves and therefore comparatively short calculations times.

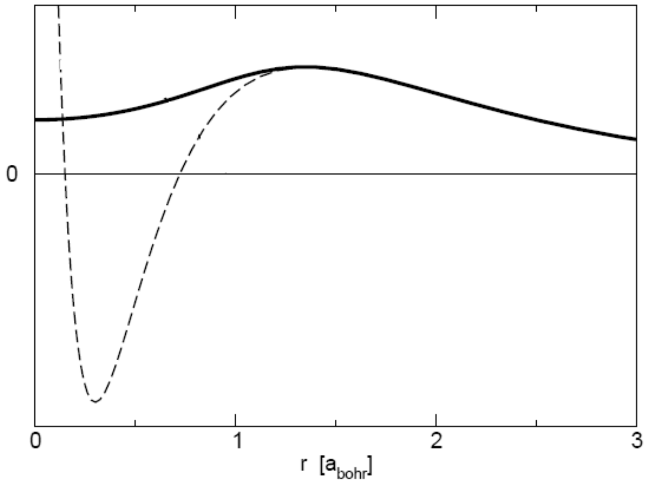

Figure 113: Radial part of the 3s function of Si. The full curve shows the smooth function and the dashed one the true function. Modified, after[173].

Pseudopotentials can be characterized by their softness and transferability. The softer the potential, the fewer planes waves are needed for evaluation. At the same time the reduction of the number of plane waves leads to the need to adjust the potential to the chemical environment, possibly causing problems concerning the transferability. A given pseudopotential is then often only suited for a certain type of system, e.g. a certain oxidation state, and may give wrong results if it is transferred to another system. The size of the basis set is determined by the cut-off energy. It defines the energy up to which plane waves are used.

$$E_{\text{cut-off}} = \frac{\hbar}{2m_e}|\vec{\kappa}_{\text{cut-off}}|^2 \tag{41}$$

5.3.2 PAWs

The Projector Augmented Waves method (PAW) was developed by Blöchl[172], closing the gap between *Augmented Waves* methods and *Plane Wave* pseudopotentials.

As mentioned above, wave functions of real systems exhibit a different behavior in the core and the binding region. The *Projector Augmented Waves* method solves the wave function for both regions separately, expressing the smooth part of the wave functions with the help of plane waves, whereas the part localized in the core region is calculated numerically. All-electron wave functions and all-electron potentials are used. The method is based on a transformation mapping the exact wave functions onto auxiliary functions which are easier to determine[173]. As auxiliary functions, such featuring a fast converging expansion of plane waves are used.

5.4 Bader charge analysis

The Bader charge analysis is one of different methods trying to answer the question if a molecule can be divided into subsystems so that the properties of a system can be described in terms of charge transfer[174,175], or, as formulated by Bader himself, *are there atoms in molecules?* From quantum mechanical calculations a charge density for a single configuration of the nuclei is obtained, whereas X-ray or electron diffraction experiments of solids give the charge density averaged over the thermal motion of the nuclei[174]. In principle, this charge density can provide different types of information about the properties of materials, such as the charge transfer between atoms or the presence of ionic charges. It is, however, unclear how the information can be extracted from the results of theoretical calculations. The question arises how electrons should be partitioned within the system. The charge density is equivalent to a scalar field defined over a three-dimensional space and therefore Bader proposed to summarize its topological properties using the number and kind of its special points. Special points are defined as such points where the charge density shows maxima, minima or saddle points and thus they can be found with the help of the first derivative that becomes equal to zero at such points. For instance, due to their attractive force caused by the nuclear charge, the nuclei exhibit local maxima in the charge density. According to Bader, special points are identified using the first derivative and subsequently, the value of the second derivative will be consulted in order to determine if a special point is a minimum, maximum or saddle point of the charge density. Generally speaking, the nine second derivatives at a point in space, which is called the Hessian matrix of the charge density, form a matrix and can be diagonalized. A critical point can be described using its rank and signature, which are defined by the number of non-zero *eigenvalues* and the algebraic sum of the signs of the *eigenvalues*. Gradient paths starting at arbitrary points, calculating the change in charge density ($\Delta\rho(r_0)$), moving a distance Δr and repeating this procedure are constructed. The so constructed trajectories are perpendicular to contour lines of the charge density and must originate or terminate at a critical point. Space is divided by means of surfaces running through minima in charge density. The Bader charge allocation method used in the following is a grid-based algorithm defining a path of steepest ascent for each grid point[175–177].

6 Electronic structure calculations - Details and results

Within this work theoretical calculations were performed using density functional theory with a plane wave basis set and Projector Augmented Waves (PAW) or Vanderbilt Ultrasoft pseudopotentials (US-PP) as implemented in the VASP code (Version 4.6.36)[167,168] and without thermal influence.

First a structure optimization including a relaxation of volume, ion positions and shell shape was carried through. Afterwards precise calculations with the obtained cell parameters were performed in order to evaluate the electronic structure.
The Brillouin zone integration was performed over a Γ-centered Monkhorst-Pack grid[178–180]; convergence with respect to the number of k-points was verified. Exchange-correlation effects were treated with the generalized gradient approximation of Perdew and Wang[181]. Mixing of the charge density was done using a *Broyden-Pulay* scheme[182]. Scalar-relativistic effects were included, whereas spin-orbit couplings were ignored.

6.1 Structure optimization

Evaluation of the electronic properties during the structure optimizations was performed using the tetrahedron method with Blöchl corrections[183]. For the plane-wave cut-off of the electronic orbitals a value of 600 eV was usually applied, deviating slightly depending on the size of the system. At least 25 ionic steps were performed and Hellmann-Feynmann forces and stresses were calculated for each ionic step. The ions were relaxed into their instantaneous ground state via a conjugate-gradient algorithm. The scaling constant for the line minimization was set to 0.1 fs. After a corrector step the line minimization was improved using a variant of Brent's algorithm[184]. Forces were converged to 0.1 meV/$\AA$ and the criterion for electronic convergence was 0.01 meV.

6.2 Density of states

In order to determine the density of states neither change in ionic positions nor in cell volume were allowed. The description of the partial occupancies was done using the tetrahedron method with Blöchl corrections or in few cases the Methfessel-Paxton scheme of first order[185] together with a smearing of 0.1 eV. For evaluating the Kohn-Sham ground state through iterative matrix diagonalization the RMM-DIIS (residual minimization scheme - direct inversion in the iterative subspace) algorithm[182] combined with a fully automatic optimization of projection operators was applied.

6.3 Host lattices for (Eu(II)-) luminescence

The potential host lattices MgH_2, CaH_2, SrH_2, BaH_2, $LiSrH_3$, $LiBaH_3$ and $KMgH_3$ were studied; both US-PPs and PAWs were tested. In case of the perovskites total energies for the normal as well as the inverse cubic perovskite structure type were evaluated in order to determine the energetically favored structure type. The europium isotype of $LiSrH_3$, $LiEuH_3$, was studied using a PAW frozen core potential for Eu(II) provided in the program package VASP, since f-electrons are not handled well within DFT due to self-interaction. As the f-electrons were not treated explicitly, however, a density of states will not be discussed for this case. The inverse and normal cubic perovskites $LiBaF_3$ and $KMgF_3$, which are isotypic to their corresponding hydrides, as well as $NaMgH_3$ crystallizing in a hypothetical cubic perovskite structure and in space group *Pnma*, have also been studied using PAWs for reasons of comparison.

6.3.1 US-PP

Optimized lattice parameters of all examined hydrides are listed in Table 25.

Table 25: Optimized lattice parameters of all examined hydrides.

Compound	a calc. (exp.)[pm]	b calc. (exp.)[pm]	c calc. (exp)[pm]
MgH_2	442.9 (448.9)	442.9 (448.9)	296.9 (300.1)
CaH_2	573.8 (594.5)	347.2 (359.2)	662.6 (680.5)
SrH_2	609.3 (638.8)	374.1 (387.5)	708.3 (733.8)
BaH_2	659.2 (681.0)	407.1 (417.0)	771.2 (787.0)
$LiSrH_3$	370.1(383.5)	370.1 (383.5)	370.1 (383.5)
$SrMgH_4$	389.6 (397.4)	1286.1 (1372.0)	539.5 (558.7)

Deviations vary from 1 up to almost 5 % compared to the experimental values. This might be due to difficulties in describing negatively charged hydrogen with a pseudopotential given in the pseudopotential libraries provided together with VASP.4.6. It is even strongly recommended to use the PAW datasets, since new PPs are no longer distributed for VASP[186]. Therefore Ultrasoft Pseudopotentials as implemented in VASP.4.6 were not considered for further calculations.

6.3.2 PAWs

Optimized lattice parameters of all examined hydrides are listed in Table 26. Deviations vary from 0.5 to 2 % compared to the experimental values, which seems to be acceptable.

Table 26: Optimized lattice parameters of all examined hydrides.

Compound	a calc. (exp.)[pm]	b calc. (exp.)[pm]	c calc. (exp.)[pm]
MgH_2	450.4 (448.9)	450.2 (448.9)	301.1 (300.1)
CaH_2	582.4 (594.5)	350.2 (359.2)	681.3 (680.5)
SrH_2	635.4 (638.8)	385.2 (387.5)	729.2 (733.8)
BaH_2	684.4 (681.0)	415.8 (417.0)	787.8 (787.0)
$LiSrH_3$	380.0 (383.5)	380.0 (383.5)	380.0 (383.5)
$LiEuH_3$	370.0 (379.8)	370.0 (379.8)	370.0 (379.8)
$LiBaH_3$	401.8 (402.3)	401.8 (402.3)	401.8 (402.3)
$LiBaF_3$	405.6 (399.7)	405.6(399.7)	405.6(399.7)
$KMgH_3$	402.5 (402.5)	402.5 (402.5)	402.5 (402.5)
$KMgF_3$	407.0 (398.3)	407.0 (398.3)	407.0 (398.3)
$NaMgH_3$ (cub.)	386.2 (-)	386.2 (-)	386.2 (-)
$NaMgH_3$ (*Pnma*)	545.9 (546.5)	768.7 (769.4)	540.6 (541.2)

Potential curves for $KMgH_3$, $LiSrH_3$ and $LiBaH_3$ crystallizing in the normal and the inverse cubic perovskite structure type are shown in Fig. 114, 115 and 116.

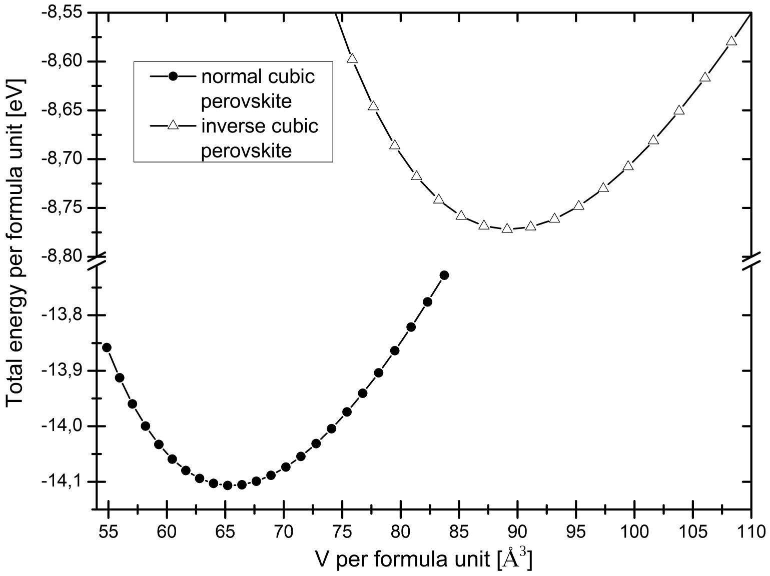

Figure 114: Potential curves for $KMgH_3$ in the normal and inverse cubic perovskite structure type.

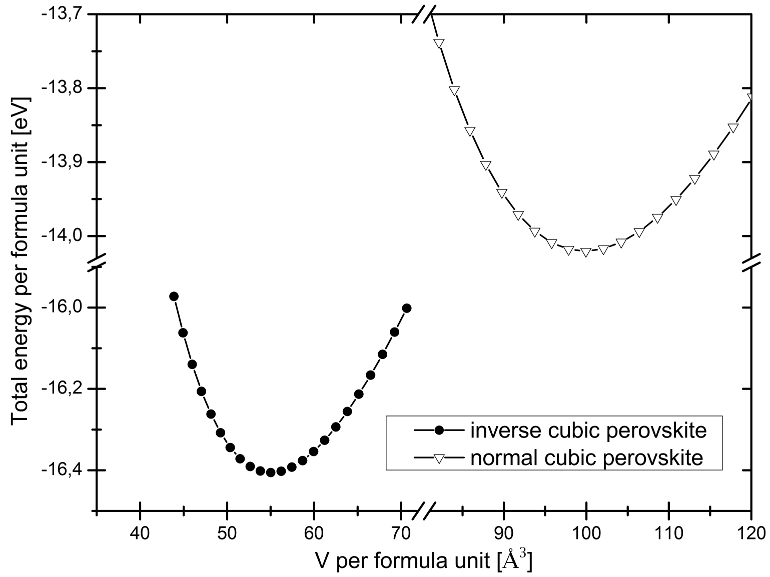

Figure 115: Potential curves for $LiSrH_3$ in the normal and inverse cubic perovskite structure type.

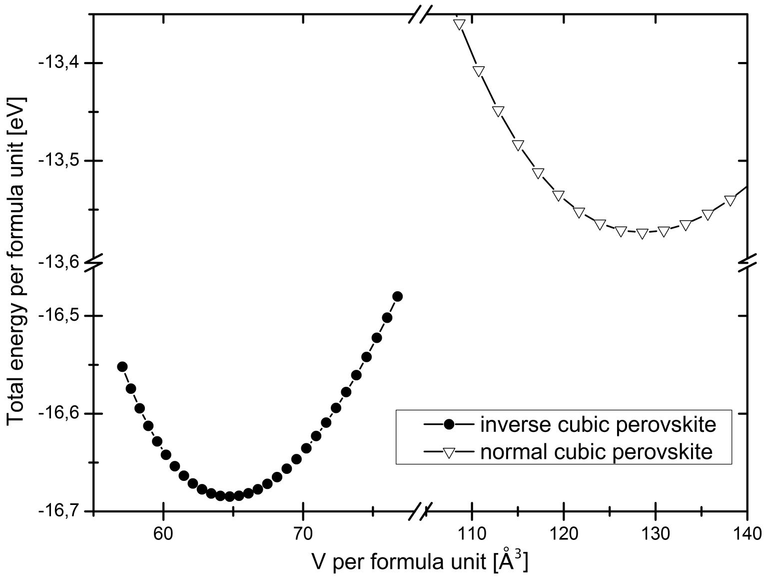

Figure 116: Potential curves for $LiBaH_3$ in the normal and inverse cubic perovskite structure type.

It is clear that the normal cubic perovskite structure type is energetically favored for $KMgH_3$, whereas for $LiSrH_3$ and $LiBaH_3$ the inverse cubic perovskite structure is preferred. Those results are in good agreement with neutron powder data from literature[37] (in case of $LiBaH_3$) and collected within this work ($LiSrH_3$). Even though neutron diffraction data are not available for $KMgH_3$, the theoretical results strongly support the assumption made for structure refinements (see Sect.4.2.6) that $KMgH_3$ crystallizes in the normal cubic perovskite type. As a conclusion, K, Sr and Ba are coordinated cuboctahedrally by hydrogen in those hosts used for Eu(II) luminescence and, assuming Eu^{2+} to occupy those sites due to size effects, the coordination sphere of the luminescence center is expected to be a cuboctahedron. Potential curves were evaluated using VASP within the ASE atomic simulation environment[187].

Bader chargers for the favored structure type are also given (see Table 27). Bader charges were evaluated using the Bader Charge Analysis script provided by the University of Texas at Austin[175–177]. The charge of the hydrogen anions is calculated to be between -0.73 and -0.78 for all considered cubic perovskite type hydrides, thus being less negative than the formal charge -1 whereas the cations carry a charge slightly smaller than the formal oxidation state of +1 and +2, respectively. The observation of charges with absolute values smaller than the formal oxidation numbers indicates that the bonding situation is not purely ionic, but also features a certain covalence. Assuming the Bader charges to be approximately the same as for Sr or Eu in $LiSrH_3$ and $LiEuH_3$ for the case of an europium-doped host lattice, such as e.g. $LiSrH_3$:Eu^{2+}, a certain covalence between the central ion Eu(II) and the hydride ligand can also be expected. This is in good agreement with the experimental determination of the location of the barycenter of the Eu(II) 5d levels and the observation of a redshift in the emission energies of Eu(II) in hydride host lattices (see 4.2.8).

Table 27: Bader charges of $A^{I}M^{II}H_3$ for the energetically more stable perovskite structure type; the value for the neutral atom is 0.

Compund	H	M^{II}	A^{I}
$KMgH_3$	-0.78	1.58	0.76
$KMgF_3$	-0.87	1.76	0.86
$LiSrH_3$	-0.75	1.42	0.83
$LiBaH_3$	-0.73	1.34	0.85
$LiBaF_3$	-0.86	1.70	0.89
$LiEuH_3$	-0.78	1.45	0.89
$NaMgH_3$ (cub.)	-0.82	1.59	0.87
$NaMgH_3$ (*Pnma*)	-0.81	1.59	0.85

In case of the hypothetical cubic $NaMgH_3$ the A-cation carries a charge almost equal to the charges of the A-cations in the fluorides $KMgF_3$ and $LiBaF_3$ and thus the hydride possesses a more negative charge than in the other hydride perovskites. In experiment, no cubic perovskite, but a variant with slightly tilted and distorted octahedra is found[44]. The absence of a cubic variant despite a tolerance factor indicating its existence is discussed in Section 4.2.9. In the orthorhombic structure the absolute values for the Bader charges of hydride and the A-cation becomes only slightly smaller and the change does not seem to be significant.

To gain a better understanding of the luminescence properties of rare earth doped alkaline-earth metal hydrides, the density of states of the pure alkaline-earth metal hydrides were evaluated (Fig.117). Among others, these calculations were supposed to deliver a crude estimation of the size of the band gaps, which might allow a preliminary selection of possible host lattices with sufficiently large band gaps.

Strictly speaking, calculated band gaps are not comparable with experimental band gaps. However, in the following they will be compared to each other, because this is a common and convenient approach being helpful in interpreting experimental results.

For MgH_2 (rutile type structure) a k-point mesh of $12 \cdot 12 \cdot 16$ was used, whereas the k-point mesh for the compounds crystallizing in the $PbCl_2$ type was $10 \cdot 16 \cdot 8$.

Furthermore, the density of states of selected ternary hydrides crystallizing in the space group $Pm\bar{3}m$ were evaluated using a k-point mesh of $15 \cdot 15 \cdot 15$ (Fig. 118).

For MgH_2, CaH_2, SrH_2 and BaH_2 band gaps of about 3.7 eV, 2.8 eV, 3.1 eV and 2.7 eV were obtained. Theoretical calculations predict sufficiently large band gaps, which is in good agreement with the experimental observation of white powders of those host materials. However, the trends observed in theoretical calculations do not correlate with the emission energies observed in the luminescence emission spectra (Ca to Ba: emission with peak maximum at 765 nm (1.621 eV), 728 nm (1.703 eV) and 755 nm (1.642 eV)). For $KMgH_3$, $LiSrH_3$ and $LiBaH_3$ the calculated band gaps are 2.6 eV, 1.8 eV and 2.0 eV, whereas the emission have their peak maximum at about 565 nm (2.194 eV), 565 nm (2.194 eV) and 530 nm (2.339 eV). Thus the knowledge of the size of the direct band gaps is not sufficient for predicting luminescence properties, even though one condition for the occurrence of luminescence is a sufficiently large band gap. However, a theoretical prediction of the size of the band gap of a possible host lattice might help in pre-selecting suitable hosts. For further predictions, the location of the 4f and 5d states of europium relatively to the valence and conduction band states of the host needs to be known. For some cases, for instance for Ce(III) in hexahalides and others, calculations explicitly treating the 4f and 5d states have been carried out using ab initio embedded cluster calculations[85,141], such methods are, however, beyond the scope of this work.

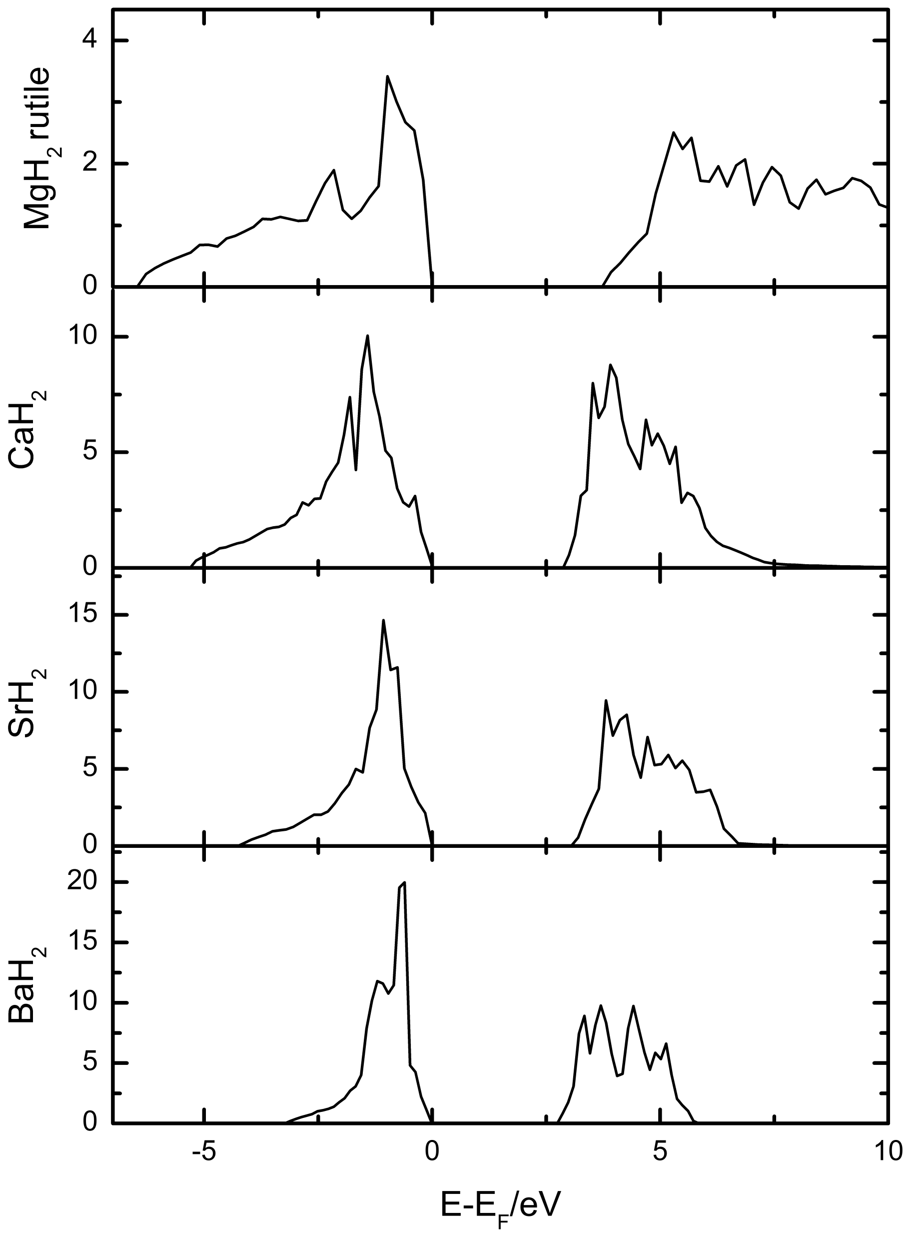

Figure 117: Density of states (DOS) of the earth alkaline metal hydrides calculated with PAW in units of states per eV and cell.

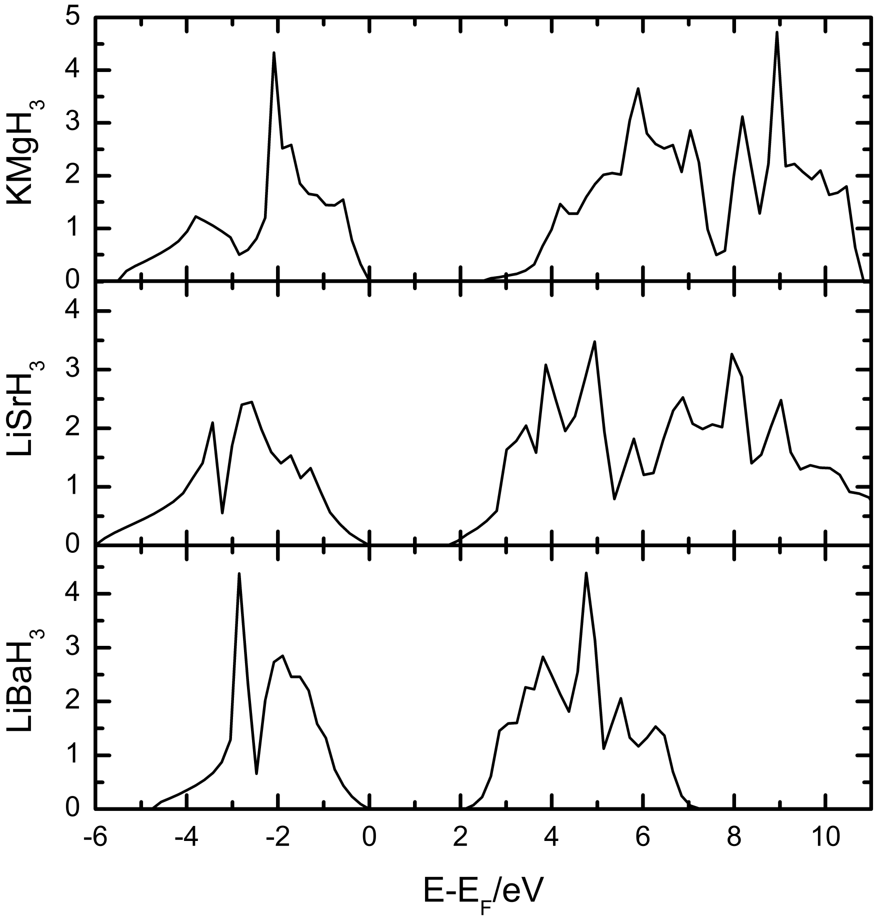

Figure 118: Density of states (DOS) of selected ternary metal hydrides calculated with PAW in units of states per eV and cell.

6.4 Theoretical studies of $Li_xSr_{1-x}AlSi$ and its corresponding hydrides

The Zintl phase SrAlSi (space group $P\frac{6}{m}mm$) and its hydride SrAlSiH (space group $P3m1$), as well as the half-Heusler phase LiAlSi (space group $F\bar{4}3m$) and its hydride $LiAlSiH_{0.9}$ (space group $F\bar{4}3m$), were studied theoretically using PAW. In order to describe the partial occupancy of Al and Si in SrAlSi on the *2d* site, an ordered arrangement was considered (space group $P\bar{6}m2$, Al on *1f*, Si on *1d*), even though in experiment it is assumed that the Al and Si atoms are distributed more or less randomly[188]. For $LiAlSiH_{0.9}$ the H atoms were placed in the tetrahedral voids (*4d* site) and a full occupancy was assumed.

Furthermore, the mixed systems $Li_xSr_{1-x}AlSi$ and $Li_xSr_{1-x}AlSiH$ were investigated in order to estimate the relative stabilities of the structure types with increasing lithium content. Relative stabilities of the mixed crystals $Li_xSr_{1-x}AlSi$ were calculated for the cubic and the hexagonal modification. Likewise, relative stabilities of $Li_xSr_{1-x}AlSiH$ were calculated for the cubic and the trigonal modification. For the hypothetic cubic modifications, 2x2x2 super cells were used. Starting from the unit cell $F\bar{4}3m$, a *klassengleiche* (IIa) transition to $P\bar{4}3m$, followed by a *klassengleiche* (IIb) transition with a doubling of the axes to $F\bar{4}3m$ was carried through. As for the unit cell, a full occupancy of the H position was assumed for $Li_xSr_{1-x}AlSiH$. For the trigonal modification of $Li_xSr_{1-x}AlSiH$ a 2x2x1 super cell was created by a *klassengleiche* (IIc) transition with a doubling of the a and b axes, which corresponds to an enlargement of the mesh size in the a,b plane and therefore a mixed occupation within the layers. For the hexagonal modification of $Li_xSr_{1-x}AlSi$ a 1x1x4 super cells was created. As for the unit cell of SrAlSi, first an ordered arrangement was considered (spacegroup $P\bar{6}m2$, Al on *1f*, Si on *1d*). Afterwards two *klassengleiche* (IIc) transitions with doubling of the c-axis were carried out. Due to the large size of the systems, ion positions were only relaxed for the end members of the hypothetical solid solutions series. For all other calculations, only cell volumes, but no ion positions were relaxed.

6.4.1 Lattice parameters of the unit cells

Optimized lattice parameters of all examined compounds are listed in Table 28. Deviations from the experimental values for the pure compounds are about or less than 1 %.

Table 28: Optimized lattice parameters of all examined hydrides.

	a calc. (exp.) [pm]	b calc. (exp.) [pm]	c calc. (exp.) [pm]
LiAlSi	593.9 (592.8)	593.9 (592.8)	593.9 (592.8)
LiAlSiH	593.3 (592.8)	593.3 (592.8)	593.3 (592.8)
SrAlSi	426.6 (421.5)	426.6 (421.5)	475.6 (477.0)
SrAlSiH	422.8 (421.39)	22.8 (421.39)	495.2 (495.50)

6.4.2 Density of states of the unit cells

The densities of states of the pure compounds were evaluated. For SrAlSi and its hydride SrAlSiH a Γ-centered k-point mesh of 12 · 12 · 14 (344 irreducible k-points and 1012, respectively) was used, whereas the k-point mesh for the compounds LiAlSi and its hydride LiAlSiH was 15 · 15 · 15 (resulting in 120 irreducible k-points). The evaluation of the partial occupancies was carried out using the tetrahedron method with Blöchl corrections.

According to the theoretical calculations, LiAlSi, LiAlSiH and SrAlSiH are semiconductors with rather small band gaps, whereas SrAlSi is metallic (see Fig. 119). The DOS of SrAlSi[189] and SrAlSiH are in good agreement with earlier calculations[66,189,190]. It should be noted that DFT usually underestimates band gaps, so that the gaps are probably slightly larger.

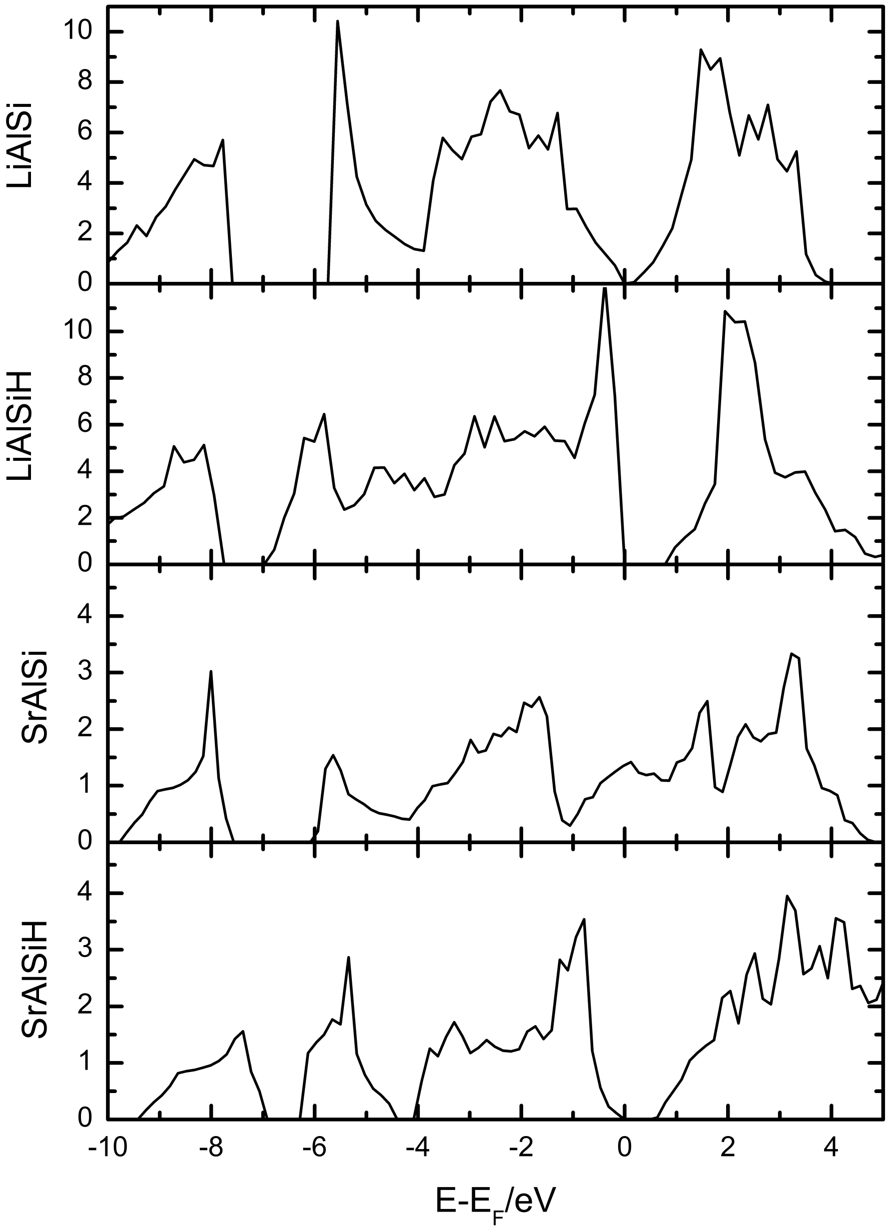

Figure 119: Density of states (DOS) calculated with PAW (Tetrahedron method) in units of states per eV and cell.

6.4.3 Relative stabilities and structural parameters of the super cells

Calculated relative stabilities and structural parameters of $Li_xSr_{1-x}AlSi$ in $F\bar{4}3m$ and $P\bar{6}m2$ and $Li_xSr_{1-x}AlSiH$ in $F\bar{4}3m$ and $P3m1$ are listed below (see Table 29 and 30).

Table 29: Optimized lattice parameters, volumes and volumes per formula unit of $Li_xSr_{1-x}AlSi$ in $F\bar{4}3m$ and $P\bar{6}m2$.

x	$F\bar{4}3m$			$P\bar{6}m2$			
	a [pm]	V [pm^3]	V (f.u.) [pm^3]	a [pm]	c [pm]	V [pm^3]	V (f.u.) [pm^3]
1	1184.2	$1.66 \cdot 10^9$	$5.19 \cdot 10^7$	410.3	1857.4	$1.82 \cdot 10^8$	$4.54 \cdot 10^7$
0.875	1213.3	$1.79 \cdot 10^9$	$5.58 \cdot 10^7$	-	-	-	-
0.75	1236.1	$1.89 \cdot 10^9$	$5.90 \cdot 10^7$	414.9	1878.1	$1.88 \cdot 10^8$	$4.9 \cdot 10^7$
0.5	-	-	-	418.3	1893.6	$1.92 \cdot 10^8$	$4.81 \cdot 10^7$
0.25	1318.1	$2.29 \cdot 10^9$	$7.16 \cdot 10^7$	421.4	1917.7	$1.98 \cdot 10^8$	$4.93 \cdot 10^7$
0.125	1345.0	$2.43 \cdot 10^9$	$7.60 \cdot 10^7$	-	-	-	-
0	1359.8	$2.51 \cdot 10^9$	$7.86 \cdot 10^7$	426.6	1902.4	$2.01 \cdot 10^8$	$5.03 \cdot 10^7$

Table 30: Optimized lattice parameters, volumes and volumes per formula unit of $Li_xSr_{1-x}AlSiH$ in $F\bar{4}3m$ and $P3m1$.

x	$F\bar{4}3m$			$P3m1$			
	a [pm]	V [pm^3]	V (f.u.) [pm^3]	a [pm]	c [pm]	V [pm^3]	V (f.u.) [pm^3]
1	1182.6	$1.65 \cdot 10^9$	$5.17 \cdot 10^7$	812.2	481.3	$1.84 \cdot 10^8$	$4.61 \cdot 10^7$
0.875	1214.0	$1.79 \cdot 10^9$	$5.591 \cdot 10^7$	-	-	-	-
0.75	1231.4	$1.87 \cdot 10^9$	$5.836 \cdot 10^7$	822.2	487.3	$1.91 \cdot 10^8$	$4.78 \cdot 10^7$
0.5	-	-	-	-	-	-	-
0.25	1318.1	$2.29 \cdot 10^9$	$7.16 \cdot 10^7$	836.4	495.7	$2.01 \cdot 10^8$	$5.03 \cdot 10^7$
0.125	1317.9	$2.29 \cdot 10^9$	$7.16 \cdot 10^7$	-	-	-	-
0	1330.4	$2.35 \cdot 10^9$	$7.36 \cdot 10^7$	842.4	499.3	$2.06 \cdot 10^8$	$5.14 \cdot 10^7$

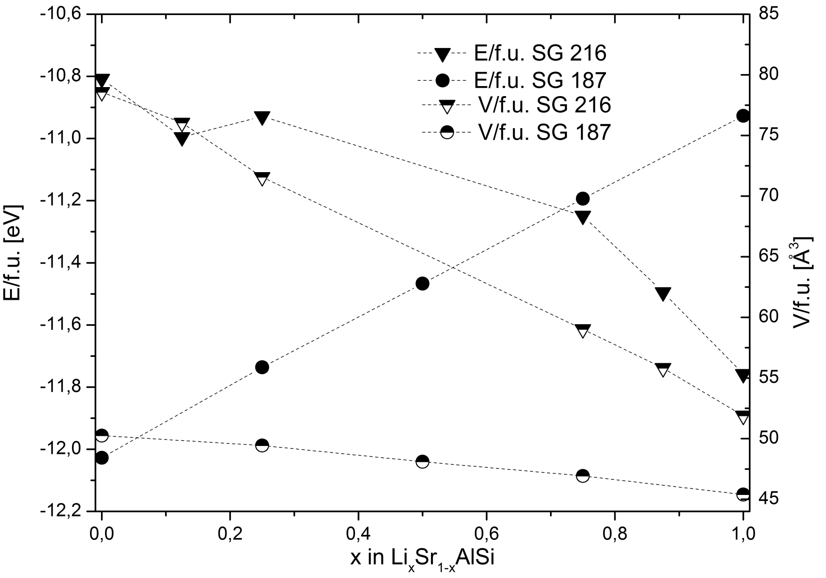

Figure 120: Relative energies and volumes per formula unit for the hypothetical mixed system $Li_xSr_{1-x}AlSi$ in the space groups $F\bar{4}3m$ (216) and $P\bar{6}m2$ (187).

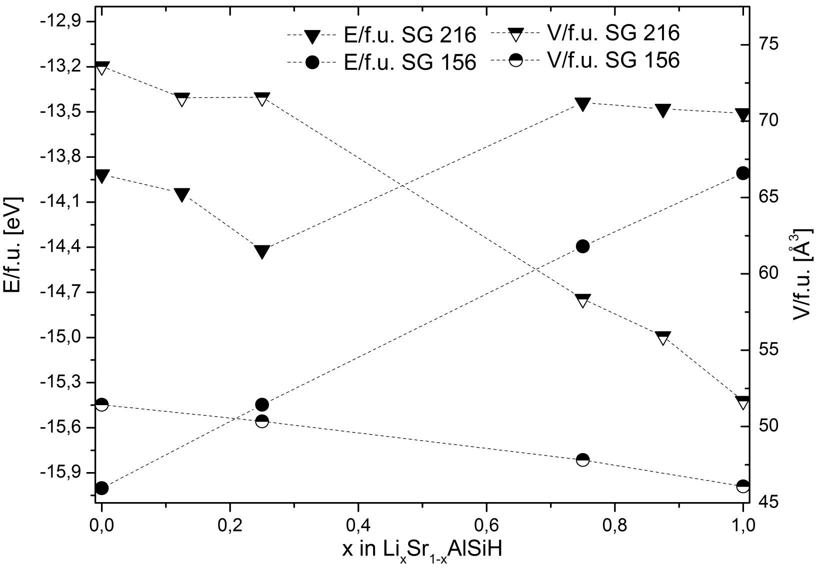

Figure 121: Relative energies and volumes per formula unit for the hypothetical mixed system $Li_xSr_{1-x}AlSiH$ in the space groups $F\bar{4}3m$ (216) and $P3m1$ (156).

As expected for the strontium-rich side, the hexagonal structure type ($P\bar{6}m2$) was found to be more stable than the cubic ($F\bar{4}3m$) in $Li_xSr_{1-x}AlSi$, whereas the cubic structure type is stable for the lithium-rich side. This result is in good agreement with the experimental observation of the cubic structure type for LiAlSi and the hexagonal structure type for SrAlSi. For x = $\frac{3}{4}$, the cubic structure type becomes more stable. It would be interesting to experimentally check the validity of the theoretical result predicting a transition in structure type, which is, however, beyond the scope of this work. In case of an experimental study it should, however, be kept in mind that kinetic effects and entropy may also effect the results of a study. For the hydrides $\mathrm{Li}_x\mathrm{Sr}_{1-x}\mathrm{AlSiH}$ the trigonal structure type ($P\,3m1$) was found to be relatively more stable than the cubic structure type ($F\bar{4}3m$) for x = 0-1. Thus the theoretical result is in agreement with experiment for SrAlSiH, but it is, similar to experimental findings[64], inconsistent with the existence of a cubic LiAlSiH claimed in[63]. Using the *in-situ* single-crystal sapphire cell, LiAlSiH ($F\bar{4}3m$) could not be obtained[64], but at high hydrogen pressures a new structure, which was indexed as trigonal, was observed. However, the metric of the possibly trigonal hydride of LiAlSi did not match the cell parameters of the structure used in calculations. Anyhow, the existence of a cubic LiAlSiH is questionable and a hydride of LiAlSi might crystallize in a trigonal structure type different from the one used in calculations. Therefore, further experimental studies are necessary in order to give a definite answer.

7 Summary and outlook

For the first time a systematic study of Eu(II) luminescence in different hydride host lattices was carried out. Hydridic matrices had not been used as host lattices for Eu(II) before and except for Eu(II)-luminescence in SrH_2:Eu^{2+}, which had been prepared during preliminary works[34], Eu(II) luminescence had never been observed within a hydride host lattice. All samples showed broad luminescence emission and absorption bands at RT which are due to parity-allowed electric dipole transitions between the $4f^7$ and $4f^65d$ levels of Eu^{2+}.

It could be shown that the use of hydride host lattices leads to a redshift in the emission energies compared to so-far known host lattices. This redshift was mainly explained with the softness of the hydride ligand and the resulting covalence of the europium-hydride bond which leads to a shift of the barycenter of the 5d levels to lower energies. Its size shows a dependence on the coordination geometry and the metal-hydride interatomic distances.

Crystal field strengths were also estimated for certain host lattices and it was concluded that the larger crystal field strength in hydrides also plays a role in the redshift, however, its effect is much smaller than the effect of the centroid shift.

The widest redshift was observed for the compounds $Eu_xM_{1-x}H_2$ (M = Ca, Sr, Ba) with x = 0.5-1% and the distorted perovskite $NaMgH_3$:Eu^{2+} (1.0 mol%). The maximum emission wavelengths are 764 nm (M = Ca), 728 nm (M = Sr), 750 nm (M = Ba) and 700 nm ($NaMgH_3$).

Furthermore, temperature dependent luminescence and decay curves were studied for the inverse perovskites $LiSrH_3$:Eu^{2+}, $LiSrD_3$:Eu^{2+}, $LiBaH_3$:Eu^{2+} and $LiBaD_3$:Eu^{2+} (0.5 mol%), the normal cubic perovskite $KMgH_3$:Eu^{2+} (1.0 mol%) and the orthorhombically distorted perovskite $NaMgH_3$:Eu^{2+} (1.0 mol%). In case of the Sr and Ba perovskites all samples showed a vibrational fine structure at low temperatures, which was exceptionally well-resolved for the Sr compounds. Especially in $LiSrH_3$:Eu^{2+} it was possible to distinguish a coupling with at least three different modes. The assignment of the vibrational modes in luminescence excitation and emission spectra of $LiSrH_3$:Eu^{2+} and $LiSrD_3$:Eu^{2+} even allowed to determine that the bonding in the $4f^{n-1}5d(e_g)$ excited state is weaker than in the ground state. These well-resolved spectra also permit the first quantitative estimation of the crystal field strength of hydride and deuteride ever. Furthermore, the comparison between the exceptionally well-resolved vibrational modes of $LiSrH_3$:Eu^{2+} and $LiSrD_3$:Eu^{2+} also allowed to confirm previous research claiming that low energy acoustic phonons do not show the expected $\sqrt{2}$-dependence and are similar for hydrides and deuterides.

Hydride-fluoride mixed crystals could be synthesized in the systems EuH_xF_{2-x} (x = 0-0.8), SrH_xF_{2-x}:Eu^{2+} (x = 0-0.5) and $LiBaH_xF_{3-x}Eu^{2+}$ and $KMgH_xF_{3-x}Eu^{2+}$ (x = 1). For the first time Eu(II)-luminescence was studied in hydride-fluoride host lattices. Especially EuH_xF_{2-x} allowed the design of varying luminescence colors from dark red for hydride-rich samples to orange and yellow for fluoride-rich samples, but also the other mixed coumpounds showed that an increase in fluoride compared to hydride leads to significant blueshifts of the emission wavelength of Eu(II). Further optimization of the preparation conditions might allow the targeted design of mixed compounds with desired emission wavelengths.

Additionally, in EuHCl Eu(II)-luminescence could be observed for the first time in a mixed hydride-chloride compound. Even though samples were not completely phase pure, it is clear that EuHCl shows an extremely bright luminescence. Further optimization of the synthesis might yield a phosphor with very high emission intensities.

In the systems YbH_{2+x} and YbD_{2+x} a reversible signal at approx. 350°C and 50 bar hydrogen pressure was observed in the DSC, thus leading to the suggestion that a further hydrogen uptake under high hydrogen pressure might be possible. *In-situ* neutron diffraction measurements of YbD_{2+x} within the single crystal sapphire high-pressure cell at 50 bar deuterium pressure showed the formation of new, slightly different reflections at 350°C. However, the reaction could not be completed and it was not possible to completely solve the structure from the data available. The observed expansion of the lattice parameters was slightly larger than thermal expansion reported for similar compounds. Therefore, a further deuterium uptake seems plausible.

Relative stabilities and structural parameters were calculated for mixed crystals of the Half-Heusler phase LiAlSi and the Zintl phase SrAlSi in both space groups, $F\bar{4}3m$ and $P\bar{6}m2$ as well as for the mixed crystals of their corresponding hydrides $Li_xSr_{1-x}AlSiH$ in $F\bar{4}3m$ and $P3m1$. Calculations for the end members LiAlSi, SrAlSi and SrAlSiH confirmed previous experimental works, whereas the existence of the hydride LiAlSiH in $F\bar{4}3m$ could not be confirmed. This results is in agreement with experimental results within the group and further experiments are necessary to clarify this question beyond doubt.

8 Appendix

8.1 List of abbreviations

acc.	according to
a.u.	arbitrary units
av.	average
bra-ket notation $\langle \Phi \mid \Psi \rangle$	$\int dx\, \Psi^*(x) \cdot \Phi(x)$
CN	coordination number
DFT	density functional theory
DOS	density of states
DSC	differential scanning calorimetry
FWHM	Full width at half maximum
GGA	generalized gradient approximation
ILL	Institute Laue-Langevin
LDA	local density approximation
LED	light emitting diode
mol%	mol-percentage
MR	molar ratio
occ.	occupation number
PAWs	projector augmented waves
RM-DIIS	residual minimization scheme - direct inversion in the iterative subspace
RT	room temperature
SG	space group
site sym.	site symmetry
US-PP	ultrasoft pseudopotential
UV	ultra violet
w%	weight percentage
XRD	X-ray diffraction

8.2 Structural data of important host lattices studied within this work

Using XRD data, only metal positions, but no hydrogen positions were refined. Hydrogen positions were either taken from literature or refined from neutron powder diffraction data (usually of the deuterides).

8.2.1 The $PbCl_2$ structure type

- space group *Pnma*
- representatives: the alkaline-earth metal hydrides CaH_2, SrH_2, BaH_2 and EuH_2 and YbH_2

Table 31: CaH_2 (positions acc.[30]); a = 594.47(5) pm, b = 359.20(2) pm, c = 680.47(5) pm. (Standard deviations as given by the program Fullprof).

site	site sym.	atom	x	y	z	occ.
4c	*.m.*	Ca	0.2424	1/4	0.10860	1
4c	*.m.*	H1	0.3543	1/4	0.4264	1
4c	*.m.*	H2	0.9727	1/4	0.6775	1

Table 32: SrH_2 (positions acc.[10]); a = 638.175(9) pm, b = 387.428(6) pm, c = 732.23(1) pm. (Standard deviations as given by the program TOPAS).

site	site sym.	atom	x	y	z	occ.
4c	*.m.*	Sr	0.2598	1/4	0.8890	1
4c	*.m.*	H1	0.6450	1/4	0.9267	1
4c	*.m.*	H2	0.0235	1/4	0.1771	1

Table 33: BaH_2 (positions acc.[10]); a = 681.03(7) pm, b = 416.79(3) pm, c = 787.04(7) pm. (Standard deviations as given by the program Fullprof).

site	site sym.	atom	x	y	z	occ.
4c	*.m.*	Ba	0.2591	1/4	0.8849	1
4c	*.m.*	H1	0.6360	1/4	0.9209	1
4c	*.m.*	H2	0.0376	1/4	0.1823	1

Table 34: EuH_2; a = 626.06(3) pm, b = 380.98(1) pm, c = 722.43(3)) pm. (Standard deviations as given by the program TOPAS).

site	site sym.	atom	x	y	z	occ.
4c	*.m.*	Eu	0.2404(9)	1/4	0.8852(3)	1
4c	*.m.*	H1	0.6450	1/4	0.9267	1
4c	*.m.*	H2	0.9735	1/4	0.6771	1

Table 35: YbD_2; a = 593.72(3) pm, b = 361.46(2) pm, c = 7680.70(4)) pm. (Standard deviations as given by the program TOPAS).

site	site sym.	atom	x	y	z	occ.
4c	*.m.*	Yb	0.257(1)	1/4	0.3907(5)	1
4c	*.m.*	D1	0.1446	1/4	0.06940	1
4c	*.m.*	D2	0.02830	1/4	0.6770	1

8.2.2 The inverse cubic perovskite structure type

- space group $Pm\bar{3}m$
- representatives: $LiSrH_3$, $LiBaH_3$, $LiEuH_3$ and the corresponding deuterides, $LiBaF_3$

Table 36: The inverse cubic perovskite structure type using the example of $LiSrH_3$; a = 383.572(4) pm. (Standard deviations as given by the program TOPAS).

site	site sym.	atom	x	y	z	occ.
1b	$m\bar{3}m$	Sr	1/2	1/2	1/2	1
1a	$m\bar{3}m$	Li	0	0	0	1
3d	$m\bar{3}m$	H	1/2	0	0	1

The lattice constants a of the compounds crystallizing in the inverse cubic perovskite structure type within this work (Standard deviations as given by the program TOPAS) are listed in Table 37. Note that more than one sample of $LiSrH_3$:Eu^{2+} and $LiBaH_3$:Eu^{2+} were prepared in order to confirm the observation of the yellow and green Eu(II) luminescence, the date of preparation is therefore given in parentheses. In case more than one sample is given, samples used for luminescence measurements at low temperature are marked with a *.

Table 37: Lattice constant a of inverse cubic perovskites.

ABX_3	a [pm]
$SrLiH_3$	383.572(4)
$SrLiH_3$:Eu^{2+} (0.5 mol%) (11/11/2010)	383.484(2)
$SrLiH_3$:Eu^{2+} (0.5 mol%) (13/12/2011 Nr.1)*	383.498(3)
$SrLiH_3$:Eu^{2+} (0.5 mol%) (13/12/2011 Nr.2)	383.444(2)
$SrLiD_3$:Eu^{2+} (0.5 mol%)	382.535(3)
$BaLiH_3$	402.395(1)
$BaLiH_3$:Eu^{2+} (18/07/2011)	402.349(2)
$BaLiH_3$:Eu^{2+} (22/11/2011)*	402.284(3)
$BaLiD_3$	401.459(3)
$BaLiF_3$:Eu^{2+}	399.692(1)

8.2.3 The normal cubic perovskite structure type

- space group $Pm\bar{3}m$
- representatives: $KMgH_3$

Table 38: The normal cubic perovskite structure type using the example of $KMgH_3$; a = 402.629(6) pm. (Standard deviations as given by the program TOPAS).

site	site sym.	atom	x	y	z	occ.
1b	$m\bar{3}m$	K	1/2	1/2	1/2	1
1a	$m\bar{3}m$	Mg	0	0	0	1
3d	$m\bar{3}m$	H	1/2	0	0	1

8.2.4 The orthorhombically distorted perovskite structure type of $NaMgH_3$

Table 39: The orthorhombically distorted perovskite structure type of $NaMgH_3$ using the example of $NaMgH_3:Eu^{2+}$ (1 mol%); a = 546.84(1) pm, b = 771.13(2) pm, c = 545.21(1) pm, *Pnma*. (Standard deviations as given by the program TOPAS).

site	site sym.	atom	x	y	z	occ.
4b	$\bar{1}$	Mg	0	0	1/2	1
4c	*m*	Na	0.015	1/4	0.082	1
4c	*m*	H	0.064	1/4	0.483	1
8d	*1*	H	0.292	0.040	0.708	1

8.2.5 $SrMgH_4$

Table 40: $SrMgH_4$; a = 397.478(3) pm,b = 1372.21(1) pm, c = 558.752(5) pm, $Cmc2_1$. (Standard deviations as given by the program TOPAS).

site	site sym.	atom	x	y	z	occ.
4a	*m*	Sr	0	0.3582	0.3615	1
4a	*m*	Mg	0	0.0831	0.3241	1
4a	*m*	H	0	0.0285	0.0	1
4a	*m*	H	0	0.1674	0.5946	1
4a	*m*	H	0	0.1983	0.1238	1
4a	*m*	H	0	0.5773	0.3121	1

8.2.6 The fluorite structure type

- space group $Fm\bar{3}m$
- representatives: EuF_2, SrF_2 and mixed crystals in the systems EuH_xF_{2-x} and SrH_xF_{2-x}

Table 41: The fluorite structure type using the example of EuF_2; a = 583.947(5) pm. (Standard deviations as given by the program TOPAS).

site	site sym.	atom	x	y	z	occ.
4a	$m\bar{3}m$	Eu	0	0	0	1
8c	$m\bar{3}m$	F	1/4	1/4	1/4	1

8.2.7 Single crystal and powder data of Eu_2H_3Cl

Table 42: Eu_2H_3Cl (single crystal) according to[153]; a = 409.19(6) pm, c = 690.71(14).

site	site sym.	atom	x	y	z	occ.
2d	$3m$	Eu	2/3	1/3	0.2886(3)	1
1a	$\bar{3}m$	Cl	0	0	0	1
2d	$3m$	H	2/3	1/3	0.85(4)	1
1b	$\bar{3}m$	H	0	0	1/2	1

Table 43: Eu_2H_3Cl according to the Ba_2H_3Cl structure[154]; a = 424.03(2) pm, c = 676.97(8).

site	site sym.	atom	x	y	z	occ.
2d	$3m$	Eu	2/3	1/3	0.2105	1
1a	$\bar{3}m$	Cl	0	0	1/2	1
2d	$3m$	H	1/3	2/3	0.1705	1
1b	$\bar{3}m$	H	0	0	0	1

Table 44: Eu_2H_3Cl (single crystal) according to[155]; a = 409.7(1) pm, c = 696.2(2).

site	site sym.	atom	x	y	z	occ.
2d	*3m*	Eu	1/3	2/3	0.7072(1)	1
1a	$\bar{3}m$	Cl	0	0	0	1
2d	*3m*	H	1/3	2/3	0.370(14)	1
1b	$\bar{3}m$	H	0	0	1/2	1

Note that the members of the site *2d* are 1/3, 2/3, z and 2/3, 1/3, $\bar{z}$ so that both structural data are quite similar, but not exactly the same.

8.3 Luminescence spectra and lifetimes

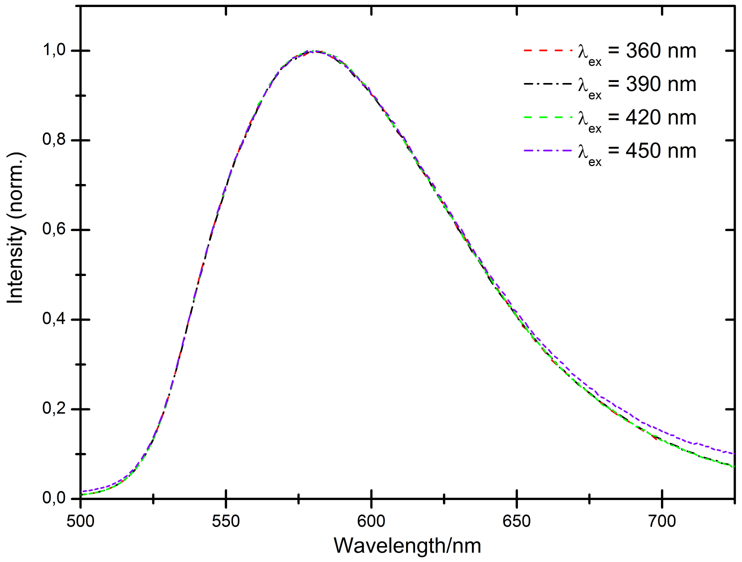

Figure 122: Luminescence spectra (FM4) of $LiSrH_3:Eu^{+2}$ (0.5 %) at 293 K, excitation from 360 nm to 450 nm.

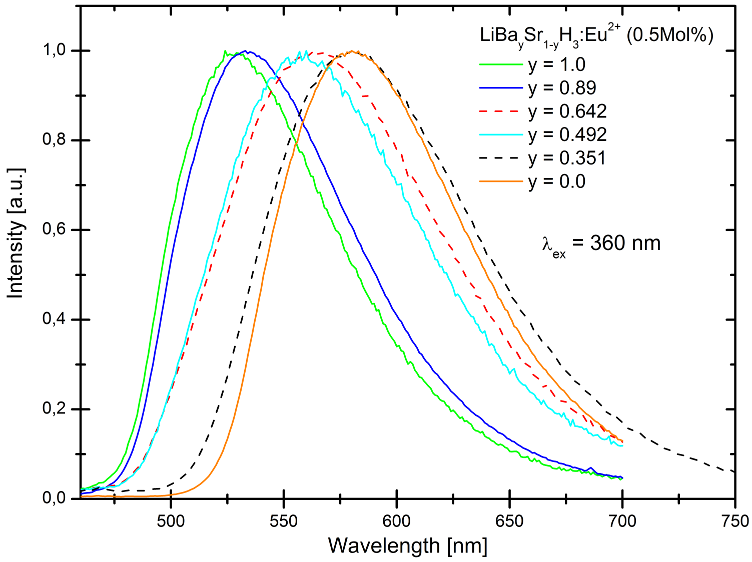

Figure 123: Luminescence spectra (FM4) of $LiSr_{1-y}Ba_yH_3:Eu^{+2}$ (0.5 %) at 293 K (y corresponds to the initial weight).

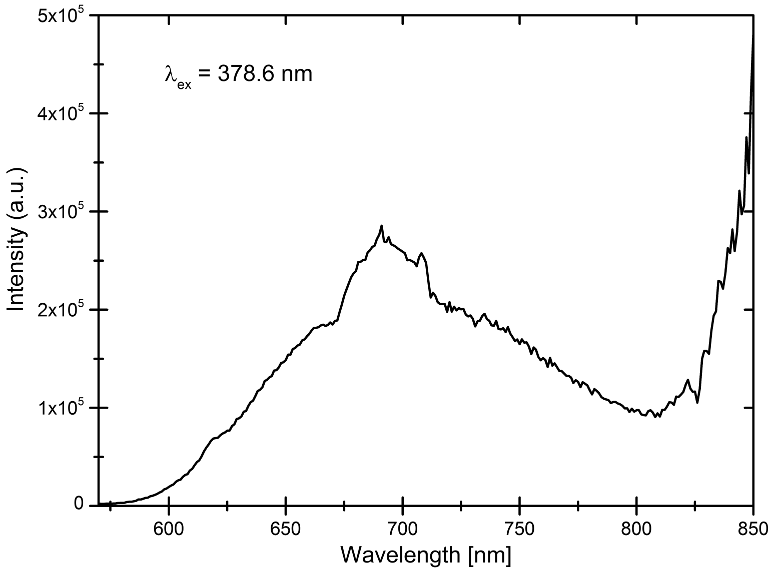

Figure 124: Emission spectrum (FL920) of $NaMgH_3$:Eu^{2+} (approx. 1 mol%) at 4 K, corrected for lamp sensitivity. Excitation at 376.8 nm.

Table 45: Temperature dependence of the decay times of $EuH_{0.278}F_{1.722}$, data based on biexponential fit.

T	τ_{short} [ns]	τ_{long} [ns]
4	76	473
15	72	482
45	72	481
90	65	454
130	61	435
180	61	376
220	57	307
255	31	156
293	13	64

8.4 Temperature-dependent lattice constants and structural data of YbD_{2+x}

Since it is unclear if the temperature calibration of the pyrometer obtained for Pd is suited (as discussed in Sect.4.8.3), both the temperatures originally measured with the pyrometer as well as the temperatures obtained from the calibration curve are listed in the following.

Table 46: Temperature dependence of the lattice parameters of YbD_{2+}, phase I and II.

		Phase I		Phase II	
T orig. [°C]	T (Pd) [°C]	a [pm]	c [pm]	a [pm]	c [pm]
29	35	633.63(3)	897.4(1)	-	-
49	53	633.72(3)	897.5(1)	-	-
89	89	633.85(3)	897.9(1)	-	-
124	120	634.06(3)	898.45(4)	-	-
158	149	634.29(3)	898.78(9)	-	-
186	173	634.47(2)	899.47(8)	-	-
217	199	634.74(2)	899.90(7)	-	-
253	228	635.00(2)	900.37(7)	-	-
287	254	635.28(2)	900.58(8)	-	-
322	281	635.39(2)	900.75(7)	-	-
355	306	635.61(2)	901.11(8)	-	-
397	336	635.89(5)	901.0(1)	638.4(3)	904.6(8)
430	359	636.01(3)	901.8(1)	640.1(2)	905.8(6)
441	367	636021(5)	901.8(1)	640.2(1)	906.3(5)
451	373	635.96(3)	902.1(1)	640.5(1)	906.4(5)
464	382	635.99(3)	902.3(1)	640.8(1)	906.8(4)

Structural data of YbD_{2+x} phase I at RT and 382°C as well as phase II at 382°C are given in Tab.47, 48 and 49. A list of interatomic distances is given in Tab.50.

Table 47: YbH_{2+x} phase I at RT; a = 633.49(1) pm, c = 898.71(3) pm, SG $P\bar{3}1m$,structural data according to[26] and additional *2d* site; occupation number of Yb and all positions fixed, B of all Yb and D, respectively, were coupled. (Standard deviations as given by the program TOPAS). Molecular formula acc. occupation: $YbD_{2.25}$.

site	site sym. (Np)	atom	x	y	z	occ.	B
Yb1	1a	Yb	0	0	0	1	0.44(1)
Yb2	2c	Yb	1/3	2/3	0	1	0.44(1)
Yb3	6k	Yb	0	0.3387	0.3295	1	0.44(1)
D1	2d	D	1/3	2/3	1/2	0.14(1)	0.87(5)
D2	6k	D	0.332	0	0.582	0.86(1)	0.87(5)
D3	2e	D	0	0	0.646	0.91(1)	0.87(5)
D4	4h	D	1/3	2/3	0.212	0.90(1)	0.87(5)
D5	6k	D	0.353	0	0.0717	0.74(1)	0.87(5)
D6	6k	D	0.2383	0	0.8293	0.809(9)	0.87(5)

Table 48: YbH_{2+x} phase I at 382°C; a = 635.92(3) pm, c = 902.2(1) pm, SG $P\bar{3}1m$,structural data according to[26] and additional *2d* site; occupation number of Yb and all positions fixed, B of all Yb and D, respectively, were coupled. (Standard deviations as given by the program TOPAS). Molecular formula acc. occupation: $YbD_{2.44}$.

site	site sym. (Np)	atom	x	y	z	occ.	B
Yb1	1a	Yb	0	0	0	1	1.1(1)
Yb2	2c	Yb	1/3	2/3	0	1	1.1(1)
Yb3	6k	Yb	0	0.3387	0.3295	1	1.1(1)
D1	2d	D	1/3	2/3	1/2	0.38(4)	2.7(1)
D2	6k	D	0.332	0	0.582	1.00(5)	2.7(1)
D3	2e	D	0	0	0.646	0.72(6)	2.7(1)
D4	4h	D	1/3	2/3	0.212	0.79(4)	2.7(1)
D5	6k	D	0.353	0	0.0717	0.91(5)	2.7(1)
D6	6k	D	0.2383	0	0.8293	0.85(2)	2.7(1)

Table 49: YbH_{2+x} phase II at 382°C; a = 640.7(1) pm, c = 906.9(4) pm, SG $P\bar{3}1m$,structural data according to[26] and additional *2d* site; occupation number of Yb and all positions fixed, B of all Yb and D, respectively, were coupled. (Standard deviations as given by the program TOPAS). Molecular formula acc. occupation: $YbD_{2.07}$.

site	site sym. (Np)	atom	x	y	z	occ.	B
Yb1	1a	Yb	0	0	0	1	1.9(1)
Yb2	2c	Yb	1/3	2/3	0	1	1.9(1)
Yb3	6k	Yb	0	0.3387	0.3295	1	1.191)
D1	2d	D	1/3	2/3	1/2	0.45(4)	3.4(1)
D2	6k	D	0.332	0	0.582	1.00(8)	3.4(1)
D3	2e	D	0	0	0.646	0.39(8)	3.4(1)
D4	4h	D	1/3	2/3	0.212	0.56(4)	3.4(1)
D5	6k	D	0.353	0	0.0717	0.94(7)	3.4(1)
D6	6k	D	0.2383	0	0.8293	0.51(2)	3.4(1)

Table 50: Interatomic distances [in pm] in the refined structures of YbH_{2+x}. (Standard deviations as given by the program TOPAS).

		phase I RT	phase I 382°C	phase II 382°C
Yb1 -	D6 (6x)	215.2	216.0	217.5
	D5 (6x)	232.7	233.6	235.3
Yb2 -	D4 (2x)	190.5	191.2	192.3
	D5 (6x)	215.1	215.9	217.5
	D6 (6x)	290.6	291.7	293.7
Yb3 -	D3 (1x)	215.7	216.5	218.1
	D2 (2x)	224.1	224.9	226.6
	D2 (1x)	227.2	228.1	229.2
	D2 (1x)	229.2	230.7	231.7
	D5 (1x)	231.9	232.8	233.9
	D4 (2x)	234.6	235.5	237.2
	D6 (2x)	238.3	239.5	240.9
	D1 (2x)	269.5	260.5	262.3
shortest dist.				
D -	D	211.9	212.7.	214.3
Yb -	Yb	362.8	363.6	365.6

References

[1] Blasse, G. *J. Alloys Compd.* **1995**, *225*, 529–533.

[2] Jüstel, T.; Nikol, H.; Ronda, C. *Angew. Chem. Int. Ed.* **1998**, *37*, 3084–3103.

[3] Höppe, H. A. *Angew. Chem. Int. Ed.* **2009**, *48*, 3572–3582.

[4] Feldmann, C.; Jüstel, T.; Ronda, C. R.; Schmidt, P. J. *Adv. Funct. Mater.* **2003**, *13*, 511–516.

[5] Dorenbos, P. *J. Lumin.* **2003**, *104*, 239–260.

[6] Messer, C. E. *J. Solid State Chem.* **1970**, *2*, 144–155.

[7] Riedel, E. *Anorganische Chemie*; de Gruyter, 2004.

[8] Kohlmann, H. *Encyclopedia of Physical Science and Technology*, 3rd ed.; Academic Press, 2002; Vol. 9, pp 441–458.

[9] Holleman, A. F.; Wiberg, E.; Wiberg, N. *Lehrbuch der Anorganischen Chemie*; de Gruyter, 2007.

[10] Ting, V. P.; Henry, P. F.; Kohlmann, H.; Wilson, C. C.; Weller, M. T. *Phys. Chem. Chem. Phys.* **2010**, *12*, 2083–2088.

[11] Kohlmann, H.; Yvon, K. *J. Alloys Compd.* **2000**, *299*, L16–L20.

[12] Yvon, K. *Z. Kristallogr.* **2003**, *218*, 108–116.

[13] Peisl, H. *Phys. Unserer Zeit* **1978**, *9*, 37–45.

[14] Yvon, K. In *Encyclopedia of Materials: Science and Technology*; 2004; Chapter Metal Hydrides: Transition Metal Hydride Complexes, pp 1–9.

[15] Skoskiewicz, T. *Phys. Status Solidi B* **1973**, *59*, 329–334.

[16] Schlapbach, L. *J. Phys. F: Metal Phys.* **1980**, *10*, 2477–2490.

[17] Knox, K.; Ginsberg, A. P. *Inorg. Chem.* **1964**, *3*, 555–558.

[18] Abrahams, S. C.; Ginsberg, A. P.; Knox, K. *Inorg. Chem.* **1964**, *3*, 558–567.

[19] Korst, W. L.; Warf, J. C. *Acta Crystallogr.* **1956**, *9*, 452–454.

[20] Mikheev, N. B. *Inorg. Chim. Acta* **1984**, *94*, 241–248.

[21] Zintl, E.; Harder, A. *Z. Elektrochem.* **1935**, *41*, 33–53.

[22] Lebech, B.; Hessel-Andersen, N.; Steenstrup, S.; Pedersen, A. S. *Acta Crystallogr., Sect. C: Cryst. Struct. Commun.* **1983**, *39*, 1475–1480.

[23] Fischer, P.; Schefer, J.; Tichy, K.; Bischof, R.; Kaldis, E. *J Less-Common Met* **1983**, *94*, 151–155.

[24] Warf, J. C.; Hardcastle, K. I. *Inorg. Chem.* **1966**, *5*, 1736–1740.

[25] Drulis, H.; Drulis, M.; Z.Borkowska, *J. Less-Common Met.* **1987**, *128*, 173–176.

[26] Auffermann, G. *Z. Anorg. Allg. Chem.* **2002**, *628*, 1615–1618.

[27] Shannon, R. D. *Acta Crystallogr., Sect. A: Found. Crystallogr.* **1976**, *32*, 751–767.

[28] Koester, L.; Rauch, H.; Seymann, E. *At. Data Nucl. Data Tables* **1991**, *49*, 65–120.

[29] Sears, V. F. *Neutron News* **1992**, *3*, 26–37.

[30] Alonso, J. A.; Retuerto, M.; Sánchez-Benítez, J.; Fernández-Díaz, M. T. *Z. Kristallogr.* **2010**, *225*, 225–229.

[31] Bergsma, J.; Loopstra, B. O. *Acta Cryst.* **1962**, *15*, 92–93.

[32] Andresen, A. F.; Maeland, A. J.; Slotfeldt-Ellingsen, S. *J. Solid State Chem.* **1977**, *20*, 93–101.

[33] Bronger, W.; Chi-Chien, S.; Müller, P. *Z. Anorg. Allg. Chem.* **1987**, *545*, 69–74.

[34] Atif, N. *Diplomarbeit*, Universität des Saarlandes, 2010.

[35] Kunkel, N.; Kohlmann, H.; Sayede, A.; Springborg, M. *Inorg. Chem.* **2011**, *50*, 5873–5875.

[36] Messer, C. E.; Eastman, J. C.; Mers, R. G.; Maeland, A. J. *Inorg. Chem.* **1964**, *3*, 776–778.

[37] Maeland, A. J.; Andersen, A. F. *J. Chem. Phys.* **1968**, *48*, 4660–4661.

[38] Maeland, A. J.; Lahar, W. D. *Z. Phys. Chem. (Muenchen, Ger.)* **1993**, *179*, 181–185.

[39] Blaschkowski, B.; Kaller, M.; Schleid, T. *Z. Anorg. Allg. Chem.* **2006**, 2149.

[40] Ashby, E. C.; Kovar, R.; Arnott, R. *J. Am. Chem. Soc.* **1970**, *92*, 2182–2183.

[41] Park, H.-H.; Pezat, M.; Darriet, B.; Hagenmuller, P. *Rev. Chim. min.* **1987**, *24*, 525–530.

[42] Schumacher, R.; Weiss, A. *J. Less-Common Met.* **1990**, *163*, 179–183.

[43] Remy, H.; Hansen, F. *Z. Anorg. Allg. Chem.* **1956**, *283*, 277–286.

[44] Rönnebro, E.; Noréus, D.; Kadir, K.; Reiser, A.; Bogdanovic, B. *J. Alloys Compd.* **2000**, *299*, 101–106.

[45] Meijerink, A. *J. Lumin.* **1993**, *55*, 125–138.

[46] Ellens, A.; Meijerink, A.; Blasse, G. *J. Lumin.* **1994**, *59*, 293–301.

[47] Gingl, F.; Yvon, K.; Fischer, P. *J. Alloys Compd.* **1992**, *187*, 105–111.

[48] Kohlmann, H.; Gingl, F.; Hansen, T.; Yvon, K. *Angew. Chem., Int. Ed.* **1999**, *38*, 2029–2033.

[49] Gingl, F.; Yvon, K.; Vogt, T. *J. Alloys Compd.* **1997**, *256*, 155–158.

[50] Gingl, F.; Hewat, A.; Yvon, K. *J. Alloys Compd.* **1997**, *253-254*, 17–20.

[51] Kadir, K.; Noréus, D. *Z. Phys. Chem. (Muenchen, Ger.)* **1993**, *179*, 243–247.

[52] Gingl, F.; Bonhomme, F.; Yvon, K. *J. Alloys Compd.* **1992**, *185*, 273–278.

[53] Gibb, Jr., T. R. P.; Schumacher, D. P. *J. Phys. Chem.* **1960**, *64*, 1407–1409.

[54] Morris, D. F. C.; Reed, G. L. *J. Inorg. Nucl. Chem.* **1965**, *27*, 1715–1717.

[55] Brice, J.-F.; Courtois, A.; Aubry, J. *J. Solid State Chem.* **1978**, *24*, 381–387.

[56] Brice, J.-F.; Perrin, M.; Leveque, R. *J. Solid State Chem.* **1979**, *30*, 183–188.

[57] Soulié, J.-P.; Laval, J.-P.; Bouamrane, A. *Solid State Sci.* **2003**, *5*, 273–276.

[58] Park, H. H.; Pezat, M.; Fournes, L.; Darriert, B.; Hagenmuller, P. *New J. Chem.* **1990**, *14*, 25–28.

[59] Freiser, M. J.; Methfessel, S.; Holtzberg, F. *J. Appl. Phys.* **1968**, *39*, 900–902.

[60] Tanguy, B.; Pezat, M.; Fontenit, C.; Portier, J. *C. R. Acad. Sci. C* **1975**, *280*, 1019–1020.

[61] Graf, T.; Felser, C.; Parkin, S. S. P. *Prog. Solid State Chem.* **2011**, *39*, 1–50.

[62] Nowotny, H.; Holub, F. *Monatsh. Chem.* **1960**, *91*, 877–887.

[63] Dahl, C.; Schuster, H.-U. *Z. Anorg. Allg. Chem.* **1993**, *619*, 1629–1632.

[64] Reichert, C. Ph.D. thesis, Universität des Saarlandes, 2014.

[65] Schäfer, H.; Eisemann, B.; Müller, W. *Angew. Chem.* **1973**, *85*, 742–760.

[66] Häussermann, U. *Z. Kristallogr.* **2008**, *223*, 628–635.

[67] Björling, T.; Noreus, D.; Häussermann, U. *J. Am. Chem. Soc.* **2006**, *128*, 817–824.

[68] Lorenz, B.; Lenzi, J.; Cmaidalka, J.; Meng, R. L.; Sun, Y. Y.; Xue, Y. Y.; Chu, C. W. *Physica C (Amsterdam, Neth.)* **2002**, *383*, 191–196.

[69] Shoemaker, C. B.; Shoemaker, D. P. *Acta Crystallogr.* **1965**, *18*, 900–905.

[70] Jeitschko, W. *Acta Crystallogr., Sect. B: Struct. Sci.* **1968**, *24*, 930–934.

[71] Sass, R. L.; Bracket, E. B.; Bracket, T. E. *J. Phys. Chem.* **1963**, *67*, 2863–2864.

[72] Gibb, Jr., T. R. P. *Prog. Inorg. Chem.* **1962**, *3*, 315–509.

[73] Müller, U. *Anorganische Strukturchemie*; Teubner, 2006.

[74] Bock, O.; Müller, U. *Acta Crystallogr., Sect. B: Struct. Sci.* **2002**, *58*, 594–606.

[75] Goldschmidt, V. M. *Naturwissenschaften* **1926**, *21*, 477–485.

[76] Pauling, L. *J. Am. Chem. Soc.* **1927**, *49*, 765–790.

[77] Fumi, F. G.; Tosi, M. P. *J. Phys. Chem. Solids* **1964**, *25*, 31–43.

[78] Shannon, R. D.; Prewitt, C. T. *Acta Crystallogr., Sect. B: Struct. Sci.* **1969**, *25*, 925–946.

[79] Wu, H.; Zhou, W.; Udovic, T. J.; Rush, J. J.; Yildirim, T. *J. Phys. Chem. C* **2009**, *113*, 15091–15098.

[80] Skoog, D. A.; Leary, J. J. *Instrumentelle Analytik*; Springer, 1996.

[81] Fox, M. *Optical Properties of Solids*, 2nd ed.; Oxford University Press, 2010.

[82] Gaft, M.; Reisfeld, R.; Panczer, G. *Luminescence Spectroscopy of Minerals and Materials*; Springer, 2005.

[83] Blasse, G. *Int. Rev. Phys. Chem.* **1992**, *11*, 71–100.

[84] Henderson, B.; Imbusch, G. F. *Optical spectroscopy of Inorganic Solids*; Oxford University Press, 2010.

[85] Tanner, P. A.; Mak, C. S. K.; Edelstein, N. M.; Murdoch, K. M.; Liu, G.; Huang, J.; Seijo, L.; Barandiarán, Z. *J. Am. Chem. Soc.* **2003**, *125*, 13225–13233.

[86] Liu, G.; Jacquier, B. *Spectroscopic Properties of Rare Earths in Optical Materials*; Springer, 2005.

[87] Bethe, H. *Ann. Phys. (Leipzig)* **1929**, *3*, 133–208.

[88] Dieke, G. H. *Spectra and Energy Levels of Rare Earth Ions in Crystals*; Interscience Publishers New York, 1968.

[89] Judd, B. R. *Operator Techniques in Atomic Spectroscopy*; McGraw-Hill, New York, 1963.

[90] Cowan, R. D. *The Theory of Atomic Structure and Spectra*; University of California Press, Berkeley, 1981.

[91] Wybourne, B. G. *Spectroscopy Properties of Rare Earth*; Wiley & Sons, New York, 1965.

[92] Van Pieterson, L.; Reid, M. F.; Wegh, R. T.; Soverna, S.; Meijerink, A. *Phys. Rev. B: Condens. Matter Mater. Phys.* **2002**, *65*, 045113 (16 pages).

[93] Van Pieterson, L.; Reid, M. F.; Burdick, G. W.; Meijerink, A. *Phys. Rev. B: Condens. Matter Mater. Phys.* **2002**, *65*, 045114 (13 pages).

[94] Roppe, R. C. *Luminescence and the Solid State*; Elsevier, 2004.

[95] Dorenbos, P. *J. Phys.: Condens. Matter* **2003**, *15*, 2645–2665.

[96] Wickleder, C.; Zhang, S.; Haeuseler, H. *Z. Kristallogr.* **2005**, *220*, 277–280.

[97] Wickleder, C. *Z. Anorg. Allg. Chem.* **2001**, *627*, 1693–1698.

[98] Zuckerman, J. J. *J. Chem. Educ.* **1965**, *42*, 315–317.

[99] Krishnamurthy, R.; Schaap, W. B. *J. Chem. Educ.* **1969**, *46*, 799–810.

[100] Schipper, W. J.; Vroon, Z. A. E. P.; Blasse, G.; Schleid, T.; Meyer, G. *Mater. Chem. Phys.* **1991**, *30*, 43–46.

[101] Blasse, G. *Phys. Status Solidi B* **1973**, *55*, K131–K134.

[102] Moine, B.; Pedrini, C.; Courtois, B. *J. Lumin.* **1991**, *50*, 31–38.

[103] Dorenbos, P. *J. Phys.: Condens. Matter* **2005**, *17*, 8103–8111.

[104] Muñoz H, G.; de la Cruz L., C.; Muñoz F., A.; Rubio O., J. *J. Mater. Sci. Lett.* **1988**, *7*, 1310–1312.

[105] Blasse, G.; Sabbatini, N. *Mater. Chem. Phys.* **1987**, *16*, 237–252.

[106] Ando, M.; Ono, Y. A. *J. Cryst. Growth* **1992**, *117*, 969–974.

[107] Najafov, H.; Kato, A.; Toyota, H.; Iwai, K.; Bayramov, A.; Lida, S. *Jpn. J. Appl. Phys.* **2002**, *41*, 2058–2065.

[108] Bleijenberg, K. C.; Blasse, G. *J. Solid State Chem.* **1979**, *28*, 303–307.

[109] Dorenbos, P. *J. Electrochem. Soc.* **2005**, *152*, H107–H110.

[110] Dorenbos, P. *J. Lumin.* **2005**, *111*, 89–104.

[111] Blasse, G.; Bril, A. *J. Chem. Phys.* **1967**, *47*, 5139–5145.

[112] Blasse, G.; Schipper, W.; Hamelink, J. J. *Inorg. Chim. Acta* **1991**, *189*, 77–80.

[113] Blasse, G.; Dirksen, G. J.; Meijerink, A. *Chem. Phys. Lett.* **1990**, *167*, 41–44.

[114] Lizzo, S.; Meijerink, A.; Blasse, G. *J. Lumin.* **1994**, *59*, 185–194.

[115] Piper, T. S.; Brown, J. P.; McClure, D. S. *J. Chem. Phys.* **1967**, *46*, 1353–1360.

[116] Bland, S. W.; Smith, M. J. A. *J. Phys. C: Solid State Phys.* **1985**, *18*, 1525–1538.

[117] Dorenbos, P. *J. Phys.: Condens. Matter* **2003**, *15*, 575–594.

[118] Wickleder, C. *J. Alloys Compd.* **2000**, *300-301*, 193–198.

[119] Rubio O., J. *J. Phys. Chem. Solids* **1991**, *52*, 101–174.

[120] Stevels, A. L. N. *J. Lumin.* **1979**, *20*, 99–109.

[121] Lakowicz, J. R. *Prinicples of Fluorescence Spectroscopy*; Springer, 2006.

[122] Kohlmann, H.; Kurtzemann, N.; Weihrich, R.; Hansen, T. *Z. Anorg. Allg. Chem.* **2009**, *635*, 2399–2405.

[123] Kohlmann, H.; Kurtzemann, N.; Hansen, T. C. *Powder Diffr.* **2013**, *28*, S242–S255.

[124] Widenmeyer, M.; Niewa, R.; Hansen, T. C.; Kohlmann, H. *Z. Anorg. Allg. Chem.* **2013**, *639, (2)*, 285–295.

[125] Kurtzemann, N.; Kohlmann, H. *Unpublished results*, year.

[126] Dutta, B. N.; Dayal, B. *Phys. Status Solidi B* **1963**, *3*, 2253–2259.

[127] Yim, W. M.; Paff, R. J. *J. Appl. Phys.* **1974**, *45*, 1456–1457.

[128] Yoder-Short, D. *J. Appl. Crystallogr.* **1993**, *26*, 272–276.

[129] Rodríguez-Carvajal, J. *Physica B (Amsterdam, Neth.)* **1993**, *192*, 55–69.

[130] Rietveld, H. M. *J. Appl. Crystallogr.* **1969**, *2*, 65–71.

[131] *TOPAS V2.1, General profile and structure analysis software for powder diffraction data, User Manual*; Bruker AXS: Karlsruhe, 2003.

[132] *TOPAS4.2, General profile and structure analysis software for powder diffraction data, User Manual*; 2009.

[133] Coelho, A. A. *J. Appl. Crystallogr.* **2003**, *36*, 86–95.

[134] *LAMP, the Large Array Manipulation Program.*

[135] Richard, D.; Ferrand, M.; Kearley, G. J. *J. Neutron Research* **1996**, *4*, 33–39.

[136] Hahn, R. *Bachelorarbeit*, Universität des Saarlandes, 2012.

[137] Kunkel, N.; Meijerink, A.; Kohlmann, H. *Phys. Chem. Chem. Phys.* **(2014)**, *DOI: 10.1039/c3cp55102d.*, year.

[138] Duan, C.-K.; Tanner, P. A.; Meijerink, A.; Makhov, V. *J. Phys. Chem. A* **2011**, *115*, 9188–9191.

[139] Ning, L.; Mak, C. S. K.; Tanner, P. A. *Phys. Rev. B: Condens. Matter Mater. Phys.* **2005**, *72*, 0851271–0851277.

[140] Lizzo, S.; Velders, A. H.; Meijerink, A.; Dirksen, G. J.; Blasse, G. *J. Lumin.* **1996**, *65*, 303–311.

[141] Barandiarán, Z.; Edelstein, N. M.; Ordejón, B.; Ruipérez, F.; Seijo, L. *J. Solid State Chem.* **2005**, *178*, 464–469.

[142] Dammak, H.; Antoshchenkova, E.; Hayoun, M.; Finocchi, F. *J. Phys.: Condens. Matter* **2012**, *24*, 435402–43407.

[143] Ho, A. C.; Hanson, R. C.; Chizmeshya, A. *Phys. Rev. B: Condens. Matter Mater. Phys.* **1997**, *55*, 14818–14830.

[144] Poort, S. H. M.; Meijerink, A.; Blasse, G. *J. Phys. Chem. Solids* **1997**, *58*, 1451–1456.

[145] Reshak, A. H.; Shalaginov, M. Y.; Saeed, Y.; Kityk, I. V.; Auluck, S. *J. Phys. Chem. B* **2011**, *115*, 2836–2841.

[146] Dorenbos, P. *J. Lumin.* **2007**, *122-123*, 315–317.

[147] Dorenbos, P. *Journal of Luminescence* **2008**, *128*, 578–582.

[148] Bachmann, V.; Ronda, C.; Oeckler, O.; Schnick, W.; Meijerink, A. *Chem. Mater.* **2009**, *21*, 316–325.

[149] Bertheville, B.; Herrmannsdörfer, T.; Yvon, K. *J. Alloys Compd.* **2001**, *325*, L13–L16.

[150] Zintl, E.; Harder, A. *Z. Physik. Chem.* **1931**, *B14*, 265–284.

[151] Mitchell, R. H.; Cranswick, L. M. D.; Swainson, I. *Phys. Chem. Miner.* **2006**, *33*, 587–591.

[152] Schipper, W. J.; Vroon, Z. A. E. P.; Blasse, G.; Schleid, T.; Meyer, G. *Chem. Mater.* **1992**, *4*, 688–692.

[153] Gerke, B.; Pöttgen, R. *Private communication 2013*.

[154] Reckeweg, O.; Molstad, J. C.; Levy, S.; DiSalvio, F. J. *Z. Naturforsch., B: Chem. Sci.* **2007**, *62*, 23–27.

[155] Reckeweg, O. *Private communication 2013*.

[156] Thoma, R. E.; Brunton, G. D. *Inorg. Chem.* **1966**, *5*, 1937–1939.

[157] Zalkin, A.; Templeton, D. H. *J. Am. Chem. Soc.* **1953**, *75*, 2453–2458.

[158] Bonnet, J. E.; Daou, J. N. *J. Appl. Phys.* **1977**, *48*, 964–968.

[159] Dronskowski, R. *Computational Chemistry of Solid State Materials*; Wiley-VCH, 2005.

[160] Cottenier, S. *Density Functional Theory and the family of (L)APW-methods: a step-by-step introduction*; Instituut voor Kern -en Stralingsfysica, K. U. Leuven, Belgium, 2002; (to be found at http://www.wien2k.at/reg_user/textbooks).

[161] Springborg, M. *Methods of Electronic-Structure Calculations. From Molecules to Solids.*; John Wiley & Sons Ltd, 2000.

[162] Hohenberg, P.; Kohn, W. *Phys. Rev. B: Condens. Matter Mater. Phys.* **1964**, *136*, 864–870.

[163] Singh, D. J. *Planewaves, Pseudopotentials and the LAPW Method*; Kluwer Academic Publishers, 1994.

[164] Kohn, W.; Sham, L. J. *Phys. Rev. B: Condens. Matter Mater. Phys.* **1965**, *140*, 1133–1138.

[165] Perdew, J. P.; Burke, K.; Ernzerhof, M. *Phys. Rev. Lett.* **1996**, *77*, 3865–3868.

[166] Bloch, F. *Z. Phys.* **1928**, *52*, 555–600.

[167] Kresse, G.; Furthmüller, J. *Phys. Rev. B: Condens. Matter Mater. Phys.* **1996**, *54*, 11169–11186.

[168] Hafner, J. *J. Comput. Chem.* **2008**, *29*, 2044–2078.

[169] Hamann, D. R.; Schlüter, M.; Chiang, C. *Phys. Rev. Lett.* **1979**, *43*, 1494–1497.

[170] Hamann, D. R. *Phys. Rev. B: Condens. Matter Mater. Phys.* **1989**, *40*, 2980–2987.

[171] Vanderbilt, D. *Phys. Rev. B: Condens. Matter Mater. Phys.* **1985**, *32*, 8412–8415.

[172] Blöchl, P. E. *Phys. Rev. B: Condens. Matter Mater. Phys.* **1994**, *50*, 17953–17979.

[173] Blöchl, P. E.; Kästner, J.; Först, C. J. In *Handbook of Material Modeling, Electronic structure methods: Augmented Waves, Pseudopotentials and the Projector Augmeneted Wave Method*; Yip, S., Ed.; Springer, 2005.

[174] Bader, R. F. W. *Atoms in Molecules - A Quantum Theory*; Clarendon Press Oxford, 1994.

[175] Henkelmann, G.; Arnaldson, A.; Jónsson, H. *Comput. Mater. Sci.* **2006**, *36*, 254–360.

[176] Sanville, E.; Kenny, S. D.; Smith, R.; Henkelman, G. *J. Comput. Chem.* **2007**, *28*, 899–908.

[177] Tang, W.; Sanville, E.; Henkelman, G. *J. Phys.: Condens. Matter* **2009**, *21*, 084204(7pages).

[178] Monkhorst, H. J.; Pack, J. D. *Phys. Rev. B: Condens. Matter Mater. Phys.* **1976**, *13*, 5188–5192.

[179] Baldereschi, A. *Phys. Rev. B: Condens. Matter Mater. Phys.* **1973**, *7*, 5212–5215.

[180] Chadi, D. J.; Cohen, M. L. *Phys. Rev. B: Condens. Matter Mater. Phys.* **1973**, *8*, 5747–5754.

[181] Perdew, J. P.; Wang, Y. *Phys. Rev. B: Condens. Matter Mater. Phys.* **1992**, *45*, 13244–13249.

[182] Pulay, P. *Chem. Phys. Lett.* **1980**, *73*, 393–398.

[183] Blöchl, P. E.; Jepsen, O.; Andersen, O. K. *Phys. Rev. B: Condens. Matter Mater. Phys.* **1994**, *49*, 16232–16233.

[184] Press, W. H.; Flannery, B. F.; Teukolsky, S. A.; Vetterling, W. T. *Numercial Recipes*; Cambridge University Press, New York, 1986.

[185] Methfessel, M.; Paxton, A. T. *Phys. Rev. B: Condens. Matter Mater. Phys.* **1989**, *40*, 3616–3621.

[186] Kresse, G.; Marsman, M.; Furthmüller, J. *VASP the Guide*; Computational Physics, Faculty of Physics, Universität Wien, 2013.

[187] Bahn, S. R.; Jacobsen, K. W. *Comput. Sci. Eng.* **2002**, *4*, 56–66.

[188] Björling, T.; Noreus, D.; Jansson, K.; Andersson, M.; Leonova, E.; Eden, M.; Halenius, U.; Häussermann, U. *Angew. Chem. Int. Ed.* **2005**, *44*, 7269–7273.

[189] Lee, M. H.; Evans, M. J.; Daemon, L. L.; Sankey, O. F.; Häussermann, U. *Inorg. Chem.* **2008**, *47*, 1496–1501.

[190] Subedi, A.; Singh, D. J. *Phys. Rev. B: Condens. Matter Mater. Phys.* **2008**, *78*, 045106.